XENON-INDUCED AXIAL POWER OSCILLATIONS IN THE 400 MW PEBBLE BED MODULAR REACTOR

GERHARD STRYDOM

Dissertation submitted in partial fulfilment of the requirements for the degree *Magister Scientiae* in Reactor Science at the North-West University, Potchefstroom campus.

Supervisor: Prof. H. Moraal (NWU – South Africa)
Co-supervisor: Dr. A. Lauer (FZJ - Germany)
Co-supervisor: Mr. F. Reitsma (PBMR – South Africa)

December 2007

Abstract

This study evaluates the stability of the 400 MW Pebble Bed Modular Reactor (PBMR) core design with respect to axial xenon-induced power oscillations. Since the two-dimensional capabilities of the reactor dynamics code TINTE exclude the possibility of modelling azimuthal xenon transients, the study is limited to the axial xenon stability behaviour of the PBMR equilibrium core, with some minor notes on radial xenon stability. The primary aim of this work is to provide the first quantitative investigation into the degree of inherent axial damping in the PBMR annular core design, as well as the xenon oscillation stability under power load-follow operational conditions.

It is shown that the TINTE code in its current form can be used with sufficient accuracy to model the axial variations that occur in the power density, iodine and xenon concentration levels, as well as the time-dependent feedback that exists between these parameters during load-follow transients. The detailed TINTE spatial power density and xenon concentration data were used to quantify the amplitude, period and linear damping properties of xenon-induced axial power oscillations. The representative operational load-follow transients that are investigated show well-damped xenon behaviour, and all local and global power and fuel temperature results are well within the prescribed safety limits.

These calculations lead to the conclusion that the current PBMR design is inherently very stable against xenon-induced axial power oscillations, and that the design shows an adequate margin to the instability transition point in this respect. No active xenon oscillation control system is therefore recommended for the PBMR.

Samevatting

Die stabilititeit van die 400 MW Korrelbed-reaktor word in hierdie verhandeling volgens xenon-gedrewe kragossilasies ondersoek. Die tweedimensionele aard van die dinamiese reaktorkode, TINTE, beperk die fokusarea van die ondersoek tot aksiale xenon-stabiliteitsberekeninge, maar enkele aspekte van die radiale xenon stabiliteit word ook bespreek. Die hoofdoel van hierdie verhandeling is om 'n eerste kwantitatiewe ondersoek na die Korrelbed-reaktor se inherente aksiale xenon-ossilasie stabilitiet daar te stel, en om tweedens ook die stabilitietseienskappe tydens kragvlakwisselinge te bepaal.

Daar word verder aangetoon dat die TINTE-kode in staat is om die aksiale veranderinge in die krag, en xenon-konsentrasie, , asook die tydafhanklike koppeling tussen hierdie veranderlikes tydens kragvlakwisselinge met voldoende akuraatheid te modelleer. Die amplitude, periode en linieêre dempingseienskappe van die xenon-gedrewe kragossilasies is gekwantifiseer deur van die TINTE ruimtelik-afhanklike krag- en xenon-konsentrasiedata gebruik te maak. Die operasionele kragvlakwisselinge wat in hierdie ondersoek ingelsuit is, het sterk gedempte xenon ossilatoriese gedrag getoon, en alle plaaslike en globale brandstoftemperature en kragresultate het binne aanvaarbare grense gewissel.

Hierdie berekeninge het tot die gevolgtrekking gelei dat die huidige 400 MW Korrelbed-reaktor baie stabiel ten opsigte van xenon-gedrewe aksiale kragossilasies is, en dat die ontwerp ver genoeg van die onstabiele ossilasieoorgangspunt verwyder is. 'n Aktiewe xenon-ossilasie beheersisteem word as gevolg van bogenoemde bevindings nie vir die Korrelbed-reaktor voorgestel nie.

Acknowledgements

This work would not exist without the critical contributions from Dr. Achim Lauer, who spent many patient hours with me in Germany and South Africa discussing the scope and detail of the topic. He remains one of the world's foremost experts on xenon oscillations in HTR reactors, and I am grateful to have had the opportunity to study under his technical guidance.

A special word of thanks is also extended to my PBMR colleagues Frederik Reitsma and Ivor Clifford, who played an important role in the technical discussions and critique of the work, and for coding the much needed algorithms used in this study. The support and suggestions from Prof. Harm Moraal also enabled the work to be clearly focused and completed in a finite time.

Lastly, I would like to thank my wife Estelle for her unwavering encouragement during the preparation of this work, and the Creator without Whom none of this would have been possible.

Contents

Abstract ii
Samevatting iii
Acknowledgements iv
Contents v
List of Figures vii
List of Tables x
Nomenclature xi
Greek Characters xii
List of Abbreviations 1

CHAPTER 1 1
1. OVERVIEW 1
1.1 Hypothesis and objectives 2
1.2 Dissertation layout 3

CHAPTER 2 4
2. LITERATURE STUDY AND THEORY 4
2.1 The theory of spatial xenon dynamics 4
2.2 Factors influencing the stability of xenon-induced power oscillations 9
2.3 Definition of quantitative spatial oscillation parameters 13
2.4 Summary 19

CHAPTER 3 20
3. OVERVIEW OF THE 400 MW PBMR DESIGN AND THE TINTE CODE 20
3.1 Overview of the 400 MW PBMR design 20
3.2 Overview of the TINTE code 23
3.3 summary 26

CHAPTER 4 27
4. RESULTS AND DISCUSSION OF THE PBMR 400 MW INHERENT AXIAL XENON STABILITY 27
4.1 introduction 27
4.2 Cases 1 to 4: Inherent xenon-induced Oscillation Properties of the PBMR 400 MW Equilibrium Core 28
4.2.1 Global Results 28
4.2.2 Spatial Results 30
4.2.3 Radial power and xenon variations 39
4.2.4 Spatial Damping Results 40
4.2.5 Variation of the damping ratio close to the axial nodal point 50
4.3 summary 52

CHAPTER 5 54
5. PBMR AXIAL XENON STABILITY DURING A 100%-40%-100% POWER LOAD-FOLLOW TRANSIENT 54
5.1 Global parameter results 55
5.2 Spatial xenon and power density results 59
5.2.1 Xenon 60
5.2.2 Power Density 66

5.3 Qualitative power density damping stability data 72
5.4 summary 77

CHAPTER 6 78
6. AXIAL XENON OSCILLATION STABILITY RESULTS FOR OTHER POWER LOAD-FOLLOW TRANSIENTS 78
6.1 Cases 7 to 10: Sensitivity study on the duration of the low power phase 78
6.2 Cases 11-14: Sensitivity study on the final power level of a power load-follow 83
6.3 summary 88

CHAPTER 7 90
7. SENSITIVITY STUDY ON FOUR PARAMETERS INFLUENCING PBMR AXIAL XENON STABILITY 90
7.1 Introduction 90
7.2 Core axial height increased to 20 m, 30 m and 40 m 91
7.3 Total power variations from 200 MW - 800 MW 96
7.4 Cases 22 to 24: Flatter Axial power shapes for the 400 MW, 800 MW and 15 meter cores 100
7.5 summary 107

CHAPTER 8 108
8. PRACTICAL XENON STABILITY IMPLICATIONS AND RECOMMENDATIONS FOR THE PBMR DESIGN 108

CHAPTER 9 110
9. CONCLUSIONS AND RECOMMENDATIONS 110
9.1 Conclusions 110
9.1.1 Chapters 4 and 5: Cases 1 to 6 111
9.1.2 Chapter 6: Cases 7-14 112
9.1.3 Chapter 7: Cases 15 to 24 112
9.2 Recommendations for future work 113

BIBLIOGRAPHY 115

APPENDIX A: TINTE 100%-40%-100% LOAD-FOLLOW DYNAMIC CONTROL ROD WORTH 118

List of Figures

Figure 2-1: A Portion of the Decay Scheme for A=135 [10] 5
Figure 2-2: Simplified Decay Scheme for ^{135}Xe 6
Figure 2-3: Low-energy cross section behaviour of several important isotopes [11] 7
Figure 2-4: Oscillation damping for ξ values of 0.1 and 0.2 18
Figure 2-5: Oscillation damping for ξ values of 0.5 and 0.8 18
Figure 3-1: Schematic layout of the PBMR design 20
Figure 3-2: Cross-sectional view of the PBMR core [4] 21
Figure 3-3: Fuel element design for the PBMR 22
Figure 3-4: Passive heat removal path in the PBMR 23
Figure 3-5: The modular structure of TINTE: principle of time discretization [24] 25
Figure 3-6: The TINTE nuclear calculation [24] 25
Figure 4-1: Cases 1 to 4 control rod bank insertion depths for the first 24 hours 29
Figure 4-2: Cases 1 to 4 core-averaged xenon absorption variation with time 29
Figure 4-3: Case 1 (100% power) normalized (to steady-state values) axial power density variation at radius r = 105 cm, for various core heights z. 30
Figure 4-4: Case 1 (100% power) detail of the normalized axial power density variation at radius r = 105 cm, for various core heights z. 31
Figure 4-5: Case 1 (100% power) detail of the normalized axial thermal flux variation at radius r = 105 cm, for various core heights z. 32
Figure 4-6: Case 4 (20% power) detail of the normalized axial power density variation at radius r = 105 cm, for various core heights z. 32
Figure 4-7: Case 1 (100% power) detail of the normalized xenon concentration variation at radius r = 105 cm, for various core heights z. 34
Figure 4-8: Case 4 (100% power) detail of the normalized xenon concentration variation at radius r = 105 cm, for various core heights z. 34
Figure 4-9: Case 1 (100% power) detail of the normalized iodine concentration variation at radius r = 105 cm, for various core heights z. 35
Figure 4-10: Case 1 (100% power) variation in the axial thermal flux difference at radius r = 105 cm, for various time points. 36
Figure 4-11: Case 1 (100% power) variation in the axial power density difference at radius r = 105 cm, for various time points. 37
Figure 4-12: Case 4 (20% power) variation in the axial power density difference at radius r = 105 cm, for various time points. 37
Figure 4-13: Case 1 (100% power) variation in the axial xenon concentration difference at r = 105 cm for various time points. 38
Figure 4-14: Case 1 (100% power) variation in the axial iodine concentration difference at r = 105 cm for various time points. 38
Figure 4-15: Case 1 variation in the radial power density difference at z = 800 cm, for 12 h to 36 h 39
Figure 4-16: Case 1 variation in the radial xenon concentration difference at z = 200 cm. 40
Figure 4-17: Case 1 normalized axial power density variation with time at r = 105 cm, including the overlaid least-squares fits. 42
Figure 4-18: Case 4 normalized axial xenon concentration variation with time at r = 105 cm, including the overlaid least-squares fits. 42
Figure 4-19: Case 1 normalized axial iodine concentration variation with time at r = 105 cm, including the overlaid Least-squares fits. 43
Figure 4-20: Variation in the inherent power density damping ratio ξ with steady-state power level. 49
Figure 4-21: Case 1 variation in the damping ratio ξ with axial height z at radius r = 105 cm, for fast and thermal flux, power density, iodine and xenon. 51
Figure 4-22: Case 2 variation in the damping ratio ξ with axial height z at radius r = 105 cm, for fast and thermal flux, power density, iodine and xenon. 51

Figure 4-23: Case 4 variation in the damping ratio ξ with axial height z at radius r = 105 cm, for fast and thermal flux, power density, iodine and xenon. 52
Figure 5-1: Case 5 core-averaged xenon absorption and control rod location 56
Figure 5-2: Case 5 and case 6 comparison - core-averaged xenon absorption levels 57
Figure 5-3: Case 5 and case 6 comparison- external reactivity levels 57
Figure 5-4: Case 5 average and maximum fuel temperature 58
Figure 5-5: Case 5 average and maximum fuel temperature detail 59
Figure 5-6: Case 5 spatial xenon concentration levels vs. time at 9 axial locations and r = 180 cm 60
Figure 5-7: Case 5 normalised spatial xenon concentration levels vs. time at 9 axial locations, and r = 180 cm 61
Figure 5-8: Case 6 normalised spatial xenon concentration levels vs. time at 9 axial locations, and r = 180 cm 61
Figure 5-9: Case 5 axial xenon concentration profiles at r = 180 cm, for 32 time points from 10 h - 72 h.62
Figure 5-10: Case 5 normalised axial xenon concentration profiles at r = 180 cm, for 32 time points from 10 h - 72 h 63
Figure 5-11: Case 5 normalised axial xenon concentration profiles at r = 180 cm, for 22 time points from 30 h - 72 h 63
Figure 5-12: Case 6 normalised axial xenon concentration profiles at r = 180 cm, from 10 h -72 h 64
Figure 5-13: Case 6 normalised axial xenon concentration profiles at r = 180 cm, from 30 h - 72 h 65
Figure 5-14: Case 5 radial xenon concentration profiles at z = 800 cm, from 14 h - 48 h 65
Figure 5-15: Case 6 radial xenon concentration profiles at z = 800 cm, from 14 h -48 h 66
Figure 5-16: Case 5 spatial power density vs. time at 9 axial locations, and r = 180 cm 67
Figure 5-17: Case 6 spatial power density vs. time at 9 axial locations, and r = 180 cm 68
Figure 5-18: Case 5 normalised spatial power density vs. time at 9 axial locations, and r = 180 cm 68
Figure 5-19: Case 6 normalised spatial power density vs. time at 9 axial locations, and r = 180 cm 69
Figure 5-20: Case 5 normalised axial power density profiles at r = 180 cm, from 10 h - 72 h 70
Figure 5-21: Case 6 normalised axial power density profiles at r = 180 cm, from 10 h - 72 h 70
Figure 5-22: Case 5 normalised axial power density profiles at r = 180 cm, from 30 h - 72 h 71
Figure 5-23: Case 5 normalised axial power density profiles at r = 180 cm, from 54 h - 72 h 71
Figure 5-24: Case 6 normalised axial power density profiles at r = 180 cm, from 30 h - 72 h 72
Figure 5-25: Case 5 least square fits to the normalised xenon concentration variations with time, at 7 axial locations and r = 180 cm 73
Figure 5-26: Case 5 least square fits to the normalised xenon concentration variations with time, at 7 axial locations and r = 180 cm. Detail between 28 h and 72 h 74
Figure 5-27: Case 5 least square fits to normalised power density variations with time, at 7 axial locations and r = 180 cm. Detail between 10 h and 72 h 75
Figure 5-28: Case 6 least square fits to normalised power density variations with time, at 7 axial locations and r = 180 cm. Detail between 10 h and 72 h 75
Figure 6-1: Control rod movements for Cases 7a to 10a. 80
Figure 6-2: Core-averaged xenon absorption (%) for Cases 7a to 10a. 81
Figure 6-3: Case 11 (400 MW to 300 MW) Least-squares fits to normalised power density variations with time, at 7 axial locations and r = 180 cm 84
Figure 6-4: Case 12 (400 MW to 500 MW) Least-squares fits to normalised power density variations with time, at 7 axial locations and r = 180 cm 84
Figure 6-5: Case 13 (400 MW to 600 MW) least-squares fits to normalised power density variations with time, at 7 axial locations and r = 180 cm 85
Figure 6-6: Case 14 (400 MW to 700 MW) least-squares fits to normalised power density variations with time, at 7 axial locations and r = 180 cm 85
Figure 6-7: Variation in the inherent power density damping ratio ξ with the final load-follow power level. 87
Figure 6-8: Comparison of the variation in the inherent power density damping ratio ξ between cases 1 to 4 and 11 to 14, based on third-order polynomial fit data. 88
Figure 7-1: Case 15 (20 m core) normalised axial power density at 7 axial locations along r = 180 cm ...92
Figure 7-2: Case 16 (30 m core) normalised axial power density at 7 axial locations along r = 180 cm ...93

Figure 7-3: Case 17 (40 m core) normalised axial power density at 6 axial locations along r = 180 cm ...93
Figure 7-4: Variation of power damping ratio with core axial height (m): calculated data points and fitted polynomial trend line ...95
Figure 7-5: Variations in the PBMR fuel, moderator, reflector and total temperature coefficients of reactivity with isodeltic changes in temperatures ...97
Figure 7-6: Variation of the power damping ratio with the steady-state power level for cases 18 to 21: calculated data points and fitted polynomial trend line ...99
Figure 7-7: Case 1 and case 22 axial power density profiles at r = 105 cm ...102
Figure 7-8: Case 22 (400 MW "flat power" core) normalised axial power density at 7 axial locations along r = 180 cm ...103
Figure 7-9: Case 23 (800 MW 600°C ROT "flat power" core) normalised axial power density at 7 axial locations along r = 180 cm ...104
Figure 7-10: Case 24 (15 m high "flat power" core) normalised axial power density at 7 axial locations along r = 180 cm ...104
Figure 7-11: 20 m high "flat power" core: normalised axial power density at 7 axial locations along r = 180 cm ...105
Figure A-1: Case 5 (100%-40%-100% load-follow) detail of core-averaged xenon absorption and control rod locations vs. time ...118
Figure A-2: Case 5 (100%-40%-100% load-follow) total power and external reactivity vs. time ...119
Figure A-3: Total power and control rod depth vs. time – 100%-40%-100%, with 40% power phase for 1 hour ...121
Figure A-4: Total power and control rod depth vs. time – repeated 100%-40%-100% cycle ...122
Figure A-5: Total power and control rod depth vs. time – 100%-60%-40%-100% load-follow ...122
Figure A-6: Total power and control rod depth vs time – 100%-40%-100% load-follow with reduced power reduction rate ...123

List of Tables

Table 2-1: ^{135}Xe and ^{135}I decay constants and fission product yields [10]. 4
Table 4-1: Control rod depths for cases 1-4 28
Table 4-2: Spatial locations of the least-squares fits 40
Table 4-3: Case 1 fast flux least-squares fit and oscillation damping data 44
Table 4-4: Case 1 thermal flux least-squares fit and oscillation damping data 44
Table 4-5: Case 1 power density least-squares fit and oscillation damping data 45
Table 4-6: Case 1 xenon concentration least-squares fit and oscillation damping data 45
Table 4-7: Case 1 iodine concentration least-squares fit and oscillation damping data 46
Table 4-8: Comparison between the power density damping ratio ξ for cases 1-4 47
Table 4-9: Comparison between the damping ratio ξ for cases 1-4: iodine and xenon concentration values 48
Table 5-1: External reactivity differences between case 5 and 6 58
Table 5-2: Case-averaged power density stability data for case 5 and case 6 76
Table 6-1: Summary of control rod minimum and maximum locations and xenon maximum absorption levels for Cases 7a to 10a 80
Table 6-2: Summary of core-averaged xenon absorption levels for Cases 7a to 10a 81
Table 6-3: Power density damping ratio ξ for cases 7a to 10a (transients include control rod movements) 82
Table 6-4: Power density damping ratio ξ for cases 7b to 10b (transients exclude control rod movements) 82
Table 6-5: Power density damping ratio ξ for cases 11to 14 86
Table 6-6: Third-order polynomial fitted power density damping ratio vs. reactor power level for cases 11 to 14 and cases 1 to 4 87
Table 7-1: Control rod movements for cases 15 to 17 91
Table 7-2: Cases 1 and 15-17 power density oscillation damping data 94
Table 7-3: Power density damping ratio ξ for cases 18 to 21 98
Table 7-4: Comparison of the average power density-damping ratio ξ for cases 1, 3, 18 and 19 99
Table 7-5: Nominal and permutated "flatter axial profile" PBMR 400 MW core isotopic material compositions 101
Table 7-6: Comparison of the power density damping ratio ξ between case 1 and cases 21 to 23 105
Table 7-7: Comparison of the power density damping ratio ξ between case 15 and case 24 106

Nomenclature

Latin Characters

A	Amplitude coefficient in general sinusoidal-exponential expression
a_1	Spatial xenon number density buckling expansion coefficient
a_2	Spatial flux buckling expansion coefficient
b	Oscillation damping constant
b_{cr}	Critical oscillation damping constant
b_{st}	Oscillation stability index
CR	Control rod
D	Time *t* offset term in general sinusoidal-exponential expression
$f_n(v)$	Eigen functions in the *v* direction
f(t)	Fit regression function
L	Linear expansion of the core in a given direction
M^2	Migration area
$N_{Xe}(t_0)$	Number density of xenon at time $t = t_0$
P	Constant related to sinus part of oscillation
Q	Constant related to co-sinus part of oscillation
Q(n)	Positive quadratic function of the number of oscillation nodes
R	Coefficient in general expression for flux oscillation period *T*
R^2	Absolute oscillation fit error
S	Coefficient in general expression for flux oscillation period *T*
T	Oscillation period
T_D	Damped oscillation period
T_N	Natural oscillation period (of an un-damped oscillation)
t	Time
X_0^{nm}	Matrix elements of the volume integrated steady-state xenon number density

Greek Characters

α	Alpha particle
β	Beta particle
β_T	Total temperature coefficient of reactivity
$\bar{\phi}_0$	Average steady-state thermal flux
ϕ_0^{nn}	Matrix elements of the volume integrated steady-state neutron flux
y_x	Ratio of the fission yield of ^{135}Xe over the total fission yield of atomic weight 135
λ_x	Decay constant of ^{135}Xe
λ_i	Decay constant of ^{135}I
μ^2	eigenvalues
μ_n^2	*n*-th eigenvalue of the self-adjoined 1-group eigenvalue problem
ρ_x^∞	Reactivity worth of xenon corresponding to the saturated xenon concentration at maximum thermal flux levels
$\sigma_{(Xe-135)}$	Microscopic fission cross-section of ^{135}Xe
ξ	Damping ratio
ω_D	Natural frequency of oscillating system with damping
ω_n	Natural frequency of oscillating system without damping

List of Abbreviations

2D	Two-dimensional
3D	Three-dimensional
BOL	Beginning of Life
BWR	Boiling Water Reactor
CANDU	**CAN**ada **D**euterium **U**ranium
DR	Damping ratio
EOL	End of Life
FZJ	Forschungszentrum Jülich
HTR	High Temperature Reactor
LWR	Light Water Reactor
PBMR	Pebble Bed Modular Reactor
TINTE	**TI**me-dependent **N**eutronics and **TE**mperatures
VSOP	**V**ery **S**uperior **O**ld **P**rogrammes

CHAPTER 1

1. OVERVIEW

Xenon-induced power oscillation stability, or the degree to which the spatial fission power changes due to variations in the xenon concentration, has been a topic of interest in reactor control and safety studies for more than 40 years [1],[2]. The xenon oscillation stability of a reactor design influences the operational control regime (load-follow patterns, suppressive rod movements by individual rods, etc), and could also drive safety related issues such as the time-integrated temperature loads on the core structural materials, or power peaking in the fuel. The main question regarding xenon oscillation stability is whether, over time, the change in xenon concentration exhibits a damped (decreasing variation) or un-damped oscillatory behaviour, and if un-damped xenon oscillations do occur, to what extent a planned control rod movement operational regime can suppress the effects of these oscillations.

In this study the stability of the 400 MW_{th} Pebble Bed Modular Reactor (PBMR) core design [3] [4] is evaluated with the reactor dynamics code TINTE (**TI**me-dependent **NE**utronics and **TE**mperatures) [5] with respect to xenon-induced power oscillations. The study is limited to investigate only axial xenon behaviour of the PBMR core, since the two-dimensional capabilities of TINTE exclude the possibility of modelling azimuthal xenon transients, and the possibility of introducing radial xenon transients is limited by the physical radial dimensions of the annular core.

A full xenon stability analysis is a complex and wide-ranging task. For example, analysis of all possible modes and states of a certain core design, as well as the core's behaviour at various life stages, are required. Beginning of Life (BOL) and End of Life (EOL) cores usually show different xenon-induced power oscillation stability characteristics compared to an equilibrium core, caused mainly by the various fuel enrichment levels used in the BOL stage, and the change in isotopic content during the core life-cycle. The scope of this study is limited to the equilibrium core only, i.e. the core state when the PBMR initial core and running phases are completed and the core consists of a heterogeneous mixture of fresh and used fuel [6]. No attempt at a xenon modal stability analysis is made in this study, since the selected set of transients represent a large enough detail data set to allow general stability conclusions to be made.

Since the xenon stability of the current PBMR design has previously only been addressed with a limited scope, and for an older 268 MW PBMR design [7], the study aims to provide the first quantitative investigation into the degree of inherent damping in the 400 MW PBMR annular core design, as well as the xenon oscillation stability under power load-follow operational conditions. Although a limited sensitivity study is included in the load-follow section, a full parametric study of all parameters influencing xenon stability falls outside the scope of this study. For typical examples of modern xenon stability studies performed for BWR and LWR core designs, the published papers [2], [8] and [9] represent good overviews of current practices. However, selected topics and conclusions from these studies that are applicable to High Temperature Reactor (HTR) cores will be reported in the Theory chapter of this study.

The results of the study are used by Pebble Bed Modular Reactor (Pty) Ltd to determine the need for an active xenon oscillation control system, and also to assess the characteristics of the required flux and power measurement system that will need to be implemented for the detection of these phenomena. It may be argued that the spatial power oscillations in the PBMR do not lead to any safety concerns, since the power density variations are far below the current limits, and the fuel temperature variations are also acceptable. However, most nuclear regulators worldwide require that any power fluctuations in an operating nuclear reactor should be well monitored and understood at all times, i.e. even though the PBMR core exhibits damped oscillations with small amplitudes and negligible safely implications, this does not mean that it is not necessary to investigate and measure these slight oscillations. This project also forms an important part of the core design input into the PBMR development, with unique challenges that need to be addressed due to the tall annular core.

1.1 HYPOTHESIS AND OBJECTIVES

It is hypothesized that:

1. The TINTE code in its current form can be used with sufficient accuracy to model the axial variations that occur in the power density, iodine and xenon concentration levels, as well as the time-dependent feedback that exists between these parameters during load-follow and other operational transient events.
2. The detail TINTE spatial power density and xenon concentration data can be used to quantify the amplitude, period and linear damping properties of xenon-induced spatial power oscillations.
3. The current PBMR core design exhibits damped axial power oscillations for a wide range of load-follow and control rod movement transients.
4. A sufficient margin to the un-damped oscillation transition point exists in the current PBMR core design.
5. The PBMR operational control design does not need to incorporate an active xenon oscillation suppression strategy, since the inherent properties of the core are sufficient to ensure damped oscillatory behaviour under all load-follow transient conditions.

The scope and objectives of this study are:

1. To confirm the existence of xenon-induced axial power oscillations during power variations in the current PBMR design, by using the dynamic reactor code TINTE.
2. To quantify the defining characteristics (e.g. amplitudes, periods and damping properties) of these spatial oscillations, by making use of a least-squares fitting routine developed for this purpose.

3. To determine if the PBMR core design exhibits damped oscillations for a representative set of operational load-follow transients, and to identify and investigate the parameters responsible for the inherent oscillation stability. The inherent xenon damping properties of the PBMR design are obtained by specifying a strong local disturbance in the thermal flux levels, while the "practical" focus of this study is on operational load-follow events in the PBMR, since these events are the leading cause of xenon-induced power oscillations.
4. To determine the need for active operational xenon oscillation control strategies. The focus of this study is not the detail characterisation of an active flux mapping and control system, and therefore only the basic properties of such a system will be discussed.

1.2 DISSERTATION LAYOUT

An introduction to the topic of xenon oscillations and stability theory in general nuclear reactor designs is given in Chapter 2, including an overview of factors that contributed towards oscillation stability in other HTR core designs. A short summary description of the PBMR core design as used in this study is presented in Chapter 3. The main features of the TINTE code are also described in this chapter, as well as the least-squares fitting method used to quantify the damping characteristics of the spatial oscillations.

Chapter 4 presents the results of investigations into the stability of the current PBMR design regarding axial power variations induced by xenon oscillations. Results from two main classes of xenon oscillations are presented: inherent stability (by exciting spatial oscillations via artificial control rod movements) in Chapter 4, and the oscillation stability under operating conditions (power load-follows) in Chapter 5.

The xenon-induced power density stability of several load-follow variations are presented in Chapter 6, where two sensitivity studies have been performed on the duration and amplitude of selected phases within these power load-follows. Chapter 7 shows the results of variations in the magnitudes of four important contributors to the PBMR xenon stability: the core height, the total operating power, the effect of temperature feedback on the progression of the oscillations, and the role of the relative flatness of the axial power profile.

The study closes with a section on the practical implications of the xenon oscillation stability results in Chapter 8, where suggestions for the detection of these spatial variations are made. The conclusion and summarised results of the study are presented in Chapter 9, including identification of possible future work. Additional data on the 100%-40%-100% load-follow transient is contained in Appendix A.

CHAPTER 2

2. LITERATURE STUDY AND THEORY

2.1 THE THEORY OF SPATIAL XENON DYNAMICS

Xenon is a fission product that is formed directly by fission, as well as by β decay of the $^{135}Te \rightarrow {}^{135}I \rightarrow {}^{135}Xe$ chain. The decay constants and fission yields of ^{135}I and ^{135}Xe are presented in Table 2-1, while a portion of the A=135 production and decay scheme is shown in Figure 2-1. It can be seen in Figure 2-1 that ^{135}Xe is formed directly by fission, and by decay of the ^{135}I isotope. It is removed by direct neutron capture, as well as decay to the ^{135}Cs isotope.

Table 2-1: ^{135}Xe and ^{135}I decay constants and fission product yields [10].

Nuclide	Decay constant (/hr)	Direct Fission yield from ^{233}U (%)	Direct Fission yield from ^{235}U (%)	Direct Fission yield from ^{239}Pu (%)	Direct Fission yield from ^{241}Pu (%)
^{135}I	0.104	4.88	6.39	6.10	7.69
^{135}Xe	0.075	1.36	0.23	1.09	0.26

A few approximations are usually made to the decay scheme shown in Figure 2-1:

i. The total yield from ^{235}U fission for the mass 135 chain is 6.61%, made up of the 6.39% formation of ^{135}Te, and the 0.23% ^{135}Xe yield. Since the half-life of ^{135}Te is short (29 seconds), compared to the longer half-lives of ^{135}I (6.7 h) and ^{135}Xe (9.2 h), it is assumed that the chain originates with the ^{135}I isotope with a yield of 6.39%, as shown in Table 2-1.

ii. The absorption cross-section of ^{135}I is small enough to be ignored in typical reactor thermal neutron fluxes (it only plays a role for flux levels higher than $1x10^{16}$ neutrons/cm^2.s [10]). In the case of the PBMR operating at 400 MW, the average TINTE thermal flux is $7.7x10^{13}$ neutrons/cm^2.s at 400 MW. The direct removal of ^{135}I by the thermal neutron flux is therefore usually ignored in most thermal reactors.

iii. Approximately 9% of the ^{135}I decay produces the meta-stable isotope ^{135m}Xe, which decays to the ground state isotope ^{135}Xe with a half-life of 15.3 minutes. This short-lived meta-stable isotope is also ignored, and it is assumed that all decay reactions of ^{135}I produce the ground state isotope ^{135}Xe directly.

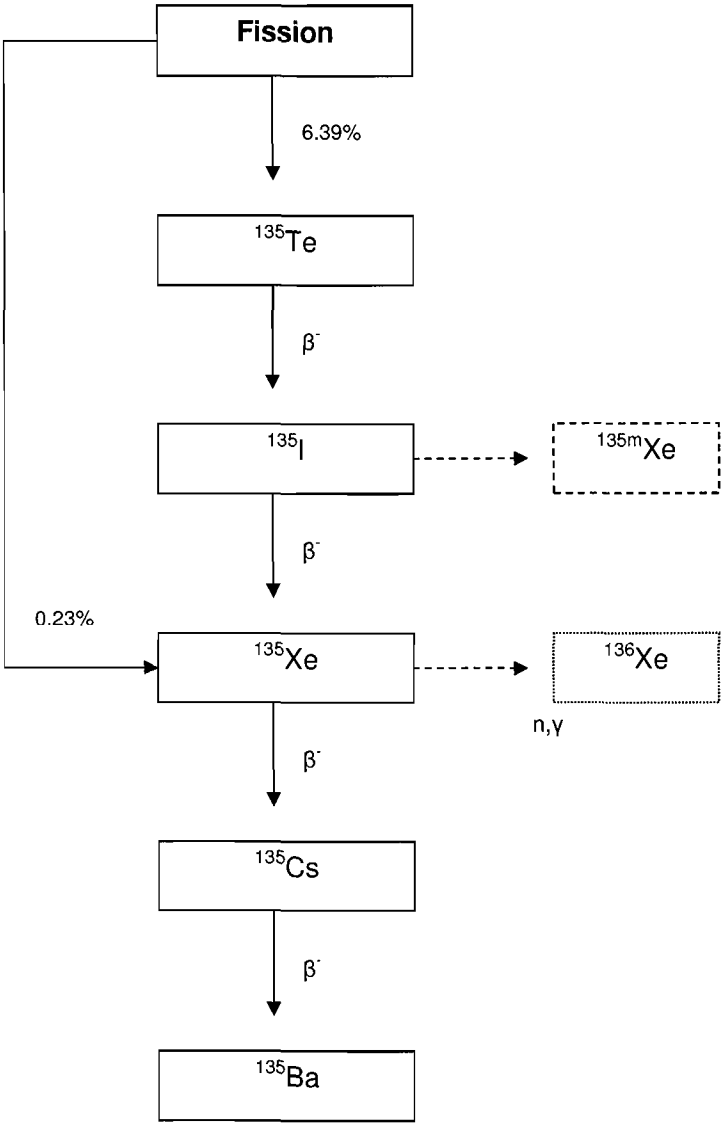

Figure 2-1: A Portion of the Decay Scheme for A=135 [10]

With these assumptions made, a simplified decay scheme can be used (Figure 2-2). The direct fission production of ^{135}Xe, and its direct removal to ^{136}Xe by thermal neutron capture is shown, as well as the two important delayed ^{135}Xe production and removal processes $^{135}I \rightarrow {}^{135}Xe$, and $^{135}Xe \rightarrow {}^{135}Cs$.

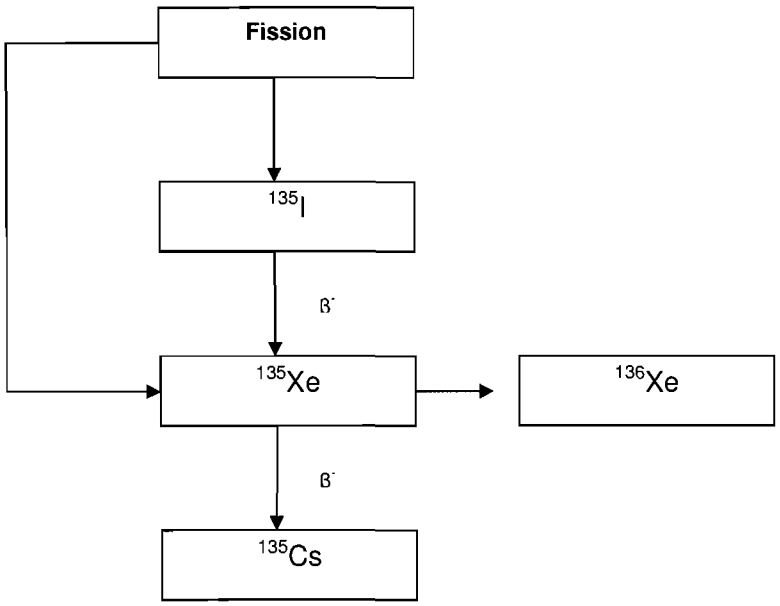

Figure 2-2: Simplified Decay Scheme for ^{135}Xe

^{135}Xe is considered to be the most important neutron poison in all types of thermal reactors, since it has an extremely large *thermal* neutron absorption cross-section of ~ $2x10^6$ barns, compared to ~ 500 barns for ^{235}U thermal fission. The ^{135}Xe absorption cross-section is indicated in Figure 2-3, where the absorption cross-sections for uranium and plutonium fuel isotopes are also shown.

For the typical equilibrium PBMR 100% power level, the global neutron absorption rate of xenon is between 2.2% and 2.6% of all absorbed thermal neutrons, but the real effect of xenon on the spatial reactor power is in the dynamic interaction between the xenon production and removal reactions. The difference in time-scales between these processes results in complex spatial xenon behaviour over time: whenever power (or thermal neutron flux) changes, the xenon and iodine production rates immediately change in opposite directions, while the 6.7 hour half-life of ^{135}I implies that a second variation in the xenon concentration will occur in the following few hours. These fast and slow production and removal mechanisms are the drivers for the so-called "xenon oscillations", since a cyclic increase and decrease in xenon levels would result in a mirror-image cyclic decrease and increase in fission power levels. As an example, consider the following chain of events:

Suppose that, as a result of a local perturbation in the thermal flux (e.g. the axial movement of a control rod in the top of the core), the flux in one part of the reactor (Region 1) is increased, while in another part some distance away (Region 2), the flux is correspondingly decreased due to the constant total power output of the reactor.

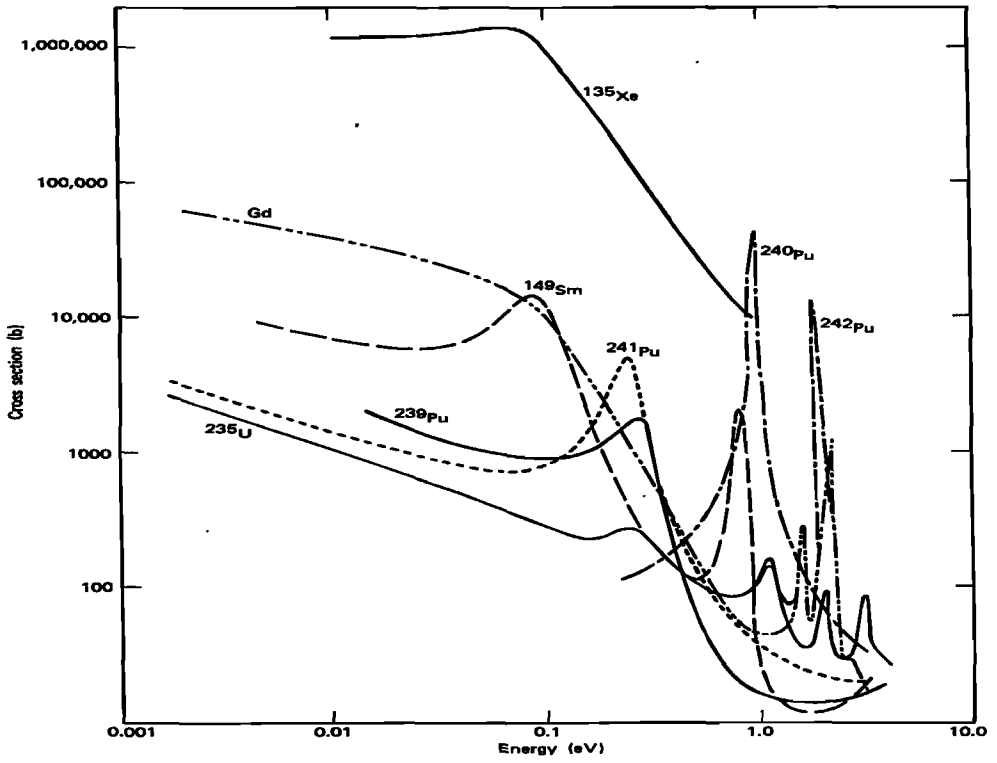

Figure 2-3: Low-energy cross section behaviour of several important isotopes [11]

This is only possible in a large reactor with linear dimensions several times greater than the thermal neutron diffusion length, so that neutrons do not diffuse directly from one region to another whenever a perturbation occurs. As one of the possible indicators, the mean neutron diffusion length can be used to determine how far the neutrons will diffuse from a source (e.g. a fission event) before they are absorbed, on average. The diffusion length is typically 2.8 cm for H_2O-moderated reactors and 59 cm for graphite-moderated reactors [12], which implies that graphite-moderated cores will typically need to be spatially much larger than water-moderated cores for any spatial xenon oscillations to occur.

The following changes will then occur in each of the regions:

- *Region 1:*

  As a result of the increase in the thermal flux in region 1, the rate of ^{135}Xe removal increases promptly because of increased neutron capture. The rate of ^{135}I formation through fission increases at the same time, but since ^{135}I has a half-life of 6.7 h, there is a considerable delay between the increase in the flux in region 1 and the associated increase in the rate of ^{135}Xe formation (via ^{135}I decay). Consequently, the *net* prompt result is that the xenon concentration decreases. This has the immediate effect of decreasing the neutron capture in region 1, so that the flux levels increase even further.

The result is a continued decrease in the xenon concentration and a steady increase in the thermal flux, until the delayed production of xenon (formed by the decay of ^{135}I) brings about an increase in the ^{135}Xe concentration. The thermal neutron flux in region 1 will then start to decrease again.

- *Region 2:*

In the meantime, if the total reactor power is kept constant, the increase in flux in region 1 will be offset by a decrease in region 2. As a result of this flux decrease, the ^{135}Xe concentration will increase because of decreased neutron capture and the continuing decay of ^{135}I formed before the decrease in the neutron flux. Hence, the flux in region 2 will tend to decrease still further. The decrease continues until it is halted, and eventually reversed by the decay of ^{135}Xe and the lower rate of production from ^{135}I in the decreased flux.

It is evident therefore that the neutron flux in region 1 increases to a maximum and then decreases; while the flux in region 2 decreases to a minimum and then increases again. Consequently, there is a continuous series of oscillations in the thermal neutron flux and power between the two regions. These oscillations typically have periods of ~ 1 day, so in principle it is quite possible to measure and control spatial power oscillations effectively. Note that since the time-scale of xenon-power oscillations is in the order of several hours, both short-term effects (e.g. delayed neutrons) and long-term effects (e.g. fuel depletion) can be ignored when xenon stability is investigated.

Two main conditions must be satisfied for any spatial xenon oscillation to start:

- The reactor must be large enough. This means that the axial, radial or azimuthal dimensions must be several times greater than the thermal neutron diffusion length for xenon/power oscillations to occur in that dimension. In reactor physics terms, this allows certain regions in the reactor, located far enough apart, to be spatially de-coupled from each other, which would enhance xenon spatial oscillations. Tightly coupled regions cannot exhibit oscillatory behaviour, since the local changes in flux levels are immediately propagated in all spatial dimensions.
- Xenon oscillations can occur only if the neutron flux magnitude is large enough to make the rate of consumption of ^{135}Xe by neutron capture large in comparison with the rate of ^{135}Xe decay. This condition requires the thermal flux to be appreciably greater than 3×10^{11} neutrons/cm^2.s [13]. Since the current *core-averaged* thermal flux for the PBMR core at 400 MW is 7.7×10^{13} neutrons/cm^2.s, xenon oscillations can definitely occur at this power level. Investigations into a possible PBMR lower boundary power level below which no xenon oscillations can occur, confirmed that very small amplitude axial power oscillations still occur as low as 12 MW total power, driven mostly by the bottom half of the core which still produces thermal flux levels up to 9×10^{12} neutrons/cm^2.s in certain locations.

Apart from the spatial power variations due to local xenon redistribution, *global* changes in the power level also result in global responses in the xenon concentration. For example, if the total reactor power is decreased to 40%, the global xenon build-up after approximately 7 h causes the well-known "xenon override" effect, where the build-up in negative reactivity needs to be countered by the addition of positive reactivity. In some instances, a global (or "fundamental mode") xenon oscillation can occur, whereby the core-integrated xenon concentration levels rise and fall as an exponentially damped or un-damped harmonic function. This fundamental oscillation mode can occur in isolation, but it can also be accompanied (and overlaid) by several of the spatial higher-order modes, for example the first axial mode. This study does not include an example of a ground-mode oscillation, as the focus here is on the first mode oscillations that may occur in the axial dimension.

2.2 FACTORS INFLUENCING THE STABILITY OF XENON-INDUCED POWER OSCILLATIONS

The occurrence of xenon oscillations is dependent on a complex interaction between various design, operational and temporal parameters. Some of these parameters work against each other in terms of stability: An increase in core height tends to decrease the degree of xenon damping, but an increase in the negative temperature reactivity coefficient will increase xenon damping. Other combinations of parameters might induce unstable oscillations in a design that was previously thought to be stable. A definitive conclusion on xenon stability for a specific core design can therefore not be made by considering each of these parameters independently - it is the manner in which they interact in a specific reactor design and at a specific stage in that reactor's life that is important.

A previous study on HTR-specific xenon stability [14] reported the following conclusions:

1. Diverging axial xenon oscillations only occurred in HTR cores when the active core height was increased to more than 8 m, with a *simultaneous* power density increase to more than 20 MW/m^3. Although the PBMR core is taller than this criterion at 11 m, the PBMR average power density is only approximately 5 MW/m^3, so it is not possible to definitively conclude from the combination of these two factors whether the PBMR core should exhibit diverging axial oscillations. It should also be noted that the study reported in [14] specifically investigated HTR designs that had control rods inserted directly into the pebble beds, in contrast to the PBMR approach of locating the rods in the side reflector.
2. No diverging radial xenon oscillations were observed for cylindrical cores of up to 6.4 meters in radius. Since the PBMR annular core design uses a central reflector with a radius of 1 meter, this observation can also not be directly applied to the PBMR design. However, it can be stated that if a cylindrical core of such a large radius did not show diverging oscillatory behaviour, a thin annular core with an inner radius of 85 cm and an outer radius of 185 cm should be very stable against xenon-induced radial power oscillations, or exhibit no radial oscillatory behaviour at all.

The case for no radial oscillations is in fact far stronger when the mean thermal neutron diffusion length of 59 cm in graphite is compared with the annular core width of 85 cm. This essentially implies that the annular core is strongly neutronically coupled in the radial dimension and no radial oscillations should occur.

3. The most unstable mode in [14] proved to be the first azimuthal mode, which was observed for very flat cylindrical cores with radii of 3.74 m and height/diameter ratios of less than 0.9. Since the PBMR height/diameter ratio is approximately 3.5, azimuthal oscillations should be strongly damped in the current design. Although the 2D TINTE code cannot be used for aziumuthal studies, a related study [17] performed with the three-dimensional version of the VSOP99 code showed that only very weak azimuthal xenon and power oscillations occurred, and that all observed modes were strongly damped.

One of the most important stabilising mechanisms is the negative temperature reactivity coefficient. In fact, Stacey [1] reports that the sensitivity of all other parameters decreases drastically with an increase in the magnitude of the negative temperature reactivity coefficient. A large negative coefficient could suppress (or even overcome) xenon oscillations since the changes in the temperature would oppose the flux changes due to xenon. An increase in flux levels would increase the local fuel temperatures, which in turn would suppress the flux increase almost immediately due to the Doppler broadening of the ^{238}U resonance absorption cross-section. The Doppler feedback effect was also found to be more effective than the moderator temperature feedback in inhibiting xenon-induced power oscillations.

These general observations by Stacey [1] are supported by work performed over a number of years for various reactor types, which indicates that the xenon stability decreases with:

1. An increase in core size.
2. A reduction in the neutron diffusion length.
3. A decrease in the magnitude of the negative power coefficient of reactivity.
4. An increase in the thermal neutron flux levels (i.e. power).
5. An increase in the "flatness" of the thermal flux distribution (i.e. a reduction in the dimensional power peaking factors).
6. A decrease in the fuel enrichment.

It can be deduced from these observations that a tall core, operating at high power densities with low enriched fuel, and exhibiting a very flat axial power profile would be represent one of the most unstable core configurations possible with respect to axial xenon/power stability. Compared to this unstable configuration, the PBMR core is quite tall, but exhibits a low power density and a large negative temperature feedback coefficient, together with a peaked axial power profile. These factors should result in a stable PBMR core design from a qualitative point of view. In support of these general conclusions, Chapter 7 presents the results of a parametric study performed on the current PBMR design on some of the oscillation stability factors indicated above.

A general mathematical xenon stability description using linear perturbation theory, based on the rigorous approach followed by Lauer [16], showed that the three-dimensional individual oscillation neutron flux modes behaved in a harmonic exponentially increasing or decreasing manner. An expression was obtained for the flux oscillation period T, given by

$$T = 4\pi (4\,S - R^2)^{-0.5} \tag{2.1}$$

where the terms R and S are defined by

$$R = \lambda_x + \lambda_i + \sigma\phi_0^{nn} + \frac{a_1 \sigma \phi_0^{nn} (X_0^{nn} - y_x)}{\mu_n^2 - a_2 \phi_0^{nn}} \tag{2.2}$$

and

$$S = \lambda_i \left[\lambda_x + \sigma\phi_0^{nn} - \frac{a_1 \sigma \phi_0^{nn} (1 - X_0^{nn})}{\mu_n^2 - a_2 \phi_0^{nn}} \right] \tag{2.3}$$

In these expressions, the symbols have the following meaning:

λ_x = decay constant of ^{135}Xe, λ_i = decay constant of ^{135}I,

σ = microscopic absorption cross-section of ^{135}Xe ,

ϕ_0^{nn} = $\int_{reactor\,volume} f_n(v)\phi_0(v) f_n(v) dV$, the matrix elements of the volume-integrated steady-state neutron flux (where a one-group flux has been assumed, and $f_n(v)$ are the eigenfunctions of the n-th mode),

a_1 = buckling expansion coefficient, multiplied with a spatial xenon number density term in the buckling perturbation expression $B^2(v,t) = B_0^2(v) + a_1 X(v,t) + a_2 \phi(v,t)$

a_2 = buckling expansion coefficient, multiplied with a spatial flux term in the buckling perturbation expression $B^2(v,t) = B_0^2(v) + a_1 X(v,t) + a_2 \phi(v,t)$

X_0^{nn} = $\int_{reactor\,volume} f_n(v) X_0(v) f_n(v) dV$, the matrix elements of the volume-integrated steady-state xenon number density

y_x = $\frac{\gamma_X}{\gamma}$, the ratio of the direct fission yield of ^{135}Xe over the total fission yield of atomic weight 135,

μ_n^2 = the n-th eigenvalue of the self-adjoined one-group eigenvalue problem

An expression was also derived for the oscillation stability index b_{st} (with simplified treatments assumed for the temperature feedback and the spatial dependence of the buckling terms):

$$b_{st} = -\frac{1}{2}R = -\frac{1}{2}\left[\lambda_x + \lambda_i + \sigma\phi_0^{nn} + \frac{a_1\sigma\phi_0^{nn}(X_0^{nn} - y_x)}{\mu_n^2 - a_2\phi_0^{nn}}\right] \qquad (2.4)$$

(The stability index was used in the older American literature [1] as an indicator of xenon stability. It is defined as $b_{st} = -b$, i.e. simply the negative damping constant in the current context).

Eq. (2.2) to Eq (2.4) were then used to derive a simplified, but very useful, stability criterion:

$$\mu_n^2 M^2 - \beta_T\bar{\phi}_0 + \frac{\rho_X^\infty\,\sigma\bar{\phi}_0\left[\frac{1}{1+(\lambda_x/\sigma\bar{\phi})} - y_X\right]}{\lambda_x + \lambda_i + \sigma\bar{\phi}_0} > 0 \qquad (2.5)$$

In this expression, the symbols have the following meaning:

ρ_x^∞ = reactivity worth of xenon corresponding to the saturated xenon concentration at maximum thermal flux levels,

M^2 = neutron migration area,

β_T = total temperature coefficient of reactivity,

$\bar{\phi}_0$ = average steady-state thermal flux.

The terms in this stability criterion can be used in a qualitative manner to discuss the effects of various parameters on the damping stability. The first and second terms in Eq. (2.5) describe the *stabilising* effect of neutron diffusion and the negative temperature feedback on spatial flux instabilities, while the third term describes the complex delayed xenon dynamics. The following qualitative tendencies can be deduced from the stability criterion expression (2.5):

i. ***First term:*** $\mu_n^2 M^2$

a. Larger eigenvalues (μ^2) would result in this term becoming larger positive, and increasing the stability of oscillation modes. A stability study such as this can therefore ignore the higher modes as a first approximation, and focus on the first modes which would be the least stable of all the higher modes. From modal analysis it is known that the fundamental mode, the first and second azimuthal modes, the first radial mode, and lastly the first axial mode occur with increasing stability properties.

b. The term $\mu_n^2 M^2$ can be approximated by $\mu_n^2 M^2 \sim Q(n)\,(M/L)^2$, with *Q(n)* a positive quadratic function of the number of nodes, and *L* the linear expansion of the core in a given direction.

This implies that an increase in reactor dimensions (i.e. larger *L*, compared to the mean neutron mean free path length) would lead to smaller values of $\mu_n^2 M^2$, which means a nearly quadratic reduction of the damping stability with an increase in core size.

c. A more subtle analysis of *Q(n)* shows that the eigenvalues μ_n^2 become smaller as the steady-state flux profile becomes flatter, but not with a linear dependency. This implies that a reactor design with a flattened flux profile tends to be less stable against xenon-induced power oscillations.

ii. ***Second term:*** $\beta_T \bar{\phi}_0$

This term indicates that a larger negative total reactivity coefficient β would almost linearly increase the xenon damping stability.

iii. ***Third term:*** $\dfrac{\sigma \bar{\phi}_0 \cdot \left[\dfrac{1}{1 + (\lambda_x / \sigma \bar{\phi}_0)} - y_X \right]}{\lambda_x + \lambda_i + \sigma \bar{\phi}_0} > 0$

The destabilising effect of the complex third term, essentially representing the dynamic xenon feedback, is discussed in more detail in [16]. However, two implications of this term deserve special mention.

a. At low and moderate flux levels (i.e. $\sigma \bar{\phi} << \lambda_x + \lambda_i$), the third term is almost proportional to $\rho_x^\infty \sigma \bar{\phi}$. This implies that the degree of instability generally increase with an increase in the average thermal flux levels and the saturated xenon reactivity worth.

b. At very high flux levels (exceeding 1×10^{14} neutrons/cm^2·s) the third term approximates a constant value $\rho_X^\infty (1 - y_X)$. The proportionality of the numerator on the thermal flux levels indicates that an upper flux limit for the occurrence of xenon oscillations exists, if the total temperature reactivity feedback coefficient is negative.

2.3 DEFINITION OF QUANTITATIVE SPATIAL OSCILLATION PARAMETERS

Advances made since 1970 in the numerical simulation of reactor cores by using multi-dimensional neutronic codes greatly shifted the emphasis away from the determination of stability criteria for a certain core design. The accurate modelling of the fast and thermal flux spatial distribution, the spatial xenon and iodine concentrations, temperature and other reactivity feedback effects and the modelling of poisons and control rods, are all included in modern codes such as TINTE, so that approximate modal or linear analysis methods are not used as frequently as in the past. In fact, Stacey [17] shows in his discussion of linear xenon stability analysis, and specifically the λ-mode and μ-mode approximations to the *p*-mode equations, that the *p*-mode equations require numerical solution techniques for all but the simplest geometries, with similar calculation burdens compared to the neutron diffusion equations.

In modern xenon stability analysis, λ-mode linear stability modules are therefore incorporated into standard multi-dimensional, multi-group diffusion solvers, with reasonable success [8]. The scope of this study does not include the determination and use of these modal stability criteria, but rather follows a "brute-force" technique of calculating a representative set of transients very accurately, and using a mathematical fitting technique to quantify the integrated xenon damping properties of the PBMR design. The term "integrated" is used here, since TINTE calculates the total integrated spatial effect of the changes in reactor state parameters. For example, the fundamental, first azimuthal and higher order radial and axial oscillation modes can exist superimposed on each other, so that the simplified fitting approach used here is actually a coarse method, when viewed from a mathematical point of view. However, it is also clear from the transient results that follow that the large majority of cases did in fact *not* lead to the excitation of the fundamental or first radial modes, and that only the first axial mode was observed.

Before the derivation of a quantitative oscillating damping parameter is pursued, a few related concepts used in this study must first be defined:

i. External excitation of xenon oscillations: The disturbance of the spatial steady-state flux and/or xenon distribution by any temporary event (e.g. control rod repositioning, power level changes, gas temperature changes), lasting for a time period which is *short* compared to the intrinsic natural xenon oscillation period (typically ~ 24 h).

ii. Xenon-induced oscillation: The periodic variations of the spatial flux and xenon distributions by a long-lasting coupled inverse reaction against some initial disturbances. Only the intrinsic xenon dynamics are driving the oscillatory behaviour in this case. A detailed explanation of this complex term is given in [1].

iii. *Free* xenon oscillations: Except for the short initial excitation phase (e.g. control rod changes or mass flow and temperature variations) which possibly caused temporary perturbations in the flux and/or xenon spatial distributions, no other spatially influencing actions are made during the transient phase. Only the inherent xenon "driving" mechanism and temperature "dampening" feedback on the flux distribution remains in the free oscillation phase. Substantial control rod movements during the free oscillation phase are specifically not present, as this would influence the spatial flux distribution and degrade the intrinsic oscillation characteristics. Note that a global control of reactivity, e.g. by soluble poison in a water-moderated core, would still allow "free" xenon oscillations, since all spatial locations are influenced simultaneously to the same degree.

As an example of the application of these terms, consider a 100%-40%-100% power load-follow transient. The mass flow and temperature changes during these power ramps, which happen over a period of a few minutes, would *excite* global and/or spatial variations in the xenon concentrations, which in turn would influence the thermal flux levels.

The control rods would then be moved to compensate for the global variation in the core reactivity, since the current PBMR design precludes the correction of short term reactivity imbalances by global reactivity methods (e.g. neutron poison gasses). However, the movements of the rods to balance the global core reactivity interacts spatially with the dynamic flux shifting of the xenon redistributions, and introduces non-linear excitation and damping effects into xenon and thermal flux oscillation behaviour. Since the rods typically stop moving after 40 h, the phase between 40-72 h could be treated as a free xenon oscillation phase.

In order to determine the inherent damping stability of the core design, the same load-follow transient must also then be analysed without moving the rods, since the additional thermal flux tilting produced by the rods is then removed from the spatial behaviour of the flux and xenon fields. It can then be determined by comparison whether the spatial rod movements produced a decrease or an increase in the degree of inherent xenon damping, i.e. if the influence of the rods on damping stability is positive or negative.

To obtain the necessary oscillation damping ratio data from the TINTE spatial data, as presented in this study in Sections 4.2.4 and 5.3, a non-linear least-squares fit approach was implemented in the TINTE post-processor utility code NAOMI. The Levenberg-Marquardt algorithm was chosen as the numerical driver for this study, since it is a fast and effective technique for solving nonlinear least-squares problems, and is freely available in the public domain [18] - [21]. It is an iterative technique that finds a local minimum of a function that is expressed as the sum of squares of nonlinear functions. It can be regarded as a combination of steepest descent and the Gauss-Newton method. When the current solution is far from the converged final solution, the algorithm behaves like a steepest descent method: slow, but guaranteed to converge. When the current solution is close to the correct solution, it becomes a Gauss-Newton method.

The least squares regression uses the Levmar library (v2.1.2) [21], which is a GPL native ANSI C implementation of the Levenberg-Marquardt optimization algorithm. The internal Levmar LU-based linear systems solver is used for matrix inversion. The least squares regression is packaged as an open source ".dll" file compiled with Microsoft Visual C++, version 6, and solves the regression expression

$$f(t) = A\, e^{-bt} \sin(Ct + D) \tag{2.6}$$

This expression is the general solution for a damped free oscillation mode in linear perturbation theory [22] in terms of a sinusoidal expression, with A the initial amplitude of the oscillation, b the damping constant and C and D period offset variables. (In [22] the more complex form of this expression is used. It is included in this study as Eq. (2.11)). The matrix to minimize therefore is

$$\mathbf{F} = \begin{bmatrix} A\, e^{-bt_1} \sin(Ct_1 + D) - f_1 \\ A\, e^{-bt_2} \sin(Ct_2 + D) - f_2 \\ \vdots \\ A\, e^{-bt_n} \sin(Ct_n + D) - f_n \end{bmatrix} \tag{2.7}$$

with the associated Jacobian matrix

$$J = \begin{bmatrix} e^{-bt_1}\sin(Ct_1+D) & At_1e^{-bt_1}\sin(Ct_1+D) & At_1e^{-bt_1}\cos(Ct_1+D) & Ae^{-bt_1}\cos(Ct_1+D) & 1 \\ e^{-bt_2}\sin(Ct_2+D) & At_2e^{-bt_2}\sin(Ct_2+D) & At_2e^{-bt_2}\cos(Ct_2+D) & Ae^{-bt_2}\cos(Ct_2+D) & 1 \\ \vdots & \vdots & \vdots & \vdots & \vdots \\ e^{-bt_n}\sin(Ct_n+D) & At_ne^{-bt_n}\sin(Ct_n+D) & At_ne^{-bt_n}\cos(Ct_n+D) & Ae^{-bt_n}\cos(Ct_n+D) & 1 \end{bmatrix}$$

The matrix calculations are implemented as C functions, and passed to the Levmar library for the least-squares minimization. Error estimates are also performed as part of the implementation of the package. The absolute error R^2 is defined as

$$R^2 = \sum_{i=1}^{N} (f_i - f(t_i))^2 . \qquad (2.8)$$

Additionally, a fit "quality" factor is defined as

$$Quality = 100R^2 / A \qquad (2.9)$$

i.e. the R^2 value divided by the starting amplitude of the variable spatial function.

The main outputs of this algorithm are the variables A, b, C and D, which are used to calculate the oscillation parameter of interest for this study, the damping ratio ξ, as follows:

1. If (2.6) is written in terms of the xenon number density $N_{Xe}(t)$ (for example), we obtain

   $$N_{Xe}(t) = N_{Xe}(t_0)e^{-bt}\sin(Ct + D) \qquad (2.10)$$

   where b is now defined specifically as the xenon oscillation damping constant. Note that if $b > 0$, it describes damped or converging oscillations, while a value of $b < 0$ describes un-damped or diverging oscillations. The period of the oscillation is given by $T = 2\pi / C$.

2. This format (2.10) of the general oscillation solution proved to converge faster when compared with the more complex approach that included both sine and cosine terms, which can be written as [22]

   $$N_{Xe}(t) = e^{-\xi\omega_n t}\left\{N_{Xe}(t_0)\cos\omega_D t + \left[\frac{\dot{N}_{Xe}(t_0) + \zeta\omega_n N_{Xe}(t_0)}{\omega_D}\right]\sin\omega_D t\right\} \qquad (2.11)$$

   where

   ξ = damping ratio, defined as the fraction of the current damping constant value to the critical damping constant value where no oscillations occur, i.e. $\xi = b / b_{cr}$. Critically damped systems have damping ratios of 1, or $b = b_{cr}$.

   ω_n = natural frequency of the system without any damping

ω_D = natural frequency of the system with damping

$N_{Xe}(t_0)$ = number density of xenon at time $t = t_0$ (i.e. the steady-state xenon number density). Note that this value can be space-dependent (e.g. the values produced by TINTE), or a core-averaged value.

3. The expressions (2.10) and (2.11) can be related as follows:

$$\begin{aligned} N_{Xe}(t) &= N_{Xe}(t_0)\, e^{-bt} \sin(Ct + D) \\ &= N_{Xe}(t_0)\, e^{-bt} (\sin Ct \cos D + \cos Ct \sin D) \\ &= e^{-bt} (P \cos Ct + Q \sin Ct) \end{aligned}$$

with

$P = N_{Xe}(t_0) \sin D$ and $Q = N_{Xe}(t_0) \cos D$.

This is equivalent to

$$e^{-\zeta\omega_n t} (P \cos \omega_D t + Q \sin \omega_D t)$$

with $C = \omega_D$ and $b = \zeta\omega_n$.

From the above, the damping ratio ξ can be determined from the least-squares fit variables b and C in (2.10) by

$$\begin{aligned} \omega_D &= \omega_n \sqrt{1 - \xi^2} \\ \therefore C &= \frac{b}{\zeta} \sqrt{1 - \xi^2} = b \sqrt{\frac{1}{\xi^2} - 1} \qquad (2.12) \\ \therefore \xi &= \sqrt{\frac{b^2}{b^2 + C^2}} \end{aligned}$$

4. The period of the damped oscillation, T_D, is related to the natural period (of the un-damped oscillation) T_n by

$$T_D = T_n / \sqrt{1 - \xi^2} \qquad (2.13)$$

which implies that damping has the effect of lowering the natural frequency from ω_n to ω_D, or increasing the period from T_n to T_D. Typically this is not an important effect for $\xi < 0.2$, but in the case of the PBMR values (ξ between 0.4-0.6, see Chapters 5 and 6 for detail), the damped period can be significantly longer than the natural period.

The expressions derived here for the damping ratio ξ (2.12) and the damped period T_D (2.13) will be used in Chapters 4 to 7 to quantify the PBMR xenon stability for a large number of transients, by using the least-square fitting data values for the parameters b and C to determine ξ and T_D.

Two graphical examples of the influence of the damping ratio ξ on the rate at which a free oscillation decay are shown in Figure 2-4 and Figure 2-5.

The figures present the oscillatory behaviour of four hypothetical systems with identical damped periods T_D and normalised amplitudes $u(t)/u(0)$, but with different damping ratios 0.1, 0.2, 0.5 and 0.8. (Note that DR = Damping ratio in the figure legends, and DR = 10% is equivalent to $\xi = 0.1$).

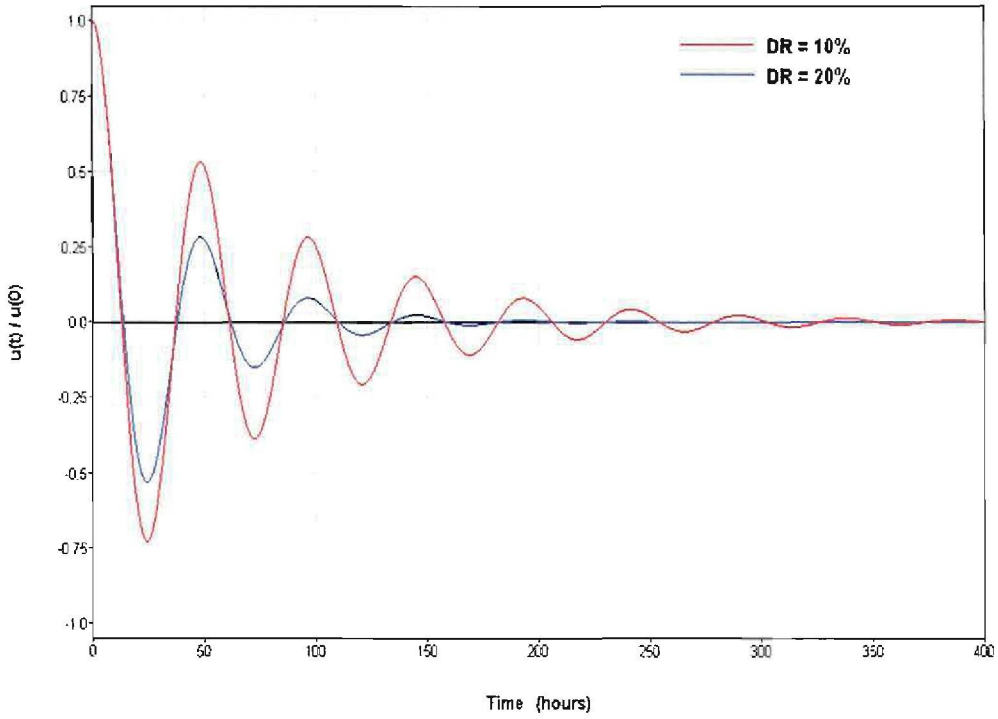

Figure 2-4: Oscillation damping for ξ values of 0.1 and 0.2

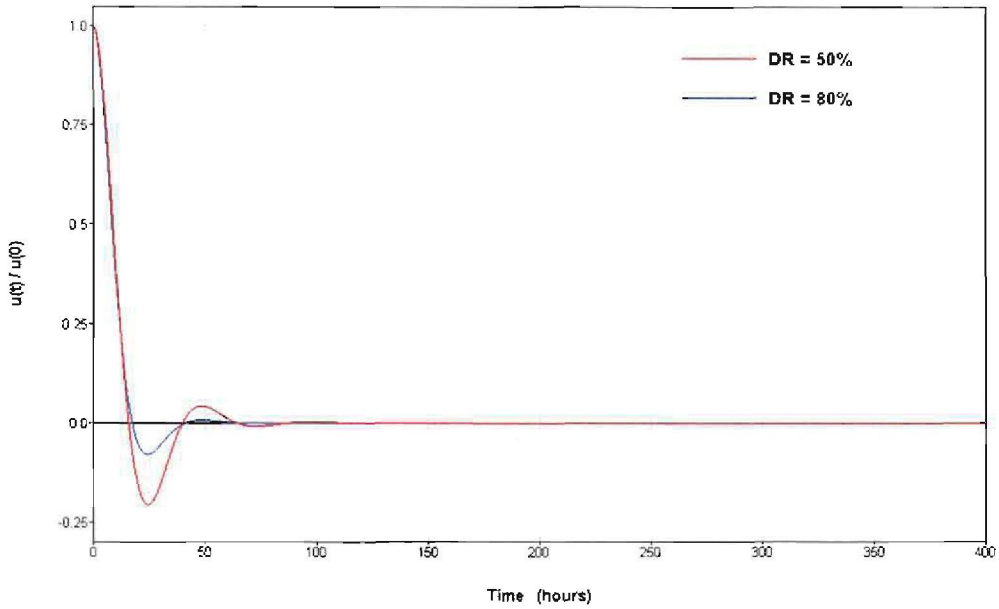

Figure 2-5: Oscillation damping for ξ values of 0.5 and 0.8

2.4 SUMMARY

An overview of the theoretical principles of spatial xenon-induced power oscillations in thermal reactors was presented in this chapter. The main characteristics of the parameters driving the complex iodine-xenon-thermal flux interactions were discussed, and a historical overview was given on the findings of previous HTR-specific studies.

In the final section of the chapter, the least-squares methodology implemented as part of this study for the quantification of the TINTE oscillation data was presented. This formalism is used for the first time in Section 4.2.4, and subsequently also in Chapters 5 to 7, to determine the axial oscillation damping properties of several transient cases. In the next chapter, background information is given on the current PBMR design, as well as a short description of the TINTE code, where after the first detailed results of the PBMR inherent xenon stability is presented in Chapter 4.

CHAPTER 3

3. OVERVIEW OF THE 400 MW PBMR DESIGN AND THE TINTE CODE

3.1 OVERVIEW OF THE 400 MW PBMR DESIGN

The current PBMR design is for a 400 MW equilibrium cycle, loaded with 6 cm diameter graphite fuel spheres that contain a uranium loading of 9 grams, enriched to 9.6%. In the multi-pass fuel management scheme the fuel pebbles pass six times through the reactor before reaching the target burn-up. The PBMR is a high-temperature helium-cooled, graphite moderated pebble bed reactor with a multi-pass fuelling scheme and annular core geometry. Coupled to the reactor is a power conversion unit, which comprises of a single shaft turbo-generator unit, based upon a recuperated, direct, closed-circuit helium cycle. A schematic layout of the main primary and secondary system components of the PBMR is shown in Figure 3-1, together with arrows showing the flow of cold and hot helium through the system.

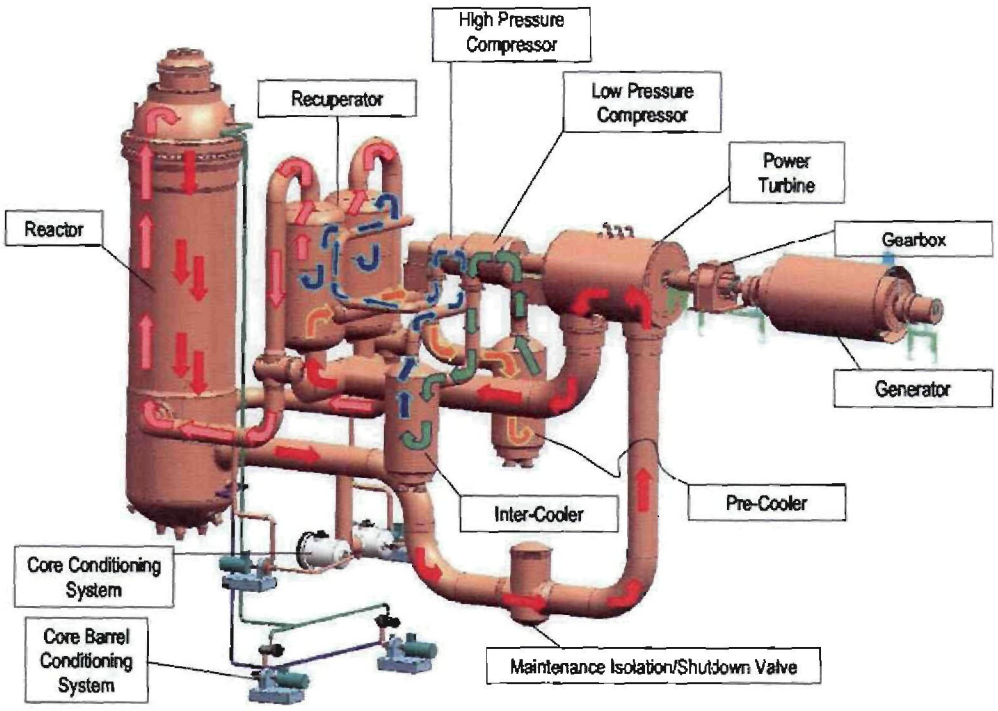

Figure 3-1: Schematic layout of the PBMR design

Reitsma [3] lists the main characteristics of the PBMR core design, apart from those already indicated, as follows:

- an annular core with an outer diameter of 3.7 m and a fixed central reflector with an outer diameter of 2 m,

- an effective cylindrical core height of 11 m,
- a graphite side reflector of ~ 90 cm,
- the reactivity control system (RCS) consisting of 24 partial length control rod positions in the side reflector, with 12 upper and 12 lower rods, when fully inserted. The rods have an effective length (neutron absorbing material) of 6.5 m,
- the reserve shutdown system (RSS) consisting of eight small absorber sphere (SAS) systems positioned in the fixed central reflector and filled with 1 cm diameter absorber spheres containing B_4C when required,
- three fuel loading positions and three fuel unloading tubes, positioned equidistant in the centre of the fuel annulus.

A detail vertical diagram of the PBMR core components is presented in Figure 3-2.

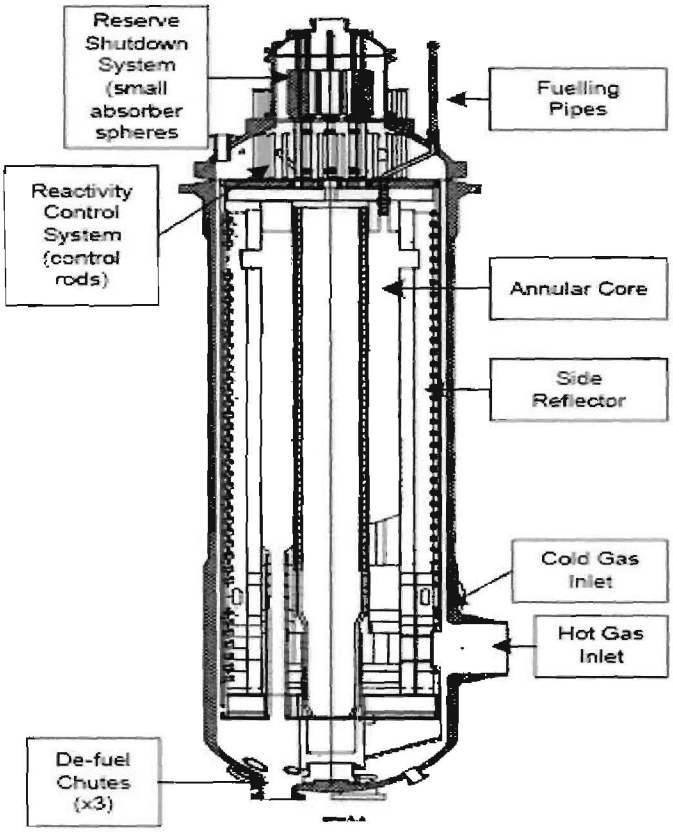

Figure 3-2: Cross-sectional view of the PBMR core [4]

The 400 MW version of the PBMR design uses as thermal-hydraulic boundary conditions a helium inlet/outlet temperature of 500°C/900 °C, a mass flow rate of 192.7 kg/s at the inlet, and an inlet pressure of 9000 kPa.

As part of the basic design principles of a Generation IV type reactor, defence-in-depth against possible operational occurrences and accidents is ensured by several inherent safety features, fuel design and heat removal via natural processes. The main safety features are as follows:

- The TRISO fuel design combines the excellent fission product retention capabilities of the SiC coated fuel kernels with the large heat capacity of the graphite matrix material. Figure 3-3 shows the material composition of a PBMR fuel sphere, as well as the sizes of the various layers.

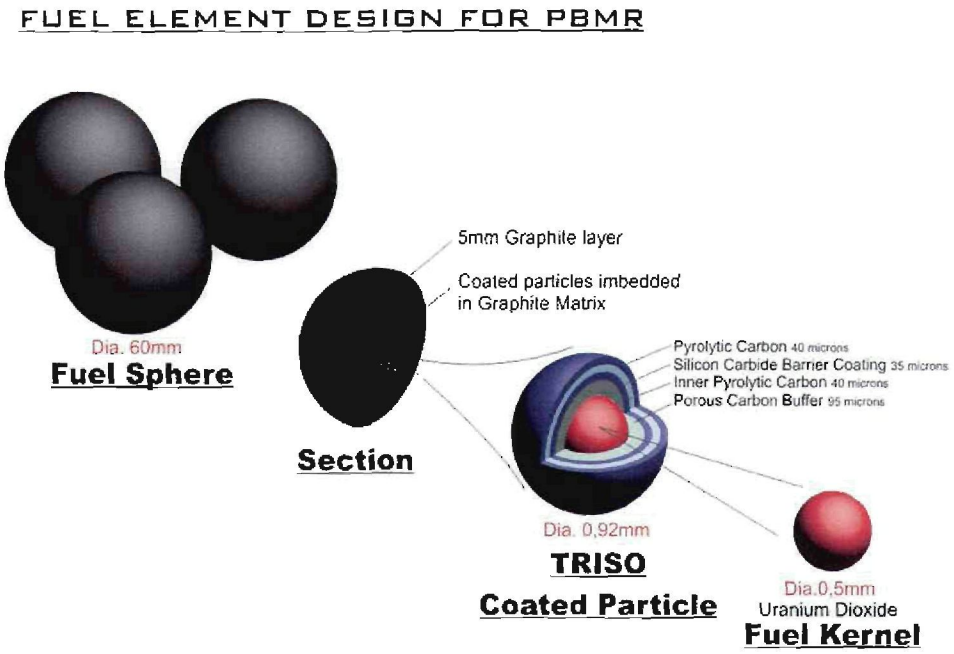

Figure 3-3: Fuel element design for the PBMR

- A low core power density (< 5 W/cm^3) guarantees a relatively small heat load on all core components during operational transients.
- The small amount of excess positive reactivity that can be attained by continuous fuel loading limits fuel temperatures during possible reactivity accidents.
- The passive heat removal path from the fuel region outwards towards the radial core barrel and reactor pressure vessel (RPV) ensures that no active safety systems are needed for the removal of decay heat during loss for forced cooling accidents. Heat flow to the outer boundaries (from the RPV to the reactor cavity cooling system (RCCS) and the concrete of the citadel wall) is ensured primarily through radiation, conduction and natural convection, as shown in Figure 3-4.

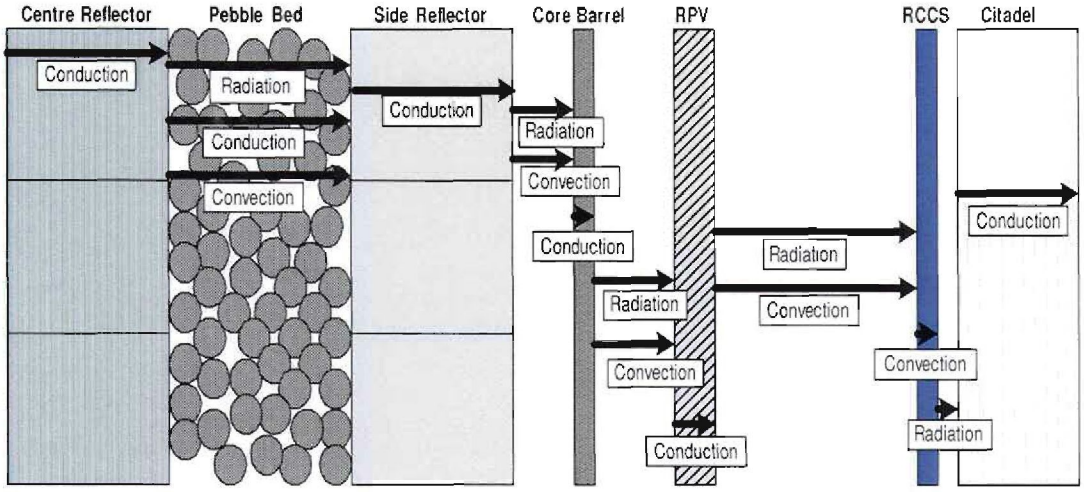

Figure 3-4: Passive heat removal path in the PBMR

3.2 OVERVIEW OF THE TINTE CODE

The TINTE (**Ti**me Dependent **N**eutronics and **Te**mperatures) code [5] was developed to investigate the nuclear and thermal transient behavior of high temperature reactors, with full neutron, temperature and xenon feedback effects taken into account in two-dimensional r-z geometry. The code was developed by KFA (Kernforschungsanlage), today Forschungszentrum Jülich from the 1980's onwards, and obtained by Pebble Bed Modular Reactor company under a license agreement in 2001. The main time-dependent calculation components are:

1. the neutron flux distribution, in two energy groups and six delayed neutron groups,
2. the nuclear heat source distribution, including local and non-local energy distribution fractions,
3. the heat transport from the fuel kernels to the fuel sphere surface,
4. the time-dependent global temperature distribution,
5. the coolant gas flow distribution for a specified mass flow or pressure gradient
6. convection and its feedback on circulation,
7. the gas mixing effects (for multiple gasses present in the system) in the model, including corrosion interactions between the gases and solid structures.

The code incorporates numerous material property correlations for graphite and other core structures, including the temperature and fast-fluence dependence of the pebble-bed effective thermal conductivity. Several benchmarks have shown that the code is suited for the accurate determination of the fast and thermal neutron flux distribution in the axial and radial dimensions [5], with full feedback from all the important neutron poisons, fuel and moderator temperatures, as well as neutron leakage in the spatial domain.

Validation of the TINTE code against AVR operational data [23] has specifically shown that the code is capable of accurately determining the complex variations in the thermal flux, iodine and xenon variables. The inherent limitations of the code (diffusion theory approach, two energy groups and two spatial dimensions) do not restrict its application in this study to determine the radial and axial xenon oscillation stability of the PBMR design, since the level of accuracy possible with the code is sufficient for a large quantitative study involving short-duration transients.

TINTE uses a one-dimensional leakage iteration method to solve the two-dimensional partial differential equations resulting from neutron and heat diffusion theory [5], [24]. This method makes it possible to solve the differential equations in a one-dimensional fine grid, where first the radial, and then the axial components of the neutron fluxes and partial currents are determined. The coupling between the radial and axial regions is obtained from the leakage terms in the 1-D calculations, and an iteration scheme is applied until both transverse calculations converge for each coarse-mesh region.

The partial problems of a reactor calculation are solved separately in TINTE, i.e. the partial solutions are explicitly coupled. The partial solutions include the following:

- The nuclear calculation – a neutronic calculation is performed to determine the time-dependent flux distribution, and the power distribution is calculated from this reaction rate.
- The temperature calculation – heat transfer calculations are performed to determine the time-dependent temperature distribution of the calculation domain. This includes gas flow, convection, solid conduction and radiation heat transfer calculations. Because of the relatively short periods associated with neutronic calculations, several nuclear time intervals are used within each temperature/chemistry calculation.

This solution scheme principle is shown in Figure 3-5, where Δt_N represents the nuclear time step size, and Δt_T the temperature time step size. Separate temperature and nuclear time intervals are therefore defined. The TINTE nuclear calculation structure is depicted in more detail in Figure 3-6. Initially, fuel and moderator temperatures are required for the cross-section calculation. Because multiple nuclear time intervals are used per temperature interval, these values are available for the first nuclear interval. For the subsequent nuclear intervals within the temperature interval the fuel and moderator temperatures are calculated by temporal extrapolation of previous temperatures. During the inner flux iteration the xenon concentrations are first adjusted according to the guessed neutron flux distribution for the time interval. These concentrations are used to update the neutron absorption of the material blocks.

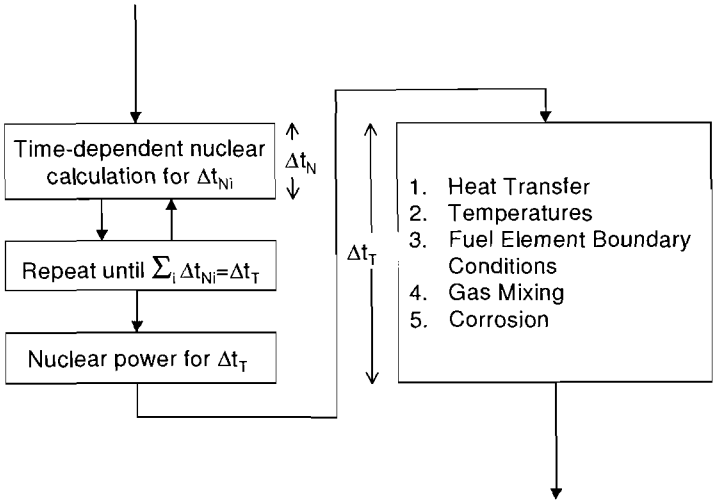

Figure 3-5: The modular structure of TINTE: principle of time discretization [24]

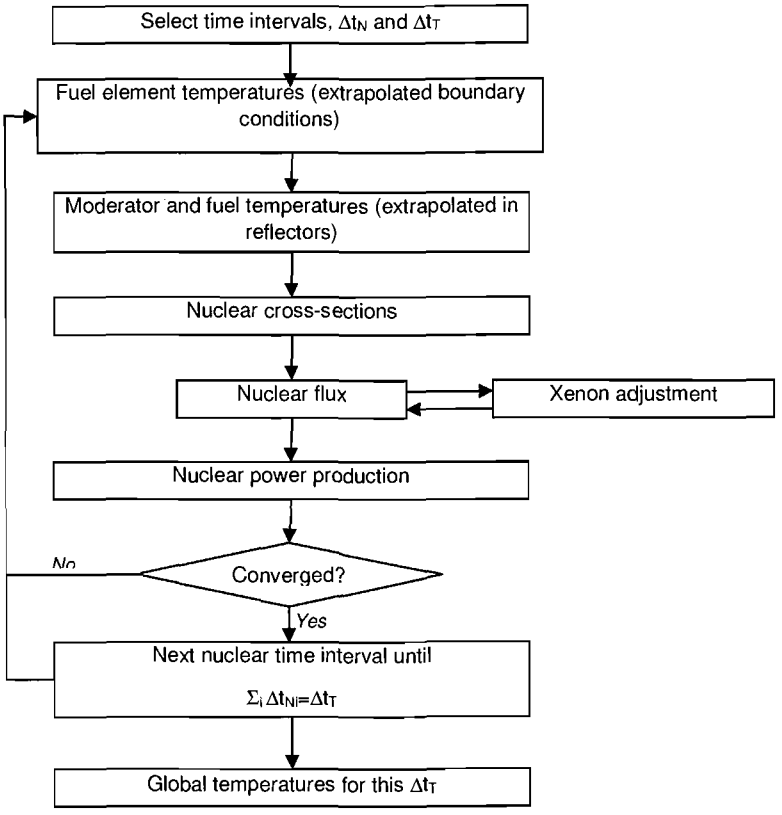

Figure 3-6: The TINTE nuclear calculation [24]

A flux calculation is then performed to update the flux distribution. The neutron flux inner iteration is repeated until convergence of the flux distribution is obtained. The spatial fission power distribution for the time-interval is then calculated. In transient cases, the power distribution is fed back into the fuel and moderator temperature calculation. Therefore an intermediate power iteration is repeated until convergence is obtained. This represents the converged solution for a single nuclear time interval. This procedure is repeated for all nuclear intervals within the current temperature time interval. The effective nuclear power in each material mesh block, for the temperature interval, is then calculated as the average power for all the nuclear subintervals.

3.3 SUMMARY

An overview of the PBMR design and its main nuclear safety features was given in this chapter. It was discussed that the TRISO fuel design, the low core power density and the passive heat removal path all contribute to the PBMR's claim of passive safety, which enables the current design to guarantee sufficient heat removal under all operating and accident conditions.

The second section of this chapter presented a short summary of the capabilities of the TINTE HTR reactor dynamics code, with specific focus on its nuclear calculation structure. It was illustrated where the flux and xenon calculations fit into the bigger TINTE solution scheme, and the validity of utilising TINTE for the quantification of xenon-induced spatial power oscillations has also been established.

CHAPTER 4

4. RESULTS AND DISCUSSION OF THE PBMR 400 MW INHERENT AXIAL XENON STABILITY

4.1 INTRODUCTION

The first quantitative results on the PBMR xenon axial oscillation stability investigation are presented in this chapter. The focus here is on the PBMR's inherent stability (the definition is given below), while chapter 5 contains the results of the 100%-40%-100% load-follow transient.

The inherent power density axial oscillation damping properties of the PBMR design are firstly determined in Section 4.2 by analysing a set of intentionally initiated free oscillations, i.e. without any external influences on the spatial flux shapes during the oscillation phase. These artificial transients consist of inserting the control rods for a short period of time (to cause a strong initial spatial disturbance in the neutron flux/xenon fields), followed by the return of the control rods to their default position. The core total power is kept constant during these events by a space-independent control option. No other control rod movements are performed for the remainder of these transients, and the events are performed for several steady-state power levels (20%, 50%, 80% and 100%) to quantify the effect of different core operational states on the degree of power/xenon oscillation damping.

After the inherent damping properties of the PBMR design have been determined by utilising artificial transients, the effect of control rod movements on the xenon and thermal flux space-time behaviour during realistic operational power load-follow events are presented in Chapters 5 and 6.

Due to the nature and scope of the PBMR xenon stability study, a large number of cases were calculated with the TINTE code, and a lot of post-processing graphical information and least-square fitting data were produced (more than 500 plots were created for this study). It is clear that this study can only contain a fraction of this total available graphical dataset, and even less if summary tables and other case information need to be included as well. The approach followed in compiling the results of this study therefore is as follows:

- Graphical representation of data will only be used to inform the reader of typical behaviours for the identified parameters.
- Data plots can be used to "visually convince" the reader of the oscillatory nature of these transients, the degree of damping exhibited, and the accuracy of the least-square fitting routine. However, the quantitative data will be summarised in tables for most of the cases, together with typical error estimates.

Two "reference" cases are discussed in some detail: the 100% power control rod bank insertion for a certain excitation period (case 1), and an example of a 100%-40%-100% load-follow transient (case 5). These cases represent the two classes of transients that have been studied, and a fair number of graphical information is supplied in this chapter during the discussion of the results. Further cases of the same class in chapters 5 and 6 are not discussed in such detail, and only the most important parameters are summarised in tables.

4.2 CASES 1 TO 4: INHERENT XENON-INDUCED OSCILLATION PROPERTIES OF THE PBMR 400 MW EQUILIBRIUM CORE

In this section, the inherent xenon and power density oscillation properties of the PBMR equilibrium 400 MW core state are firstly determined by analyzing a set of *free* oscillations, i.e. without any external influences on the spatial flux shapes or xenon concentration levels during the oscillation phase. Cases 1 to 4 consist of inserting the control rods three meters deeper than the nominal location at four different steady-state power levels; i.e. 80 MW (20% of the nominal power level), 200 MW (50%), 320 MW (80%) and 400 MW (100%). All four cases utilise inserted control rod periods of four hours, to excite strong spatial disturbances in the neutron flux/xenon fields in the top part of the core. The control rods are returned to their nominal location after this period, and no other control rod movements were performed for the remainder of these transients.

These cases are designed to study the nature and effects of axial power oscillations at a constant global reactor power. Since the insertion of the control rods lead to sub-critical core states, a global external reactivity control option in TINTE is utilized to keep the core power levels constant throughout the transients. (This simulates the control of the core reactivity by the addition of a global poison, for example. This type of global control is not possible in the PBMR design). To ensure that the rods were inserted in a consistent manner, all cases included a relative control rod banks insertion distance of 3 m from their respective steady-state locations, as shown in Table 4-1.

Table 4-1: Control rod depths for cases 1-4

Case # and description	Steady-state control rod depth (cm)	Inserted control rod depth (cm)
1: 100% power	200	500
2: 80% power	230	530
3: 50% power	280	580
4: 20% power	380	680

4.2.1 Global Results

Figure 4-1 and Figure 4-2 present the control rod depth variations and core-averaged xenon absorption levels for cases 1-4. The decrease in the core-averaged xenon levels can be seen for all cases from 1-5 h when the control rods are at their inserted locations, as well as the subsequent global xenon build-up and decay when the rods are returned to their nominal locations.

The global xenon levels show the typical decay and build-up behaviour for all four cases, with case 1 (400 MW) producing the largest variations in the core-averaged xenon levels. Note that these global xenon variations cannot be classified as fundamental mode global oscillations, since the total power levels stay fixed throughout the transients. (A fundamental mode xenon oscillation is accompanied by a coupled inverse oscillation in the total power levels).

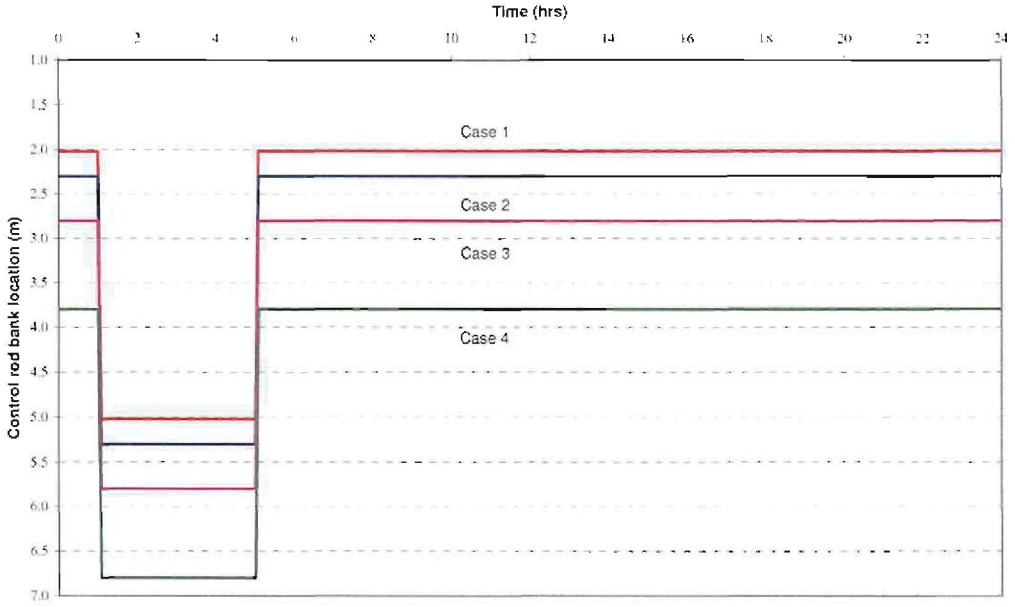

Figure 4-1: Cases 1 to 4 control rod bank insertion depths for the first 24 hours

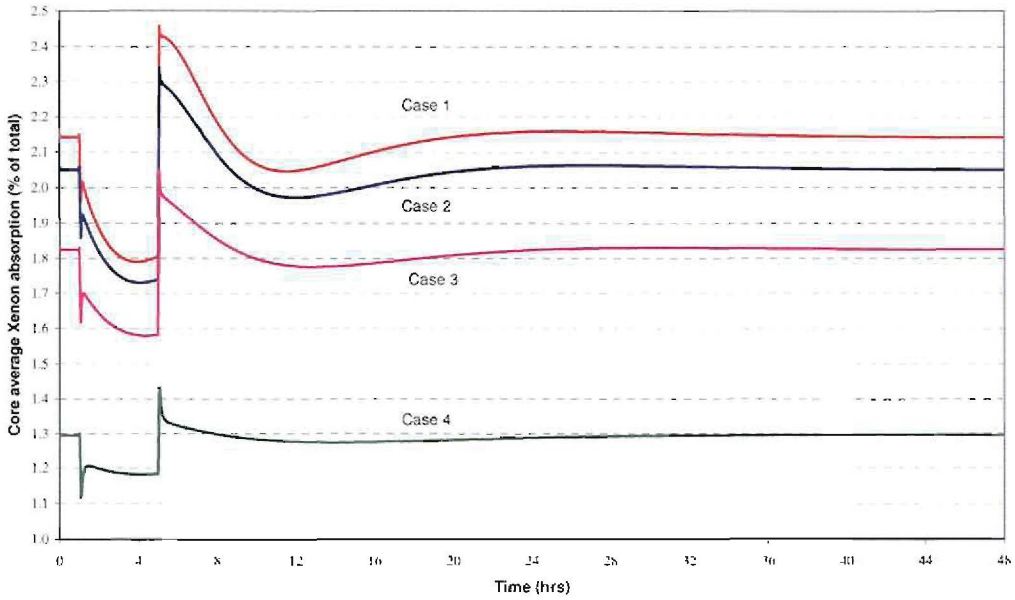

Figure 4-2: Cases 1 to 4 core-averaged xenon absorption variation with time

4.2.2 Spatial Results

Since spatial data for all four cases cannot be presented fully in this study, selected plots for cases 1 and 4, representing the two limiting power values (20% and 100% power), are used as examples of the typical information that can be extracted for the purposes of spatial xenon damping stability studies. Only summarised tabular data will be provided for the other cases.

Figure 4-3 shows the power density (or heat source) spatial oscillations that occur at 7 locations along an axial cut at r = 105 cm, i.e. adjacent to the central reflector. Note that the power density data during the transient phase are normalized to the steady state values. The coordinate designation (r;z) used in Figure 4-3, and throughout this study, indicates the radius r and axial height z of a specific core location. This means that (105; 1000) represents the position at radius r = 105 cm (next to the central reflector), and at an axial height of 1000 cm into the core, or at the bottom of the core. The TINTE axial zero line is located at the bottom of the top reflector.

The insertion of the control rods forces the nominal axial power peak (usually located at z ~ 350 cm) downwards, and the sharp decrease in the power generation in the top area of the core (z = 100-400 cm) is coupled with the increase in the power generation in the bottom areas of the core (z = 600-900 cm), since the total power generated remained constant. Figure 4-3 also clearly shows the difference in magnitude between the forced power variations between 1 and 5 h, and the subsequent free oscillations that proceed from 5 h onwards, when the control rods have stopped moving. This spatial flux oscillation is fully damped out within ~ 48 h, i.e. 43 h after the return of the control rods to their nominal location.

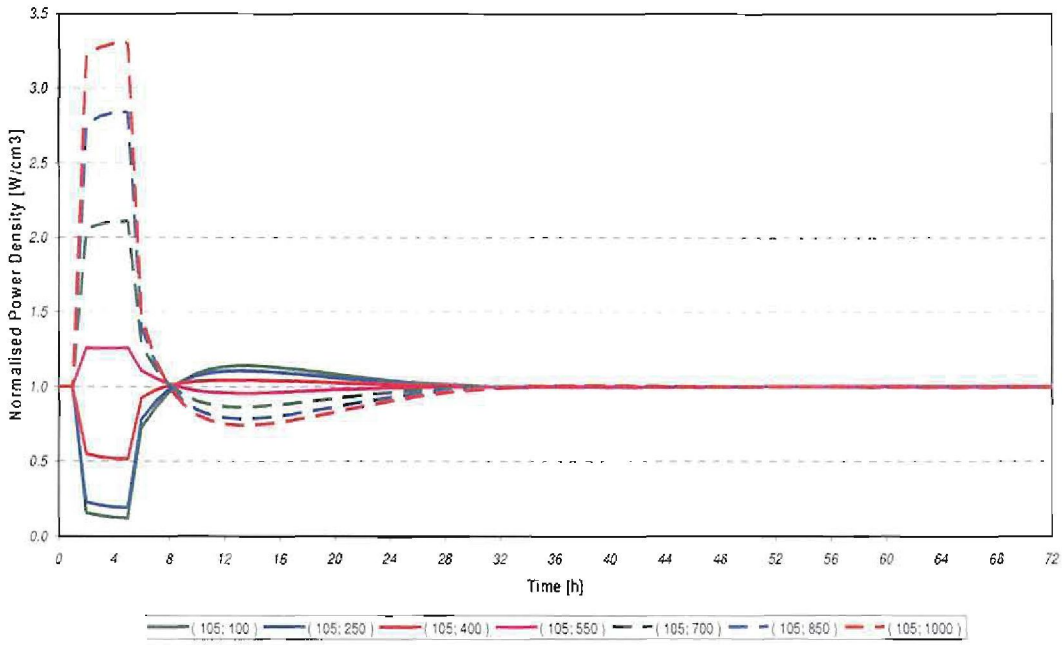

Figure 4-3: Case 1 (100% power) normalized (to steady-state values) axial power density variation at radius r = 105 cm, for various core heights z.

The damped free spatial oscillation between 5 and ~ 48 h, caused by this large flux perturbation, can be seen in more detail in Figure 4-4 (power density) and Figure 4-5 (thermal flux). Locations in the bottom regions of the core (z ~ 800-900 cm) experience the largest deviations from their steady-state values, while the centre of the core (z = 450 - 550 cm) shows only a slight variation.

The variation in the normalised power density for case 4 (20% power) is shown in Figure 4-6. The spatial oscillation behaviour of the low-power case is similar to the high power-case in respect to the spatial behaviour of the power density, but a higher degree of damping is evident for case 4 if the slight overshoot in power at 36 h in Figure 4-4 is compared with the behaviour of the power density in Figure 4-6. The amplitudes and the periods of the two transients also differ quite substantially. The maximum amplitudes of the variations are significantly smaller for case 4 (1.04 at z = 100 cm), compared to variations in power for case 1 (1.15 at the same location). However, it must be kept in mind that the normalisation levels cannot be compared directly, since they are related to two different steady-state power levels (400 MW and 80 MW), with different control rod positions, fuel temperature distributions and k-eff values.

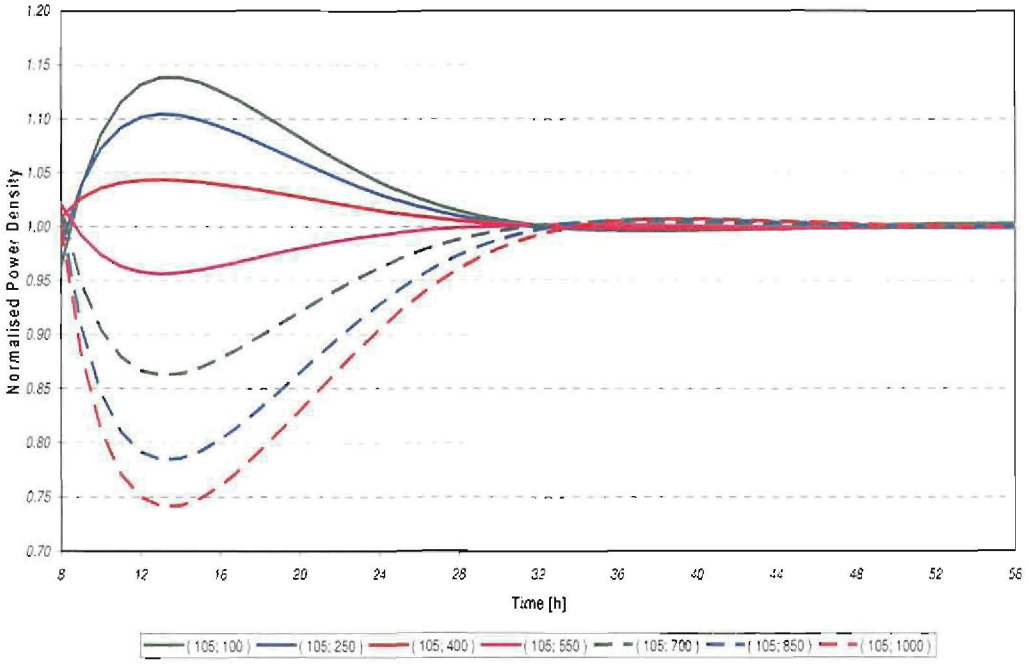

Figure 4-4: Case 1 (100% power) detail of the normalized axial power density variation at radius r = 105 cm, for various core heights z.

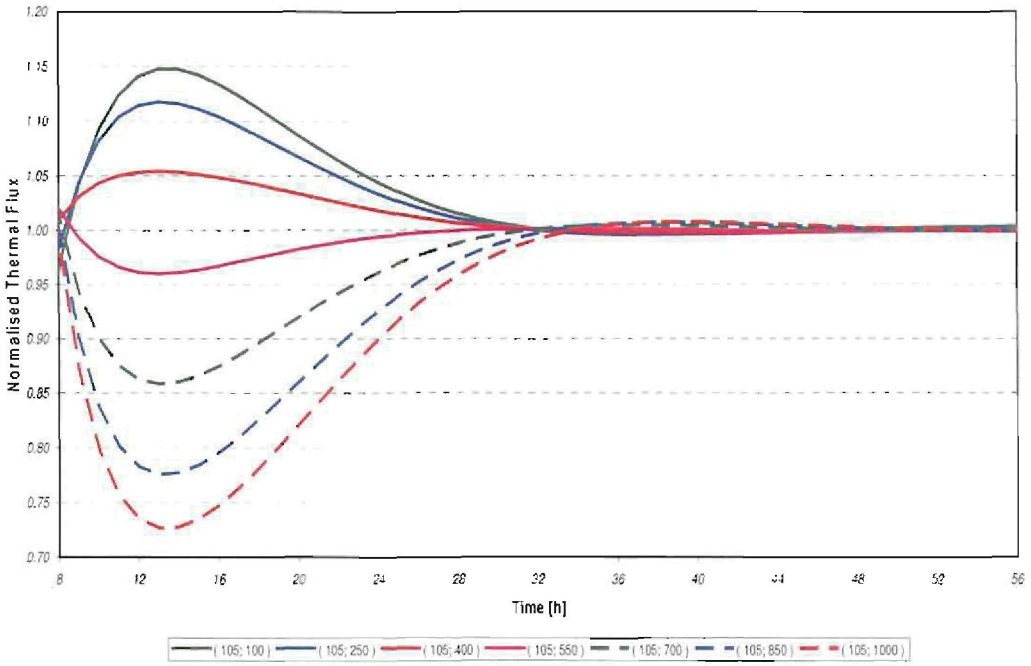

Figure 4-5: Case 1 (100% power) detail of the normalized axial thermal flux variation at radius r = 105 cm, for various core heights z.

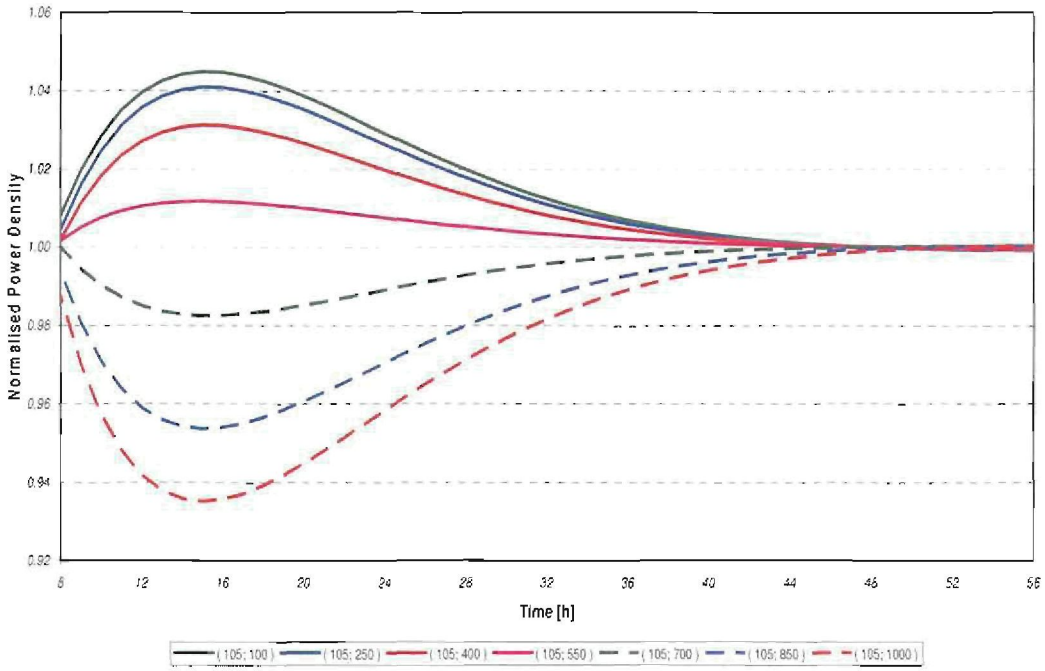

Figure 4-6: Case 4 (20% power) detail of the normalized axial power density variation at radius r = 105 cm, for various core heights z.

Apart from the difference in oscillation amplitude, the damped oscillation period for case 1 also seems shorter (~ 50 h), compared to the case 4 period of ~ 100 h. This is caused by the difference in the degree of damping between the two cases, but it should be noted that an increase in the damping period does not imply a lesser degree of damping. Table 4-8 at the end of this section, actually confirms qualitatively that case 4 is better damped than case 1, in spite of its longer damped period. As indicated in Chapter 2, Eq. (2.13) shows that the natural period T_n and damped periods T_D of an oscillation are related by

$$T_D = T_n / \sqrt{1 - \xi^2} \qquad (2.13)$$

where ξ is the damping ratio of the oscillation. If average values of ξ = 0.51 and T_D = 50 for case 1, and ξ = 0.74 and T_D = 100 for case 4 are used in Eq. (2.9) (from Table 4-8), it results in natural periods of T_n = 43 h (case 1) and T_n = 67 h (case 4). Although the natural oscillation period of case 4 is longer than the natural period for case 1 (67 h vs. 43 h), this difference was actually increased by the higher degree of damping that case 4 exhibits. (The point of this small digression is to stress that using only visual comparisons for this topic is not advisable – numerical data should be determined before final conclusions can be made).

The final difference between case 1 and case 4 is in the behaviour of the central core location (z = 550 cm), which is near to the oscillation node, as is shown in the next section. Figure 4-6 shows that the power density decreases at this location in the period 8-12 h for case 1, while it increases in the same period for case 4. The reason for this is the difference between the insertion and subsequent return depths of the control rods. In case 1, the rods are moved from 200 cm to 500 cm at t = 1 hour, and when the control rods are returned to 200 cm at t = 5 h, the axial power peak shift upwards again. The power density at z = 550 cm therefore increased between 1 and 5 h (Figure 4-3), and slowly returned to its nominal value when the rods were returned to 200 cm. This behaviour is different to case 4, where the deep insertion of the rods (from 380 cm to 680 cm) shifted the axial power peak below 550 cm, and only when the rods were returned again, did the power density increase (and overshoot) to its nominal value.

The normalised xenon concentration levels for case 1 and case 4 are compared in Figure 4-7 and Figure 4-8; again for 7 axial core locations at r = 105 cm. The differences in the xenon levels between the cases are similar to the power density behaviour (case 4 has smaller amplitudes, the z = 550 cm location moves in opposite directions, and case 4 is more slowly damped), but the xenon concentration data show larger variances between the spatial locations. For example, if the xenon levels in Figure 4-7 and Figure 4-8 are compared at z = 850 cm and 1000 cm, a significantly larger difference exists between these two locations for case 4.

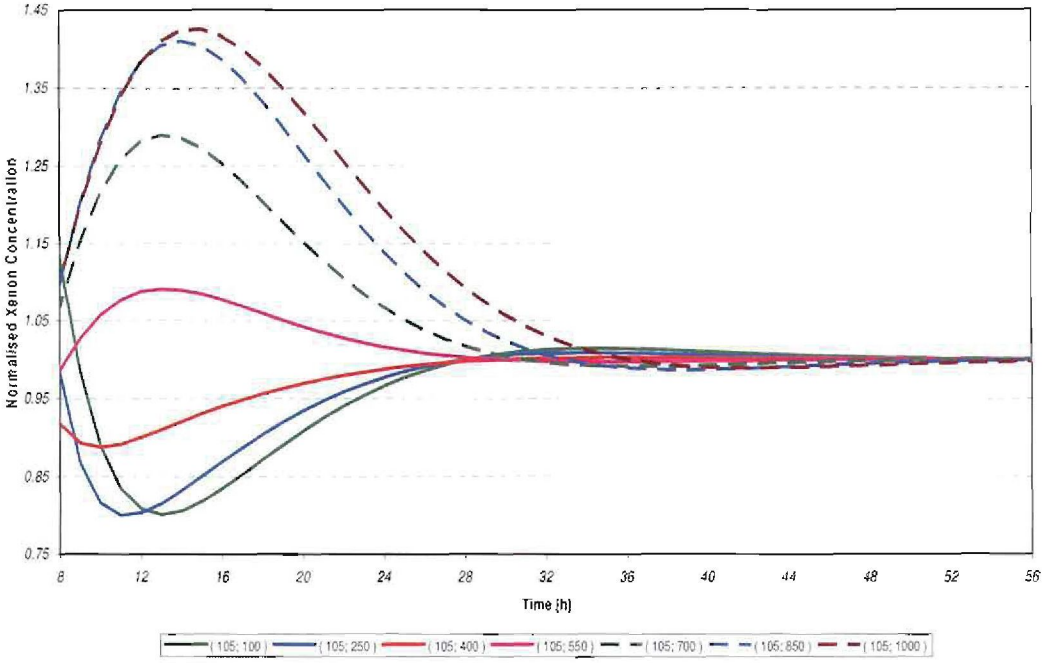

Figure 4-7: Case 1 (100% power) detail of the normalized xenon concentration variation at radius r = 105 cm, for various core heights z.

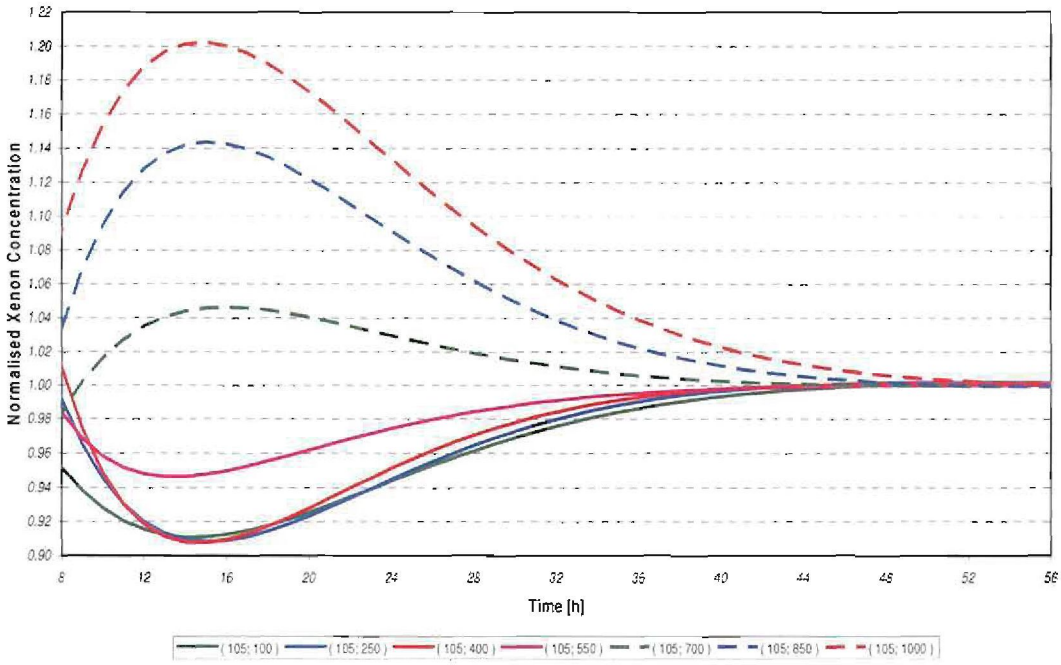

Figure 4-8: Case 4 (100% power) detail of the normalized xenon concentration variation at radius r = 105 cm, for various core heights z.

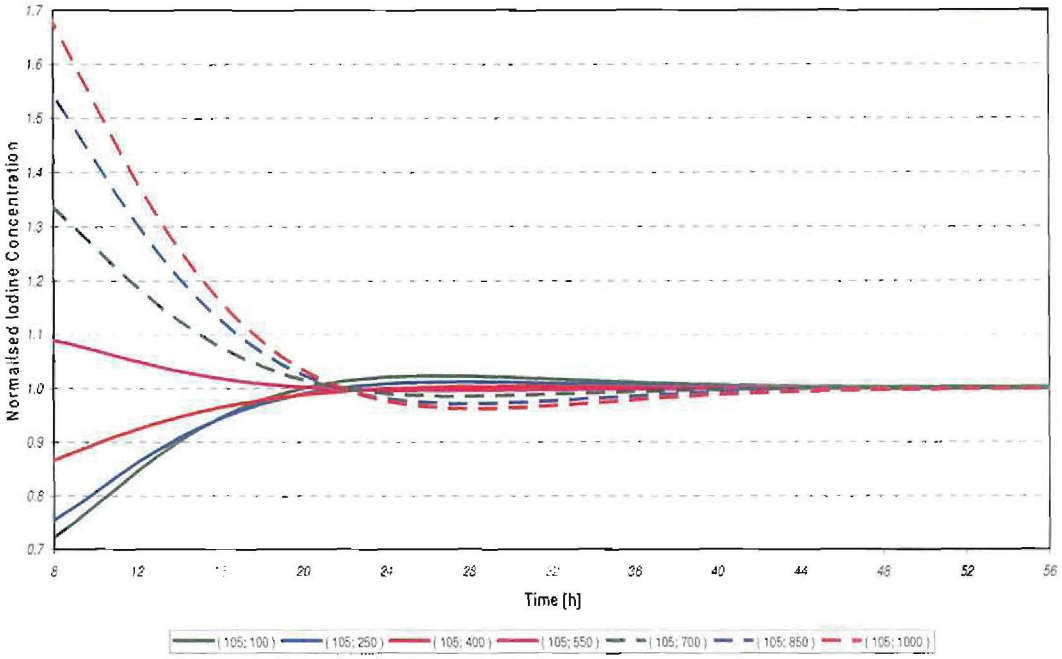

Figure 4-9: Case 1 (100% power) detail of the normalized iodine concentration variation at radius r = 105 cm, for various core heights z.

The normalised iodine concentration levels for case 1, presented above in Figure 4-9, do not seem to show the same temporal behaviour as the flux, power and xenon variables. However, the iodine oscillation is only phase-shifted compared to the flux and xenon levels (e.g. iodine levels decrease immediately after the control rods are returned to their nominal locations, while the xenon levels increase). The difference in the xenon and iodine oscillation amplitudes should also be noted.

Difference function axial and radial cuts

The flux oscillation can be seen in another way by plotting the variation of the thermal flux axial profile for case 1 at selected time points from 13 h to 36 h, as shown in Figure 4-10. In this case, the thermal flux values shown are "difference" values, calculated by subtracting the respective steady-state value from the spatial transient values at a time point. This approach is comparable to the normalized value approach, and enables comparison between the transient behaviour of the four cases. The effect of the damping can be observed as a flattening on the axial flux difference, as the thermal flux axial profile slowly returns to its steady-state shape, and from 36 h onwards there is no discernable difference between the steady state and transient flux values. The oscillation shape is typical of a first axial mode oscillation, with a single oscillation node located at z ~ 490 cm; close the axial centre of the core (the effective, or flattened, core height is approximately 11m).

When the power density variations for case 1 and 4 are compared (Figure 4-11 and Figure 4-12), it can be seen that the deeper location of the control rods for case 4 forces the axial power oscillation node location down to ~ 610 cm, or about 120 cm deeper compared to case 1.

The xenon and iodine variations in Figure 4-13 and Figure 4-14 confirm the general shape of the spatial oscillation and the location of the first axial oscillation node for these two parameters. The location of the first axial node for the xenon and the iodine oscillations is actually similar (at z ~ 490 cm), when Figure 4-13 and Figure 4-14 are compared.

The figures also show the difference between the xenon and flux/power behaviours during the transient, in the sense that increases in the power density or flux values correspond to decreases in the xenon levels.

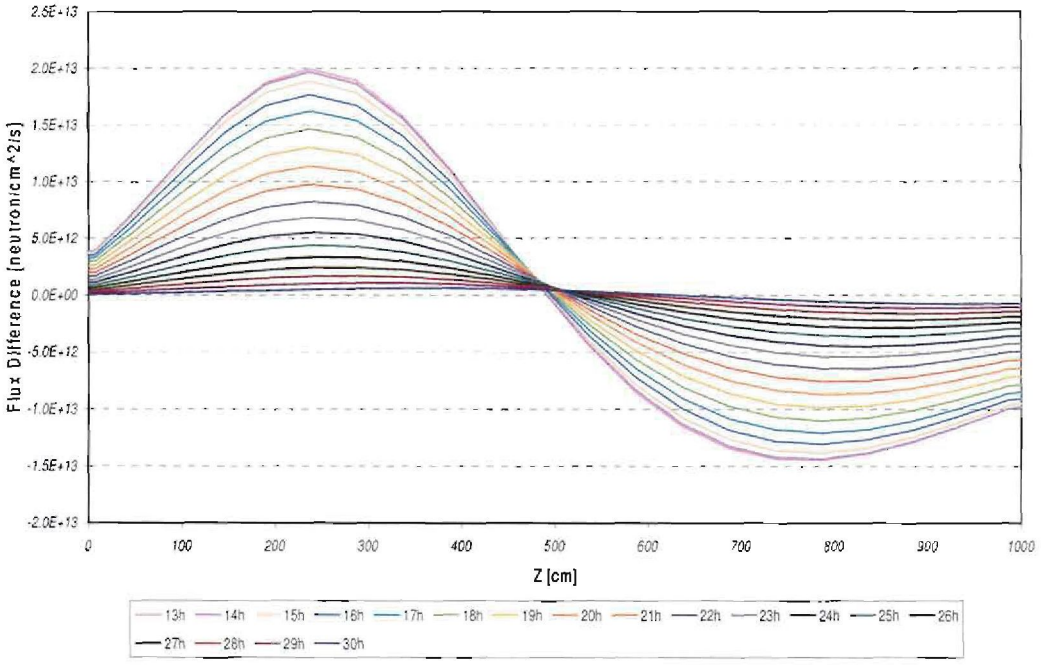

Figure 4-10: Case 1 (100% power) variation in the axial thermal flux difference at radius r = 105 cm, for various time points.

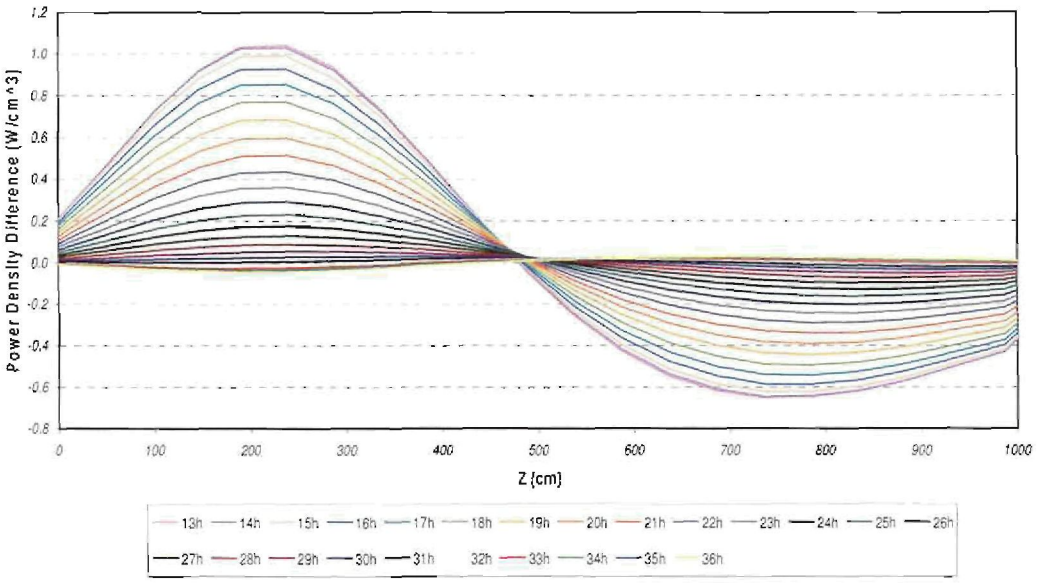

Figure 4-11: Case 1 (100% power) variation in the axial power density difference at radius r = 105 cm, for various time points.

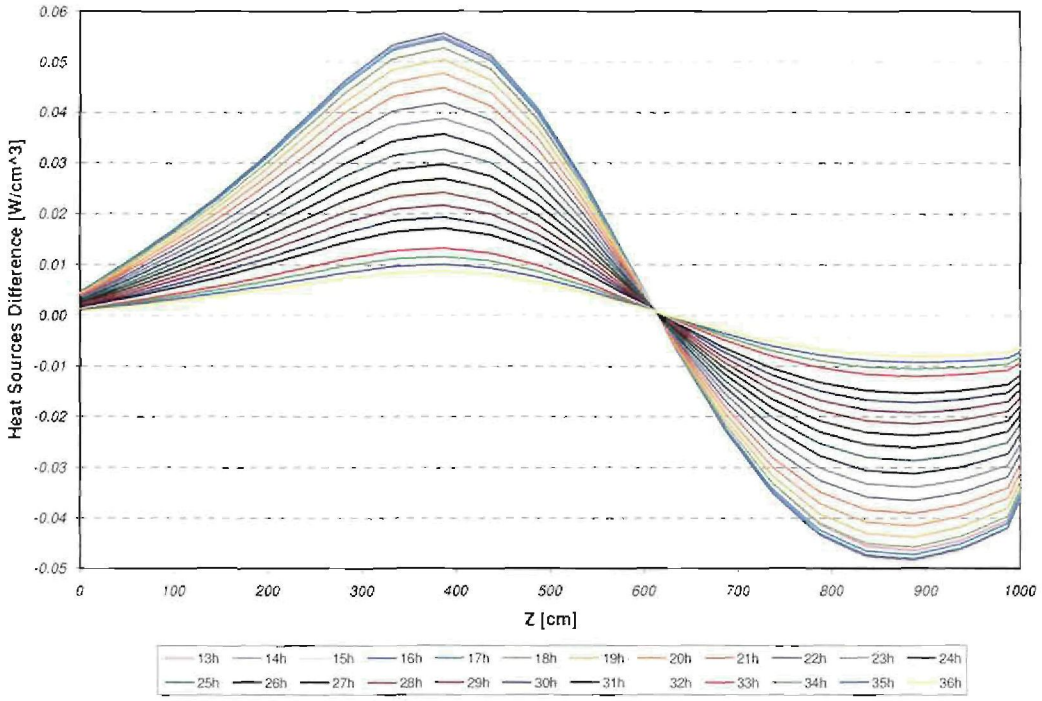

Figure 4-12: Case 4 (20% power) variation in the axial power density difference at radius r = 105 cm, for various time points.

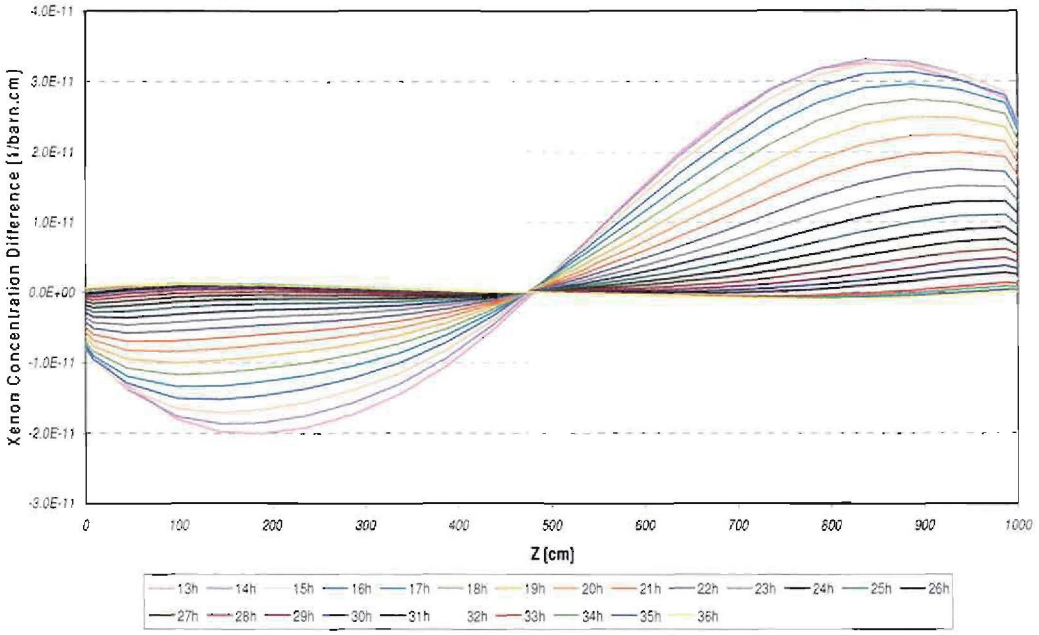

Figure 4-13: Case 1 (100% power) variation in the axial xenon concentration difference at r = 105 cm for various time points.

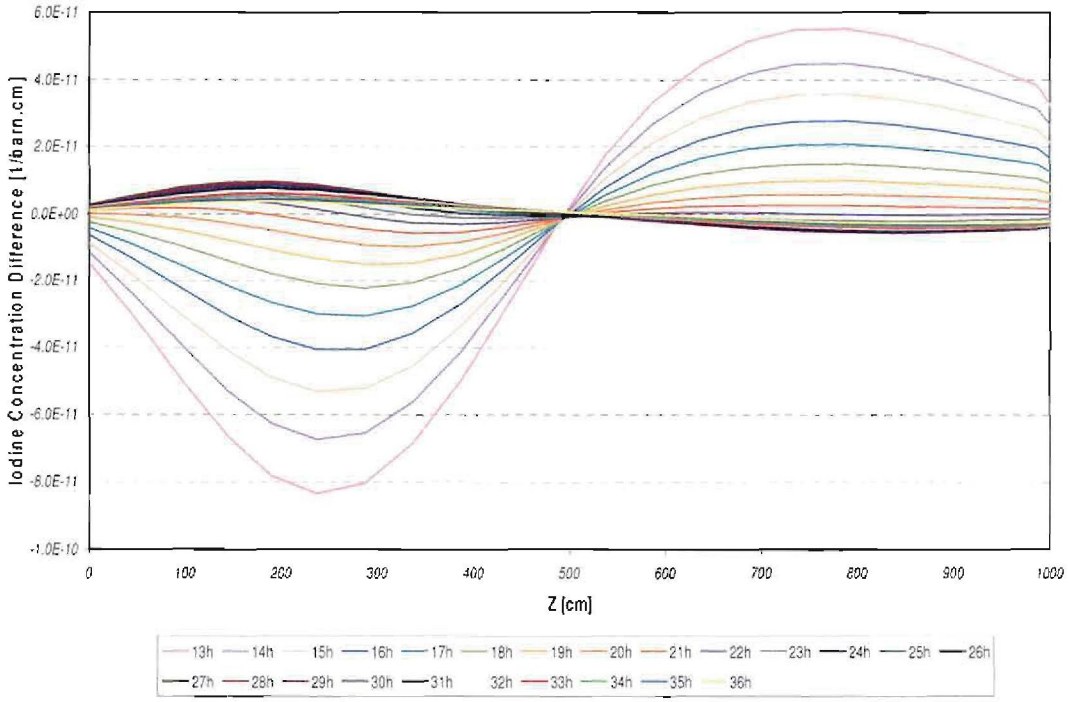

Figure 4-14: Case 1 (100% power) variation in the axial iodine concentration difference at r = 105 cm for various time points.

4.2.3 Radial power and xenon variations

The occurrence of xenon-induced power oscillations in the radial dimension can largely be excluded from this study based on basic xenon theory, since the core annulus radius of 85 cm is only slightly larger than the mean neutron diffusion length in graphite (59 cm). (Expressed differently, the flux/xenon fields are strongly coupled in the radial direction). This implies that flux or xenon changes in the inner part of the annulus will immediately be propagated to the outer part of the annulus as well.

The axial oscillation results obtained in this study seem to confirm a very high radial xenon stability in the PBMR core. The radial power density and xenon concentration difference data for case 1 are presented in Figure 4-15 and Figure 4-16, at z = 800 cm and z = 200 cm, respectively. The data shown in the figures are for the period t = 12 h to t = 36 h, since no radial shape variations occur after this period. The figures show very small radial variations in the power and xenon fluctuations, and only small amplitude variations are present as the axial power shape returns to its steady-state form. For example, the power density vary only by ~ 0.65 W/cm^3 on a nominal value of ~ 10 W/cm^3, in the region adjacent to the central reflector (r = 105 cm).

The absence of any radial xenon or power oscillations components in the PBMR core confirms the expectation that no radial mode oscillations are induced by the axial excitation cases included in this study (see also Chapter 5 for more examples).

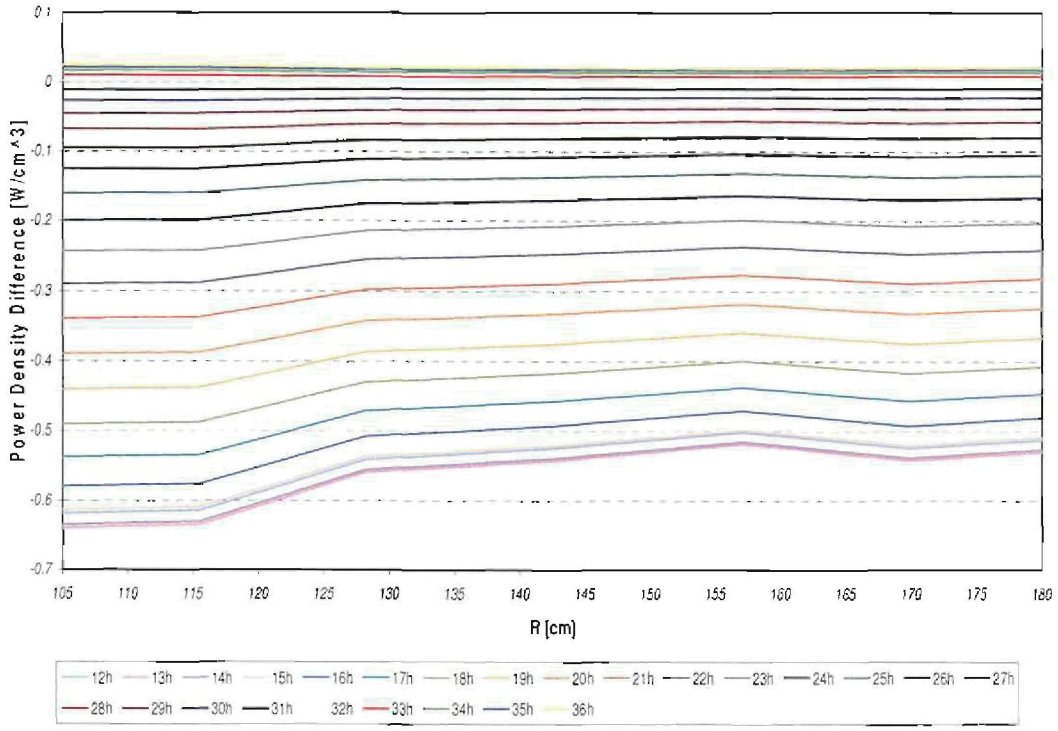

Figure 4-15: Case 1 variation in the radial power density difference at z = 800 cm, for 12 h to 36 h

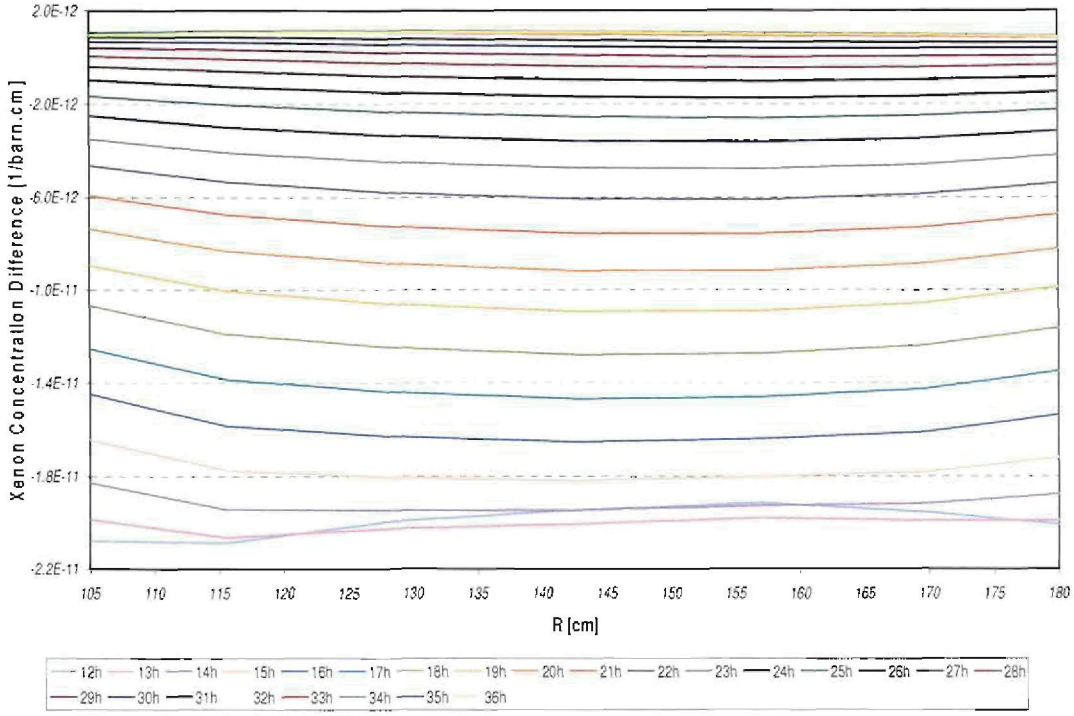

Figure 4-16: Case 1 variation in the radial xenon concentration difference at z = 200 cm.

4.2.4 Spatial Damping Results

In Sections 4.2.1 to 4.2.3, several results from cases 1-4 have been presented on the absolute and normalised variations in the axial and radial xenon and power density fields. In this section, the least-squares fitting routine described in Section 2.3 (see Eq. (2.6) to Eq. (2.13)) is used on the spatial data for cases 1-4 to quantify the inherent axial oscillation damping properties of the PBMR. The xenon and iodine concentrations levels, as well as the fast and thermal flux and power density transient data at 21 spatial points in the core were used as input for data fits (Table 4-2).

Table 4-2: Spatial locations of the least-squares fits

	R = 105 cm (next to central reflector)	R = 140 cm (radial centre of core)	R = 180 cm (next to side reflector)
Axial location	100	100	100
	250	250	250
	400	400	400
	550	550	550
	700	700	700
	850	850	850
	1000	1000	1000

As discussed in Section 2.3, Eq. (2.10), the least-squares fit is applied to the general damped oscillation expression

$$N_{Xe}(t) = N_{Xe}(t_0)e^{-bt}\sin(Ct + D) \tag{4.1}$$

to obtain the variables *b*, *C* and *D*, where

$N_{Xe}(t)$ = number density of xenon at time *t*

$N_{Xe}(t_0)$ = number density of xenon at time t_0. Time t_0 usually defines the starting time point of the fitting function, and since the linear oscillation theory is usually only applied to *free* oscillations (i.e. without any forcing functions or higher modes, for example the flux tilting caused by the movement of the rods), the starting point for the fit and the transient itself is usually not the same.

b = damping constant of the system. It is related to the damping ratio ξ and the terms in Eq. (4.1) by

$$\xi = \sqrt{\frac{b^2}{b^2 + C^2}} \tag{4.2}$$

The least-squares fitting routine utilises the values of *b*, *C*, and *D*, obtained from Eq. (4.1), to calculate the damping ratio ξ from Eq. (4.2), for all spatial fits in a numerical format. Graphical representations of these fits were also implemented for this study, and a limited set of examples of these plots will be included in the following sections.

However, these graphical representations are really only useful to convince the user of high quality fits – the real quantitative statistical data is contained in tabular format, together with data on the error margins for each fit. The fitting routine utilized in this study typically produces linear damping fits with standard errors of less than 0.05%, if the fits are restricted to the free oscillation phases.

Three graphical examples of the least-square fits for case 1 and case 4 are shown in Figure 4-17 to Figure 4-19, where the spatial fitting functions have been overlaid as solid black lines on the original spatial data for comparison purposes. Figure 4-17 and Figure 4-19 present the power density and iodine concentration data for case 1 at r = 105 cm, while Figure 4-18 shows the xenon concentration data at the same location, but for case 4. The fits have only been applied from 10 h onwards, since the initial large perturbations in the power and xenon fields do not form part of the free oscillations phase of the transient. The figures indicate a satisfactory level of accuracy in the fitted data, at all of the selected spatial locations. Quantitative data on these fits are presented in Table 4-3 to Table 4-9.

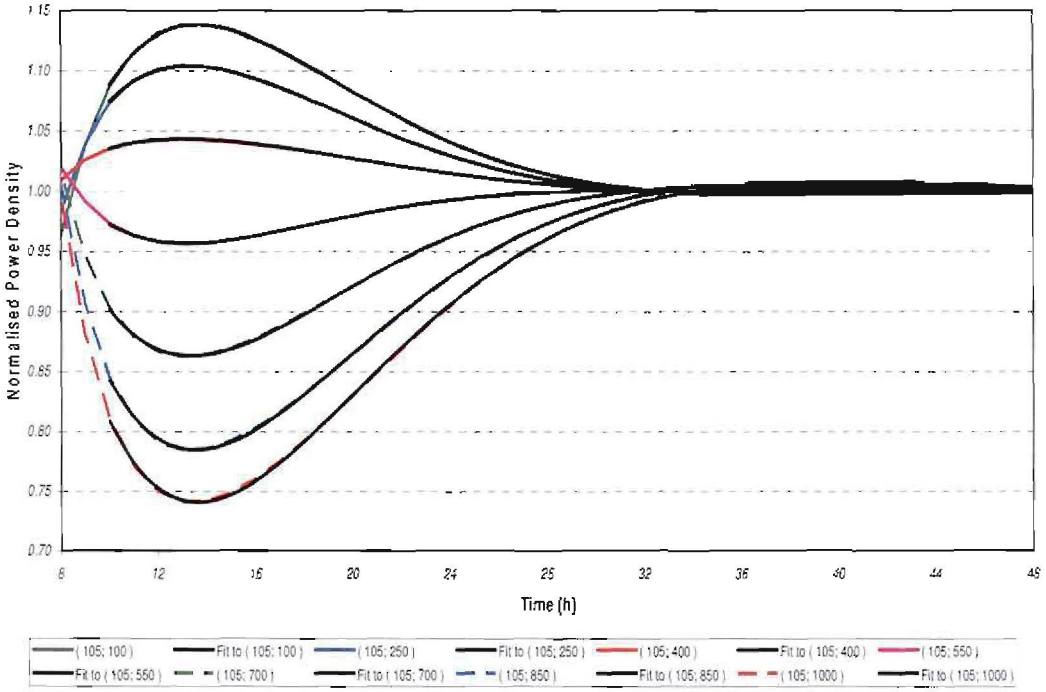

Figure 4-17: Case 1 normalized axial power density variation with time at r = 105 cm, including the overlaid least-squares fits.

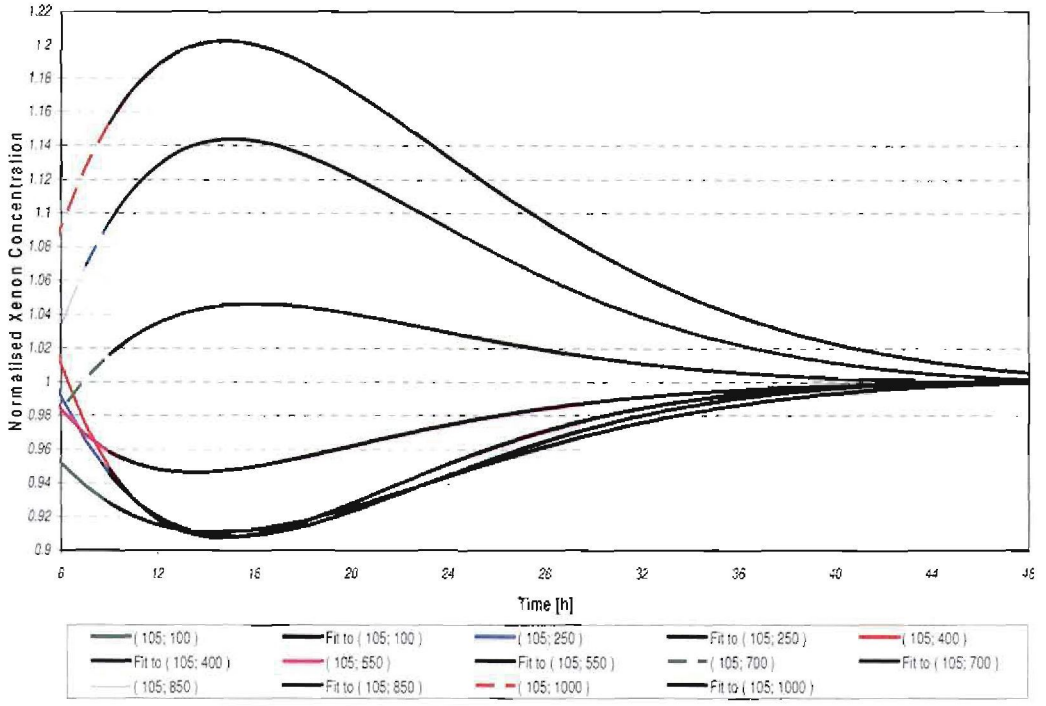

Figure 4-18: Case 4 normalized axial xenon concentration variation with time at r = 105 cm, including the overlaid least-squares fits.

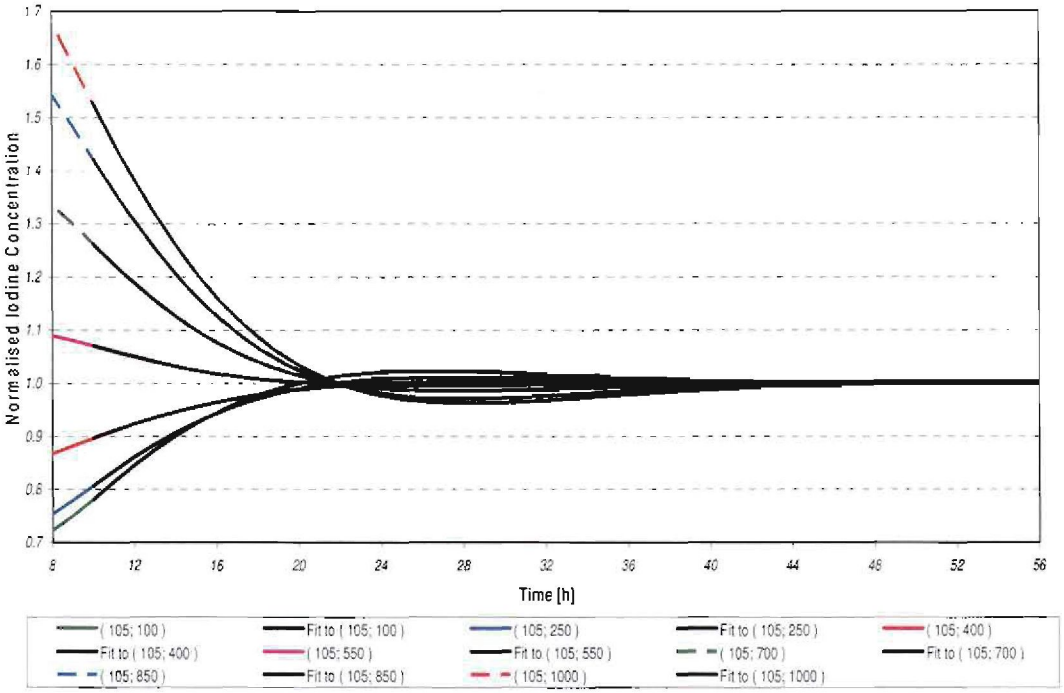

Figure 4-19: Case 1 normalized axial iodine concentration variation with time at r = 105 cm, including the overlaid Least-squares fits.

Table 4-3 to Table 4-7 present the case 1 data for the damping constant b, the least-squares fit constant C (both from Eq. (4.1)), the damping ratio ξ (from Eq. (4.2)), the damping period T_D (form Eq. (2.9) and the fit quality (or the standard error expressed as a fraction), for seven axial locations at two radial cuts (r = 105 cm and 180 cm).

The main parameter of interest here is the power density values, since the variations in local power density relate directly to the variations in the fuel temperatures. The other variables (fast and thermal flux, iodine and xenon) are included here for completeness sake, but these data sets are not used in the determination of the case-average power density stability data.

A few general remarks can be made:

i. The least-squares fit constant b varies between 0.12 and 0.18 for the various spatial locations, but the damping ratio ξ shows a smaller range, between 0.50 and 0.53. The value of $\xi \sim 0.5$ represents quite a large degree of damping inherent in the PBMR design of almost 50% of the critical damping transition point (see Figure 2-5 in Chapter 2 for a comparison of the damping effects for various ξ values).

ii. In general, the b and ξ values should be space-independent if a pure exponential-sinusoidal single mode axial oscillation exists. This expectation is confirmed from the data in the tables, which show no significant variations in the b or ξ values between the different axial locations.

The exceptions to this observation are the ξ values at z = 400 cm and z = 550 cm, i.e. close to the axial oscillation node, which are slightly lower when compared to the other locations. The relevance of this "distortion" of the oscillatory fit data near the nodal location is discussed in more detail in Section 4.2.5.

iii. The damped period T_D varies between 48 and 53 h at most of the locations, except at z ~ 400 - 550 cm, i.e. close to the axial oscillation node. These two locations exhibit smaller damped periods, between 39 and 43 h. The quality of the fits at the nodal points is also lower, as indicated by the larger fitting errors here.

iv. The variances in b and ξ values are also to large extent independent of the chosen variable, although the xenon and iodine data show a slightly larger spread, when compared to the power and flux values. This is especially true for the location near to the oscillation nodes for these two variables.

Table 4-3: Case 1 fast flux least-squares fit and oscillation damping data

Fit location	Damping constant b	Constant C	Damping ratio ξ	Damped Period T_D	Fit Quality
(105; 100)	0.14	0.13	0.53	47	8.85E-03
(105; 250)	0.14	0.13	0.53	48	6.10E-03
(105; 400)	*0.12*	*0.12*	*0.51*	*54*	*2.87E-03*
(105; 550)	*0.16*	*0.16*	*0.50*	*39*	*1.30E-02*
(105; 700)	0.14	0.13	0.52	47	7.13E-03
(105; 850)	0.13	0.12	0.52	50	6.77E-03
(105; 1000)	0.13	0.12	0.53	53	9.54E-03
(180; 100)	0.14	0.13	0.53	47	8.54E-03
(180; 250)	0.14	0.13	0.53	48	6.27E-03
(180; 400)	*0.12*	*0.12*	*0.52*	*54*	*2.74E-03*
(180; 550)	*0.16*	*0.16*	*0.50*	*39*	*1.31E-02*
(180; 700)	0.14	0.13	0.52	47	7.11E-03
(180; 850)	0.13	0.12	0.52	51	6.81E-03
(180; 1000)	0.13	0.12	0.53	53	9.54E-03

Table 4-4: Case 1 thermal flux least-squares fit and oscillation damping data

Fit location	Damping constant b	Constant C	Damping ratio ξ	Damped Period T_D	Fit Quality
(105; 100)	0.14	0.13	0.53	47	1.01E-02
(105; 250)	0.14	0.13	0.54	48	7.37E-03
(105; 400)	*0.12*	*0.12*	*0.52*	*53*	*2.02E-03*
(105; 550)	*0.16*	*0.17*	*0.48*	*38*	*1.33E-02*
(105; 700)	0.14	0.13	0.52	47	6.65E-03
(105; 850)	0.13	0.12	0.52	50	6.52E-03
(105; 1000)	0.13	0.12	0.53	53	9.51E-03
(180; 100)	0.14	0.13	0.53	47	9.53E-03
(180; 250)	0.14	0.13	0.54	48	7.58E-03

(180; 400)	*0.12*	*0.12*	*0.52*	*53*	*2.04E-03*
(180; 550)	*0.16*	*0.17*	*0.49*	*38*	*1.33E-02*
(180; 700)	0.14	0.13	0.52	47	6.62E-03
(180; 850)	0.13	0.12	0.52	51	6.58E-03
(180; 1000)	0.13	0.12	0.53	53	9.54E-03

Table 4-5: Case 1 power density least-squares fit and oscillation damping data

Fit location	Damping constant *b*	Constant *C*	Damping ratio ξ	Damped Period T_D	Fit Quality
(105; 100)	0.14	0.13	0.53	47	9.82E-03
(105; 250)	0.14	0.13	0.53	48	6.80E-03
(105; 400)	*0.12*	*0.12*	*0.52*	*54*	*2.39E-03*
(105; 550)	*0.16*	*0.16*	*0.50*	*40*	*1.11E-02*
(105; 700)	0.14	0.13	0.52	47	6.55E-03
(105; 850)	0.13	0.12	0.52	50	6.25E-03
(105; 1000)	0.13	-0.12	0.53	53	9.07E-03
(180; 100)	0.14	0.13	0.53	47	9.16E-03
(180; 250)	0.14	0.13	0.54	48	7.17E-03
(180; 400)	*0.12*	*0.12*	*0.52*	*54*	*2.24E-03*
(180; 550)	*0.16*	*0.16*	*0.50*	*39*	*1.13E-02*
(180; 700)	0.14	0.13	0.52	47	6.52E-03
(180; 850)	0.13	0.12	0.52	51	6.63E-03
(180; 1000)	0.13	-0.12	0.53	53	9.16E-03

Table 4-6: Case 1 xenon concentration least-squares fit and oscillation damping data

Fit location	Damping constant *b*	Constant *C*	Damping ratio ξ	Damped Period T_D	Fit Quality
(105; 100)	0.16	0.16	0.51	40	9.70E-02
(105; 250)	0.15	0.14	0.54	44	4.73E-02
(105; 400)	*0.15*	*0.11*	*0.62*	*55*	*7.01E-03*
(105; 550)	*0.17*	*0.15*	*0.58*	*43*	*1.30E-03*
(105; 700)	0.15	0.14	0.55	46	9.97E-04
(105; 850)	0.13	0.13	0.52	50	1.48E-02
(105; 1000)	0.12	0.11	0.53	56	3.37E-02
(180; 100)	0.14	0.15	0.49	43	2.29E-02
(180; 250)	0.17	0.14	0.61	45	5.44E-02
(180; 400)	*0.18*	*0.10*	*0.76*	*61*	*8.90E-03*
(180; 550)	*0.17*	*0.15*	*0.57*	*43*	*6.00E-04*
(180; 700)	0.14	0.13	0.54	47	2.57E-03
(180; 850)	0.13	0.12	0.53	52	2.09E-02
(180; 1000)	0.12	0.11	0.55	59	3.49E-02

Table 4-7: Case 1 iodine concentration least-squares fit and oscillation damping data

Fit location	Damping constant *b*	Constant *C*	Damping ratio ξ	Damped Period T_D	Fit Quality
(105; 100)	0.13	0.13	0.48	47	1.37E-03
(105; 250)	0.14	0.13	0.53	48	5.14E-04
(105; 400)	*0.14*	*0.12*	*0.60*	*54*	*1.29E-03*
(105; 550)	*0.18*	*0.16*	*0.56*	*40*	*7.36E-03*
(105; 700)	0.15	0.13	0.55	47	2.36E-03
(105; 850)	0.13	0.12	0.53	50	4.99E-04
(105; 1000)	0.13	0.12	0.53	53	6.58E-04
(180; 100)	0.13	0.13	0.48	47	8.43E-04
(180; 250)	0.15	0.13	0.56	48	2.04E-03
(180; 400)	*0.17*	*0.11*	*0.72*	*59*	*4.49E-03*
(180; 550)	*0.18*	*0.16*	*0.56*	*40*	*7.33E-03*
(180; 700)	0.15	0.13	0.55	47	2.35E-03
(180; 850)	0.13	0.12	0.53	51	7.48E-04
(180; 1000)	0.13	0.12	0.53	53	6.87E-04

Since Table 4-3 to Table 4-7 can be created for all four cases (but not enough space can be allocated here for their full representation), Table 4-8 and Table 4-9 present the summarized spatial damping ratio data for cases 1 to 4 for the five variables investigated in this study. It has also been discussed that there is no significant dependence of the b or ξ values on the spatial location of the damping fit, and that the power density core spatial average values for the four cases are therefore the main outcome of this inherent oscillation stability investigation. The average values have been calculated over all the spatial positions, except the nodal points z = 400 cm and z = 550 cm due to the distortion of the fitted data close to the oscillation node position. (The data points at these locations are shown in italics in the tables).

The overall power density average damping ratios are 0.53, 0.55, 0.60 and 0.73, respectively (Table 4-9). There is a clear trend towards an increased inherent damping ratio as the power levels are decreased, with the 20% power case (case 4) showing the strongest damping characteristics. This trend is a qualitative confirmation of the observations made in the literature, as summarised in Section 2.2. The current PBMR equilibrium core operating at the nominal power level of 400 MW can therefore be characterised by a single set of inherent power density stability parameters:

- Damping ratio ξ =0.53
- Damping constant b = 0.14
- Damped period T_D = 49 h

(A similar spatial averaging approach was followed to obtain the indicated values for the damping constant and period from Table 4-5).

Table 4-8: Comparison between the power density damping ratio ξ for cases 1-4

Variable	Spatial Location	case 1	case 2	case 3	case 4
Fast flux	(105; 100)	0.53	0.54	0.58	0.70
	(105; 250)	0.53	0.56	0.60	0.72
	(105; 400)	*0.51*	*0.55*	*0.63*	*0.74*
	(105; 550)	*0.50*	*0.48*	*0.28*	*0.79*
	(105; 700)	0.52	0.55	0.60	0.71
	(105; 850)	0.52	0.55	0.61	0.74
	(105; 1000)	0.53	0.56	0.62	0.75
	(180; 100)	0.53	0.54	0.58	0.70
	(180; 250)	0.53	0.56	0.60	0.72
	(180; 400)	*0.52*	*0.56*	*0.63*	*0.74*
	(180; 550)	*0.50*	*0.48*	*0.27*	*0.78*
	(180; 700)	0.52	0.55	0.60	0.71
	(180; 850)	0.52	0.55	0.61	0.74
	(180; 1000)	0.53	0.56	0.62	0.75
Average		**0.53**	**0.55**	**0.60**	**0.72**
Thermal flux	(105; 100)	0.53	0.54	0.58	0.70
	(105; 250)	0.54	0.56	0.61	0.72
	(105; 400)	*0.52*	*0.56*	*0.63*	*0.74*
	(105; 550)	*0.48*	*0.45*	*0.13*	*0.79*
	(105; 700)	0.52	0.55	0.60	0.70
	(105; 850)	0.52	0.55	0.61	0.74
	(105; 1000)	0.53	0.56	0.62	0.75
	(180; 100)	0.53	0.54	0.58	0.70
	(180; 250)	0.54	0.56	0.61	0.72
	(180; 400)	*0.52*	*0.56*	*0.63*	*0.74*
	(180; 550)	*0.49*	*0.46*	*0.54*	*0.79*
	(180; 700)	0.52	0.55	0.60	0.71
	(180; 850)	0.52	0.55	0.61	0.74
	(180; 1000)	0.53	0.56	0.62	0.75
Average		**0.53**	**0.55**	**0.60**	**0.72**
Power density	(105; 100)	0.53	0.54	0.58	0.71
	(105; 250)	0.53	0.56	0.60	0.72
	(105; 400)	*0.52*	*0.56*	*0.63*	*0.74*
	(105; 550)	*0.50*	*0.49*	*0.31*	*0.80*
	(105; 700)	0.52	0.55	0.60	0.71
	(105; 850)	0.52	0.55	0.61	0.74
	(105; 1000)	0.53	0.56	0.62	0.75
	(180; 100)	0.53	0.54	0.58	0.71
	(180; 250)	0.54	0.56	0.61	0.72
	(180; 400)	*0.52*	*0.56*	*0.63*	*0.74*

	(180; 550)	*0.50*	*0.49*	*0.30*	*0.79*
	(180; 700)	0.52	0.55	0.60	0.71
	(180; 850)	0.52	0.55	0.61	0.74
	(180; 1000)	0.53	0.56	0.62	0.75
Average		**0.53**	**0.55**	**0.60**	**0.73**

Table 4-9: Comparison between the damping ratio ξ for cases 1-4: iodine and xenon concentration values

Variable	Spatial Location	case 1	case 2	case 3	case 4
iodine	(105; 100)	0.48	0.48	0.50	0.63
	(105; 250)	0.53	0.53	0.55	0.66
	(105; 400)	*0.60*	*0.62*	*0.64*	*0.71*
	(105; 550)	*0.56*	*0.50*	*0.29*	*0.79*
	(105; 700)	0.55	0.56	0.60	0.69
	(105; 850)	0.53	0.55	0.60	0.73
	(105; 1000)	0.53	0.55	0.60	0.73
	(180; 100)	0.48	0.48	0.50	0.63
	(180; 250)	0.56	0.56	0.58	0.66
	(180; 400)	*0.72*	*0.72*	*0.71*	*0.74*
	(180; 550)	*0.56*	*0.48*	*0.60*	*0.87*
	(180; 700)	0.55	0.56	0.60	0.68
	(180; 850)	0.53	0.55	0.60	0.73
	(180; 1000)	0.53	0.55	0.61	0.74
Average		**0.53**	**0.54**	**0.58**	**0.69**
xenon	(105; 100)	0.51	0.50	0.50	0.64
	(105; 250)	0.54	0.57	0.61	0.66
	(105; 400)	*0.62*	*0.65*	*0.71*	*0.74*
	(105; 550)	*0.58*	*0.56*	*0.45*	*0.84*
	(105; 700)	0.55	0.56	0.60	0.70
	(105; 850)	0.52	0.54	0.59	0.72
	(105; 1000)	0.53	0.55	0.60	0.73
	(180; 100)	0.49	0.48	0.54	0.68
	(180; 250)	0.61	0.62	0.62	0.68
	(180; 400)	*0.76*	*0.80*	*0.79*	*0.76*
	(180; 550)	*0.57*	*0.54*	*0.94*	*0.91*
	(180; 700)	0.54	0.55	0.59	0.69
	(180; 850)	0.53	0.55	0.59	0.72
	(180; 1000)	**0.55**	**0.57**	**0.62**	**0.74**
Average		**0.54**	**0.55**	**0.58**	**0.70**

The set of inherent xenon stability parameters shown in Table 4-9 will be compared in Chapters 5 and 6 with the load-follow cases stability data. It is however clear from the quantitative (as well as the graphical) data presented in this chapter that the PBMR design exhibits quite a strong degree of inherent axial oscillation damping, ranging between ~ 0.5-0.7 (i.e. between 50% and 70% of the critical damping point, where no oscillations would occur)

A fourth very useful stability parameter can be derived using the data in Table 4-9. The variation of the damping ratio ξ with the steady-state power level is presented in Figure 4-20. A polynomial fit trend line is also shown in relation to the source data points. The dependency of the damping ratio ξ on the steady-state power level P is given by the third order polynomial fit expression

$$\xi = -(5.0\text{x}10^{-09})P^3 + (5.36\text{x}10^{-06})P^2 - (0.0022)P + 0.8679 \qquad (4.3)$$

with an R^2 value of 0.9999.

This implies that an increase of 100 MW in the reactor steady-state power from 300 MW to 400 MW would result in a decrease of the power density damping ratio ξ from 0.56 to 0.53, or 5%. Due to the non-linear dependency of stability on the power level, the decrease in stability is more severe at lower power levels. For example, an increase in power from 100 MW to 200 MW would result in decrease in stability from 0.70 to 0.60, or 14%.

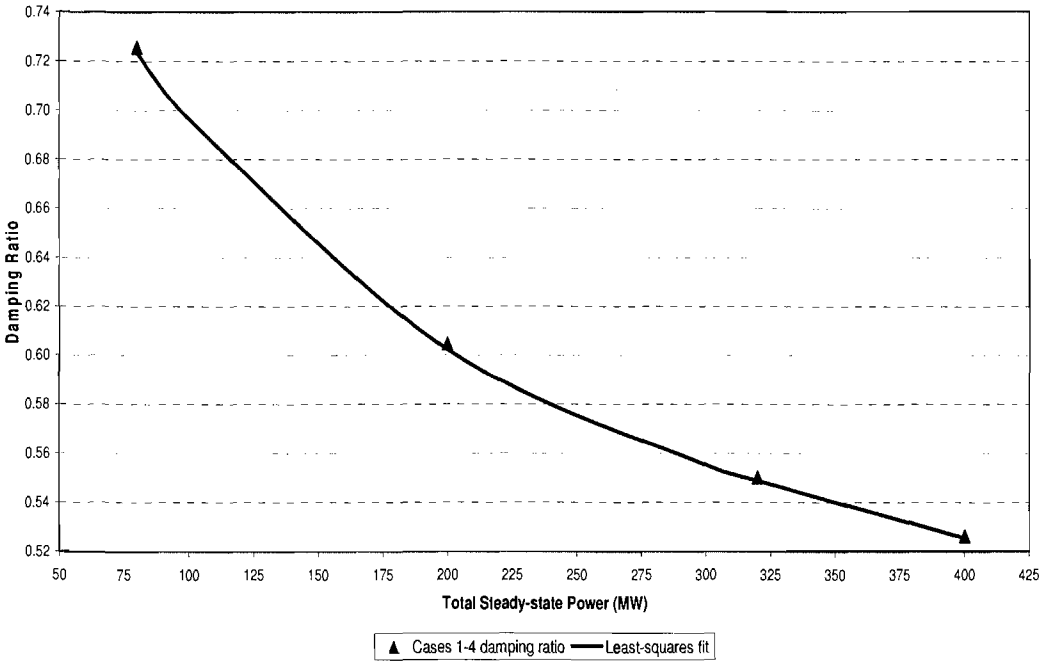

Figure 4-20: Variation in the inherent power density damping ratio ξ with steady-state power level.

The derivative of the damping ratio with the power level can also be determined from Eq (4.3) as

$$d\xi / dP = -(1.50\text{x}10^{-08})P^2 + (1.072\text{x}10^{-05})P - 0.0022 \qquad (4.4)$$

At the nominal power level of 400 MW, Eq. (4.4) results in a $d\xi / dP$ value of -3.12E-04 MW^{-1} for the current PBMR equilibrium core design. The value of the $d\xi / dP$ coefficient determined here for the inherent power density damping stability will be compared with the coefficients developed for the power load-follow transients in Sections 5.3 and 6.2, where a similar decrease in stability with an increase in the final power level is expected.

4.2.5 Variation of the damping ratio close to the axial nodal point

Figure 4-21 shows an interesting trend if the variation in the damping ratio ξ with the axial core height z is expressed in visual format. In this example, only the values for case 1 at r = 105 cm are used, and the damping ratio behaviour for all 5 variables are shown. It is found that a good correlation exists between the axial location of the oscillation node maxima at z ~ 250 cm and minima at z ~ 850 cm (see Figure 4-13), and the axial location where the smallest variation in damping ratio exists (compare the axial locations indicated with circles in Figure 4-21). This implies that the optimal locations for the determination of the axial damping ratio parameter correspond to the oscillation mode maxima and minima, i.e. in the top and bottom parts of the core.

By the same argument, locations near the axial centre of the core should be excluded from the determination of the core-averaged damping ratio, since the data are distorted due to the axial oscillation nodes located here. The distortion in the data around the nodal points could be caused by small-amplitude higher axial mode overlays, which become only visible where the first axial mode amplitude is close to zero.

Note that the location of the control rods also plays a role in this trend: since the axial power shape is forced progressively downwards by the deeper control rods from case 1 to case 4, the spread in the damping ratio values also becomes larger from case 1 to case 2 at the same location (i.e. when Figure 4-21 and Figure 4-22 are compared), as the oscillation node is also shifted downwards by ~ 120 cm (see Figure 4-11 and Figure 4-12). When Figure 4-21 is compared with Figure 4-23, this trend is confirmed by the fact that the spread in damping ratio values for case 4 at z ~ 250 cm is actually larger than the spread at the next deeper location (z ~ 400 cm). The spread in the damping ratio values in the bottom areas of the core remain unaffected by the change in the control rod locations between the four cases.

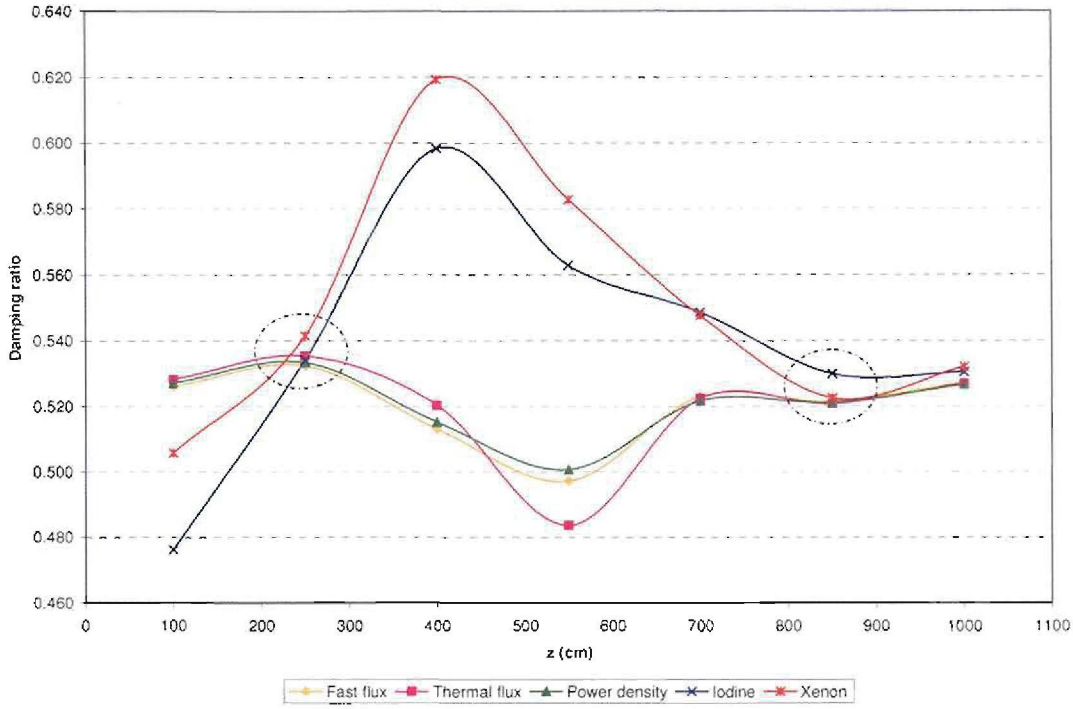

Figure 4-21: Case 1 variation in the damping ratio ξ with axial height z at radius r = 105 cm, for fast and thermal flux, power density, iodine and xenon.

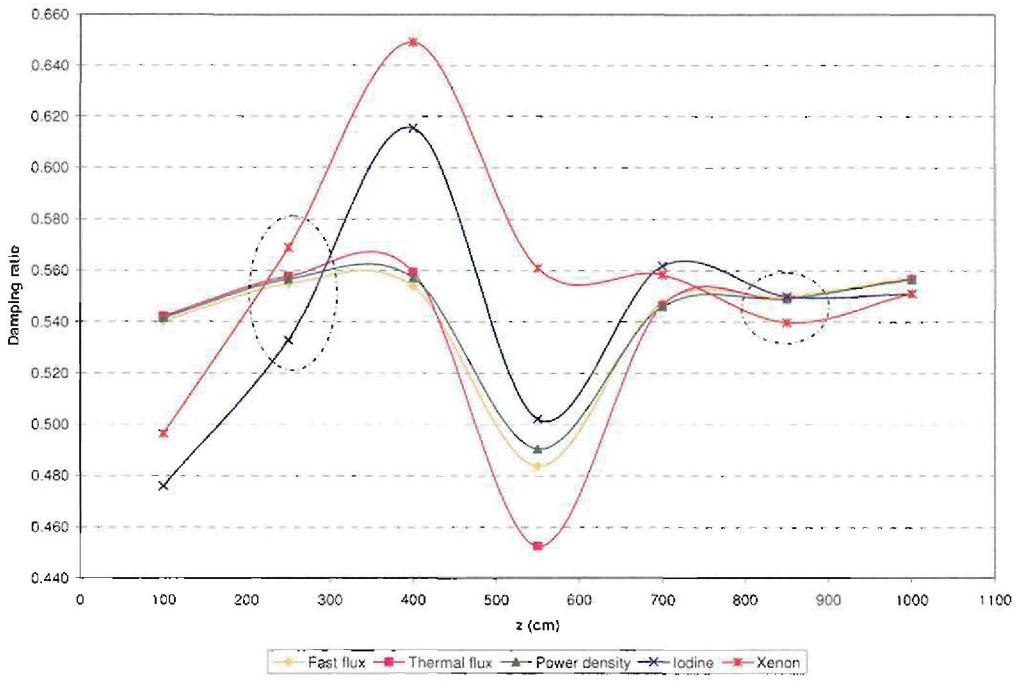

Figure 4-22: Case 2 variation in the damping ratio ξ with axial height z at radius r = 105 cm, for fast and thermal flux, power density, iodine and xenon.

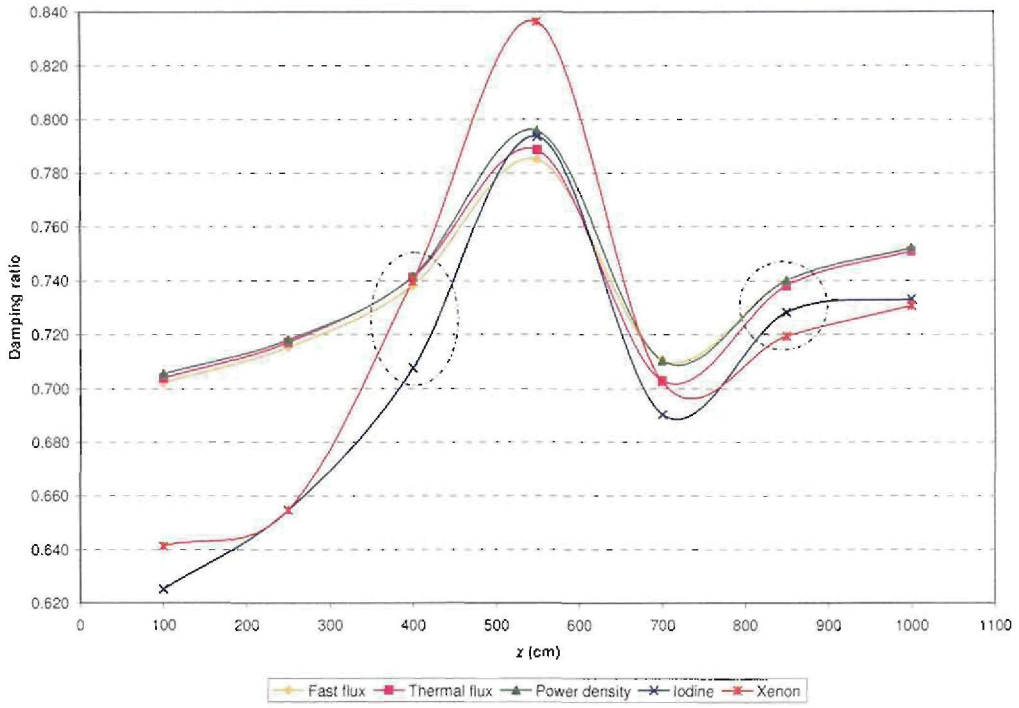

Figure 4-23: Case 4 variation in the damping ratio ξ with axial height z at radius r = 105 cm, for fast and thermal flux, power density, iodine and xenon.

4.3 SUMMARY

The first quantitative results of the PBMR xenon stability study were presented in Chapter 4. The focus was on the determination of the inherent xenon stability, and four transient cases were defined that involved the insertion and removal of the full control rod bank at 20%, 50%, 80% and 100% power. The resulting xenon-induced axial power oscillations (as well as the flux, xenon and iodine variations) were analysed in detail in Sections 4.2.1 and 4.2.2, and data was presented on the absolute and normalised axial oscillations, as well as representative axial profiles of these parameters.

It was shown in Section 4.2.3 that the axial oscillations obtained by the insertion of the control rod bank did not lead to any significant oscillations in the radial dimension. This result confirmed the first-principle expectation that no radial oscillation components should exist for these axial xenon oscillation transients in the thin PBMR annular core.

In Section 4.2.4 the least-squares fit formulation, as described in Section 2.3, was utilised to obtain quantitative oscillation damping data from the four transients that were defined in this chapter. Not only was it found that the xenon stability of the PBMR decreases with an increase in operating power levels, but also that the current PBMR core design exhibits quite strongly damped axial xenon and power oscillations. An average damping ratio value of 0.53 was obtained for the four cases. (Compare Figure 2-4 and Figure 2-5 for a general visual interpretation of the degree of damping that this value implies).

In order to compare the degree of damping obtained in this chapter with the load-follow transient data that are presented in Sections 5.3 and 6.2, a relationship between the operating power level and the damping ration was determined. It was found that the dependency of the damping ratio ξ on the steady-state power level P is given by the third order polynomial fit expression

$$\xi = -(5.0\text{x}10^{-09})P^3 + (5.36\text{x}10^{-06})P^2 - (0.0022)P + 0.8679 \qquad (4.3)$$

This implies that an increase of 100 MW in the reactor steady-state power from 300 MW to 400 MW would result in a decrease of the power density damping ratio ξ from 0.56 to 0.53, or 5%. As a second indicator of the variance of xenon stability with power, the derivative of Eq. (4.3) was evaluated at the nominal power level of 400 MW, and a value of $d\xi/dP$ = -3.12E-04 MW^{-1} was obtained. This result will be compared with the values obtained for the power load-follow transients in Sections 5.3 and 6.2, where a similar decrease in stability with an increase in the final power level is expected.

CHAPTER 5

5. PBMR AXIAL XENON STABILITY DURING A 100%-40%-100% POWER LOAD-FOLLOW TRANSIENT

The inherent xenon stability of the PBMR was investigated in Chapter 4 by defining four transients that involved the artificial insertion and removal of the control rod banks to excite axial xenon-induced power oscillations. However, these artificial control rod movements will not occur for the operating PBMR core, but frequent operational power changes (also called load-follows) will be required. These load-follows necessitate the movement of the control rods to keep the core critical due to the global xenon build-up (as explained in Section 5.1), which will again lead to xenon-induced axial power oscillations. The current PBMR system specification requires that power load-follow manoeuvres be performed within the range 160 MW (40%) to 400 MW (100%). The 100%-40%-100% load-follow event is therefore taken as the reference load-follow transient for this study.

Most of the load-follow transients reported in Chapters 5 and 6 are analysed with and without control rod movements, to quantify and compare the effect of the moving control rods on the inherent axial power and xenon oscillation damping. Apart from the focus on the stability quantification of these oscillations, a practical assessment of the effects of xenon oscillations on the operating PBMR, in terms of the variations in the fuel temperatures and power density amplitudes is also performed.

Apart from the 100%-40%-100% load-follow transient reported in detail in this chapter, the summarised results of two power load-follow sensitivity studies have also been included in Chapter 6. The first transient set consists of four cases where the 50% power phase duration of a 100%-50%-100% load-follow transient has been specified over 6 h,12 h,18 h, and 24 h, while the second set of four hypothetical cases consists of open-ended higher power variations (100%-125%, 100%-150%, 100%-175% and 100%-200%). The sensitivity studies are included in this work to provide quantitative data for the xenon stability parameters for a large variety of possible load-follow transients.

The first two load-follow transients defined for this study follow the same basic pattern:

- operation at full power for an extended period (at least several days for equilibrium to be reached), plus an additional hour at 100% power, explicitly shown in the simulation calculations.
- a reduction to 40% power for a period of 6 h,
- and then a ramp back to 100% power.

The two load-follow transients differ in the following:

- Case 5 has an active control rod control during the load-follow.
- Case 6 presents the same transient without any control rod movements, in order to compare the "free" oscillation properties of this load-follow with the more complex spatial effects of the control rod movements in case 5.

The 40% power phase for 6 h was selected because the global xenon maximum build-up peak is reached close to this time point (see Figure 5-1). Case 5 is the reference case for the load-follow transients, since the PBMR core design criteria currently includes the requirement to change the reactor power from 100% to 40% over a period of 6 minutes (the PBMR maximum load-follow rate is 40 MW/minute).

5.1 GLOBAL PARAMETER RESULTS

Both cases are modelled by changing the following boundary conditions in TINTE:

- The main inlet gas flow rate is decreased from 100% (192.7 kg/s) to 40% (77.1 kg/s) over 6 minutes, starting at t = 1 h.
- The reactor outlet pressure is decreased from 87.9 bar to 35.16 bar over 6 minutes, also starting at t = 1 h. (The CBCS mass flow and pressure are also reduced in the same way).
- A reactor total power ramp from 100% to 40% is also applied in the same period to match the total reactor power with the fluidic power decrease during the transient. In case 5 the global auto-reactivity controller is instructed to move the control rods to keep the reactor critical during the event. (For example, when the fuel temperature decreases due to lower fission power production, this will tend to increase k-eff, so that the control rods need to be inserted to offset the increase in global reactivity). The auto-controller uses a dead-bandwidth of 10 mNile, i.e. the control rod will only be moved when the change in k-eff is larger than ± 0.0001. In some cases a 50 mNile bandwidth was used to investigate the effect of less control rod movement during the transient.
- A t = 7 h, all of the above parameters are returned to their nominal (100%) values over 6 minutes again.
- The transient is calculated for a total of 72 h, without any further changes.

Figure 5-1 indicates the core-averaged xenon absorption (as a percentage of the total neutron absorption), as well as the control rods (CR) location for case 5. The global xenon absorption level [1] increases by 36% from the steady-state value (2.15%) to the peak value (2.92%) at t = 6.3 h. The average xenon absorption level returns to its steady-state level after approximately 65 h.

[1]The global Xenon concentration levels are, strictly speaking, directly proportional to the core-averaged Xenon absorption only if the fuel temperature, and therefore the neutron spectrum, remains unchanged. Since the fuel temperature variations are shown to be small in Section 5.2.2.1, the approximation made here is acceptable.

It can be seen from Figure 5-2 that the core-averaged xenon absorption level for case 6 is approximately 0.12% higher at t = 6 h (2.92% for case 5 vs. 3.04% for case 6). The spatial movement of the control rods therefore caused a slight decrease in the core-averaged xenon build-up levels. Note that the 100%-40%-100% load-follow transient requires the control rod banks to be fully withdrawn from the core in the period between t = 4 h and 8 h (Figure 5-1). The importance of this finding, and possible mitigation measures are discussed in detail in Appendix A.

Since case 6 does not make use of the global reactivity balance effect of the control rods, the core would soon go sub-critical, and the transient data would become meaningless. To allow inherent xenon stability studies to be performed without the spatial influence of the control rods on the axial power profiles, an "external reactivity" value is calculated by the TINTE code. This time-dependent parameter indicates the global positive or negative reactivity that would be needed to return the core reactivity state to a k-effective value of 1.0000. The dynamic effect of moving the control rod during the xenon build-up can clearly be seen from Figure 5-3, which shows the difference in the external reactivity needed to keep the core critical for both cases.

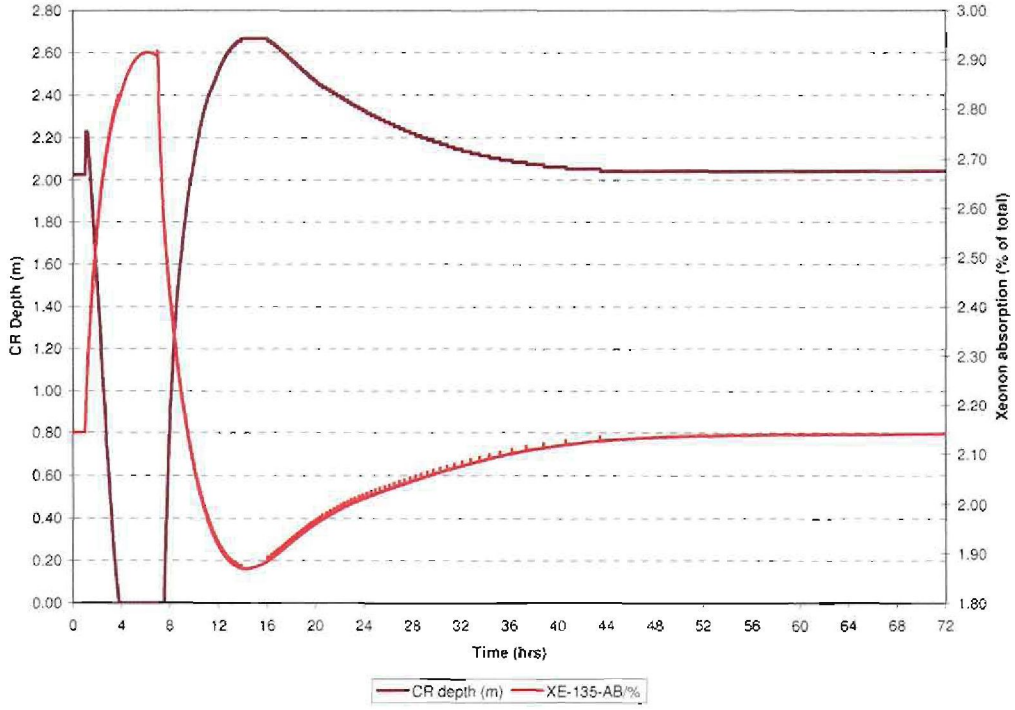

Figure 5-1: Case 5 core-averaged xenon absorption and control rod location

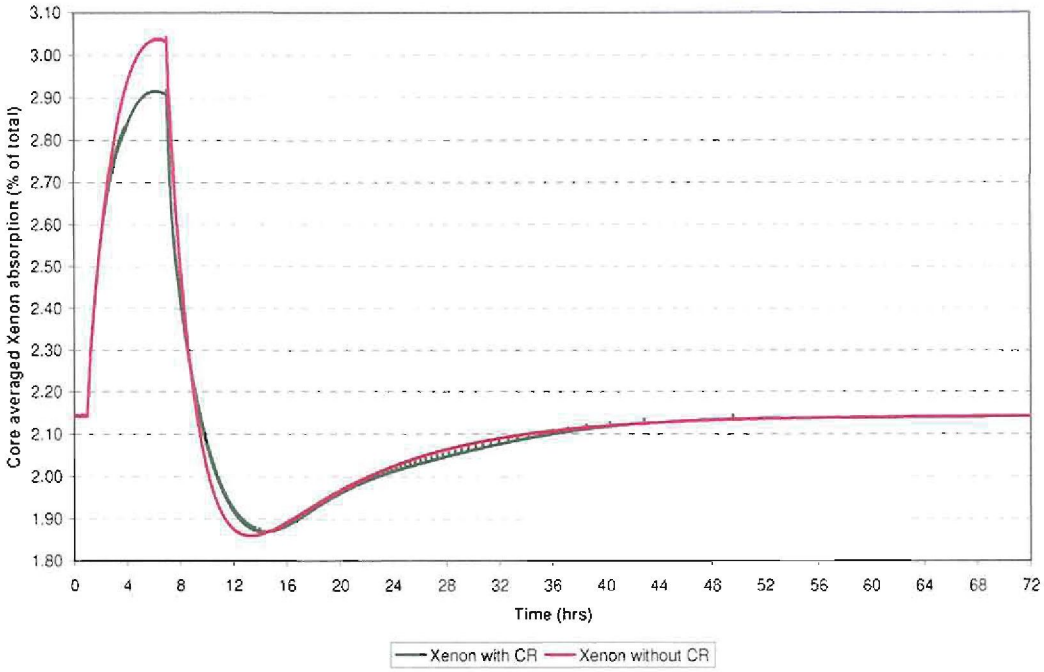

Figure 5-2: Case 5 and case 6 comparison - core-averaged xenon absorption levels

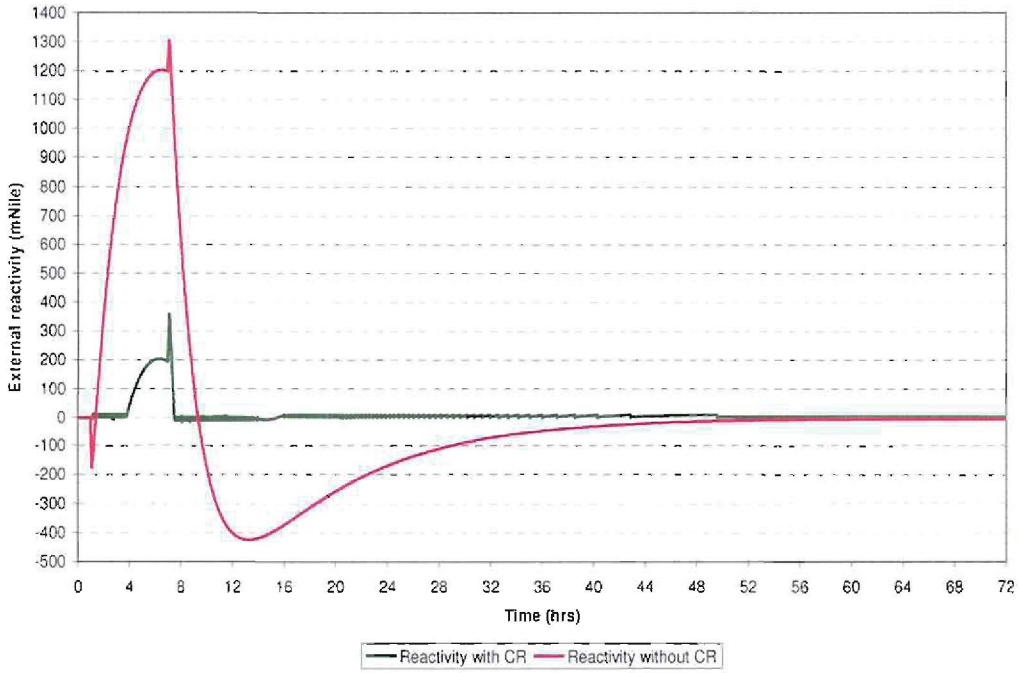

Figure 5-3: Case 5 and case 6 comparison- external reactivity levels

Table 5-1 indicates the reactivity differences between the two cases, which equates directly to the compensating reactivity effect of the control rod movements.

Table 5-1: External reactivity differences between case 5 and 6

Case #	Maximum reactivity (mNile) needed at xenon peak (t = 6 h)	Maximum reactivity (mNile) needed at ramp-up to 100% power (t = 7 h)
Case 5	203	357
Case 6	1203	1300

Figure 5-4 shows the maximum and average fuel temperatures for case 5. The sharp increases and decreases correspond to the power ramps from 40% to 100%, and back again. Since the reactor is operational, convective heat transfer is the dominant heat removal mechanism, and the fuel temperatures only change within a relatively narrow band. For example, the maximum fuel temperature increases from 1065°C to 1136°C (i.e. 70°C) in 45 minutes when the ramp back to 100% power occurs, while the average fuel temperature increases from 917°C to 961°C over the same period. It is clear therefore that load-follow scenarios represent no safety threats to fuel integrity or fission product releases.

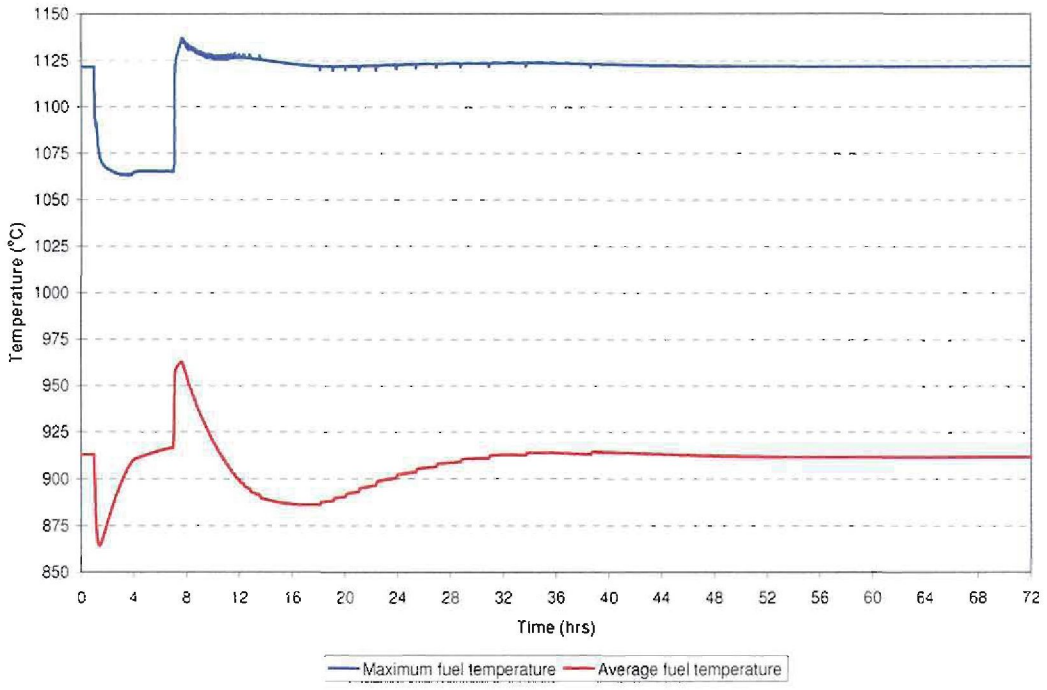

Figure 5-4: Case 5 average and maximum fuel temperature

Similar, but even smaller temperature variations are calculated for the average and maximum temperatures of the control rod channel, the core barrel (CB) and the reactor pressure vessel (RPV), as well as the side and central reflectors. It is interesting to note that the maximum and the average fuel temperature trends differ during the load-follow transitions. The maximum fuel temperature follows the power level changes very closely, since the adjustment of the neutronic heat source (via the increase/decrease in thermal and fast flux) happens relatively fast. However, during the 40% power phase the average fuel temperature over the whole core slowly returns to the 100% power phase average temperature, since the withdrawal of the control rods caused an upward shift in the axial power generation. Figure 5-5 shows this behaviour in more detail.

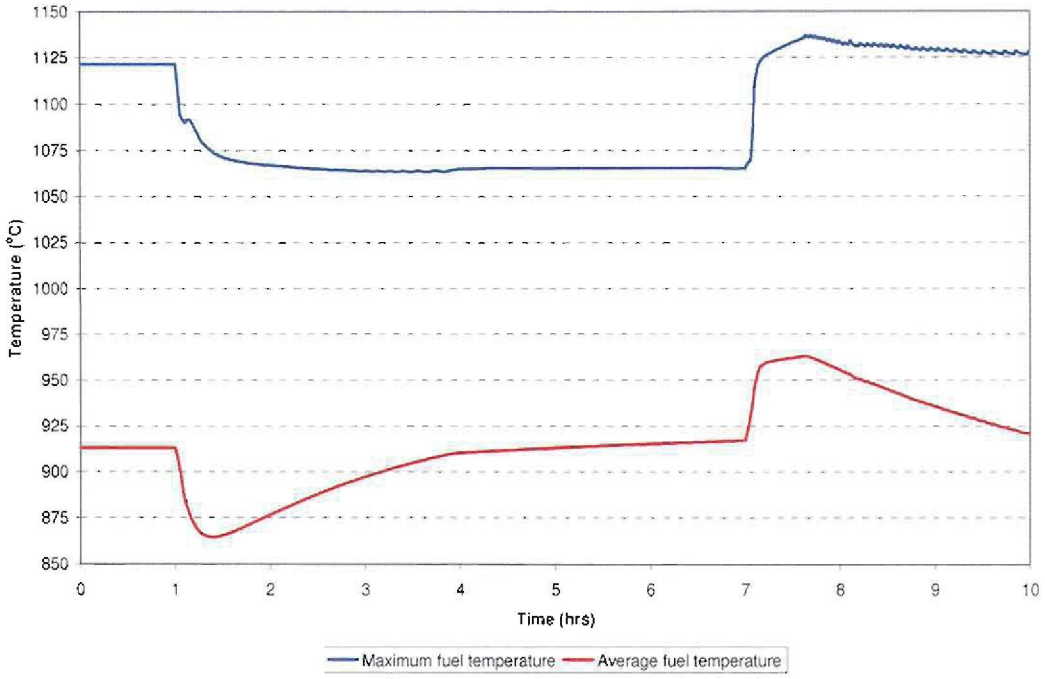

Figure 5-5: Case 5 average and maximum fuel temperature detail

5.2 SPATIAL XENON AND POWER DENSITY RESULTS

In this section, selected spatial output data for cases 5 and 6 are presented. This includes axial and radial cuts of the power density and xenon concentration, as well as the variations of these parameters over time at 9 selected core locations. Detail on the remaining secondary parameters of interest, i.e. the fast and thermal flux, local fuel temperatures and the iodine concentration are not included in this study, due to space limitations. A more detailed data set is presented in the PBMR report on this topic [25].

The full data set consists of spatial data at 60 core locations. The data are extracted along the axial height, from z = 100 cm to 1050 cm at 50 cm axial intervals, and at three radial locations: r = 105, 140 and 180 cm.

Since this full data set cannot be shown in graphical or tabular format in this study, only data for the radial location next to the side reflector at r = 180cm (and therefore closest to the control rods) are presented. The number of axial points is also reduced to 9 for graphical clarity, i.e. at 1 m intervals from z = 100 cm to z = 900 cm.

5.2.1 Xenon

Figure 5-6 and Figure 5-7 present the absolute and normalised spatial concentration levels of xenon over time for case 5 at 9 locations in the core, where it can seen that the normalised xenon variation reaches a minimum level at t = 36 h. The normalised xenon variations for case 6 are shown in Figure 5-8, and the large difference that exists between case 5 and 6 is apparent between t = 12 h and 60 h. The amplitude of the xenon variations is much smaller for case 6, but of more importance is the absence of opposite spatial xenon variations for case 6. This can be seen best at the location (180, 100) in the top of the core, where case 5 shows a large increase between t = 9 h and 16 h, while case 6 shows a decrease in the same period, together with the rest of the core locations.

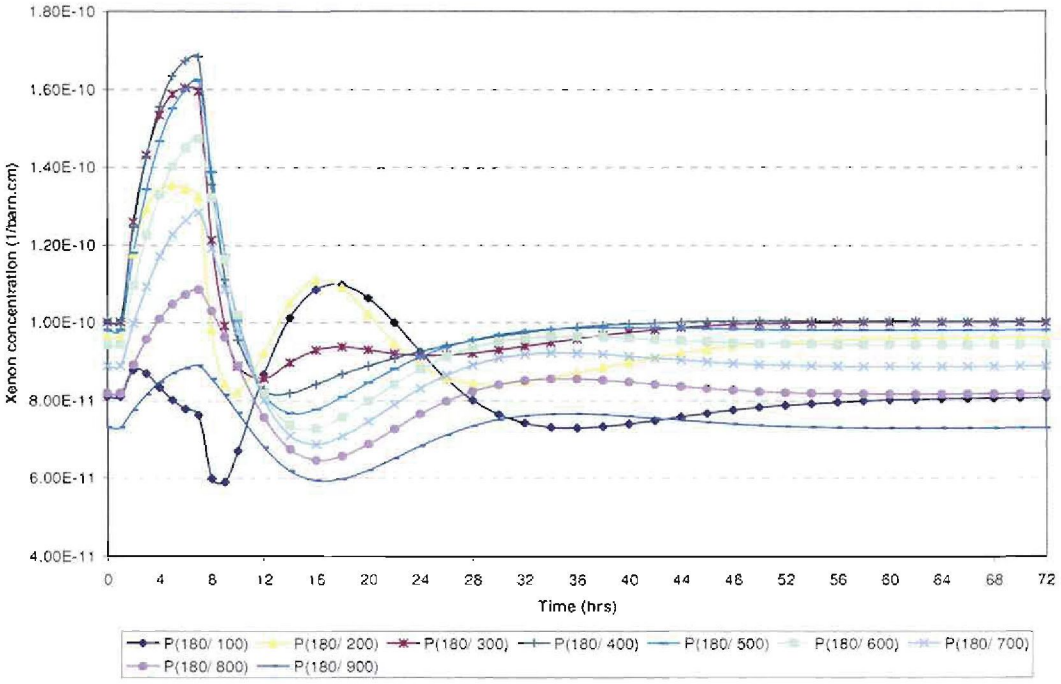

Figure 5-6: Case 5 spatial xenon concentration levels vs. time at 9 axial locations and r = 180 cm

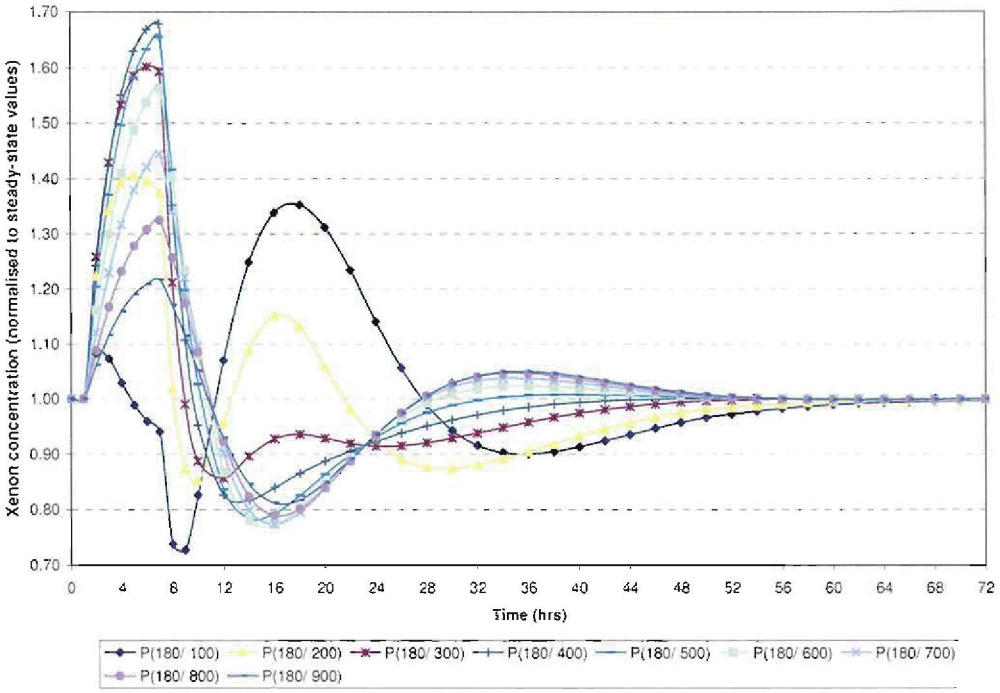

Figure 5-7: Case 5 normalised spatial xenon concentration levels vs. time at 9 axial locations, and r = 180 cm

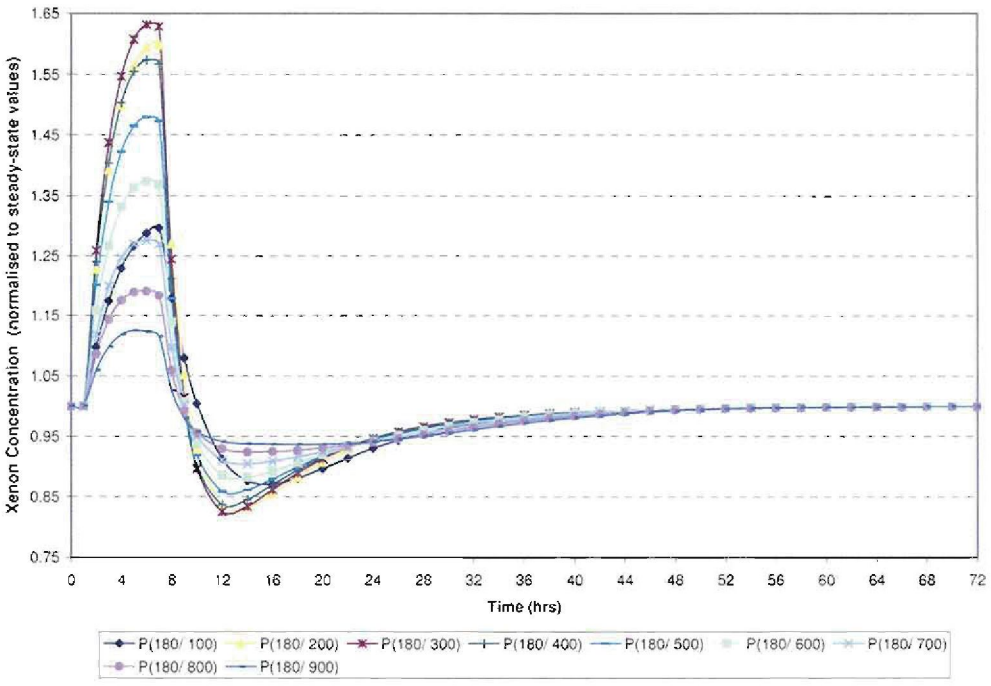

Figure 5-8: Case 6 normalised spatial xenon concentration levels vs. time at 9 axial locations, and r = 180 cm

The absolute and normalised axial xenon concentration profiles at r = 180 cm for case 5, presented in Figure 5-9 and Figure 5-10, seem to confirm the presence of two possible axial nodes at z ~ 300 cm and z ~ 500 cm. However, when the axial xenon profiles in the first 30 h of the transient are excluded from the data (Figure 5-11), the only axial oscillation node that remains is located at z ~ 420 cm. The "noise" that was introduced in the xenon spatial variations in the upper part of the core by the continued movements of the control rods caused a temporary oscillation node at z ~ 300 cm, which terminated as soon as the control rods moved less. Figure 5-1 shows that the control rods only move approximately 10 cm from 30 h onwards, which make the "free" oscillation axial node detail more visible from this point onwards. Note that the moving rods still cause minor deviations in the axial xenon profiles during the period t = 30 h to 54 h, as can be seen in Figure 5-11 by observing that the node position is shifted just for the four earlier curves, i.e. from 30 h to 36 h.

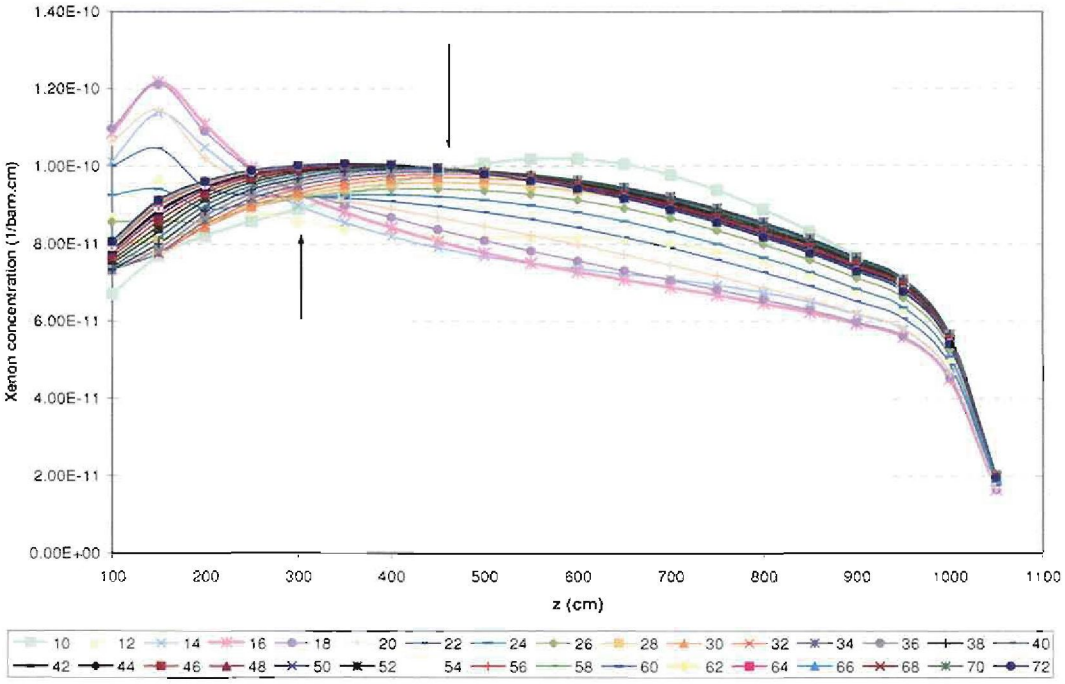

Figure 5-9: Case 5 axial xenon concentration profiles at r = 180 cm, for 32 time points from 10 h - 72 h

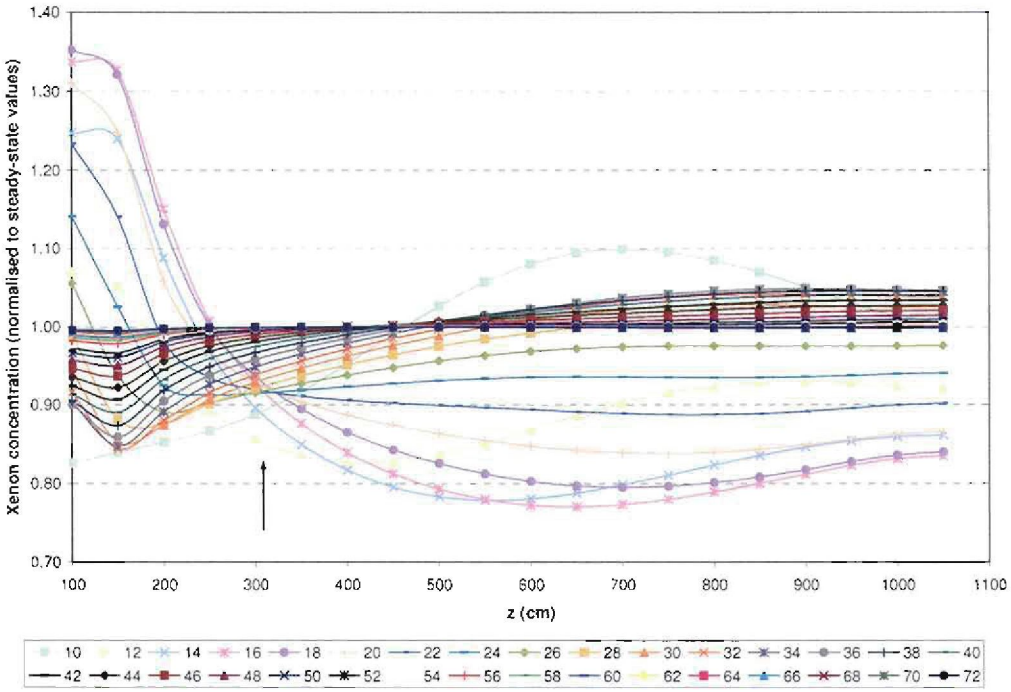

Figure 5-10: Case 5 normalised axial xenon concentration profiles at r = 180 cm, for 32 time points from 10 h - 72 h

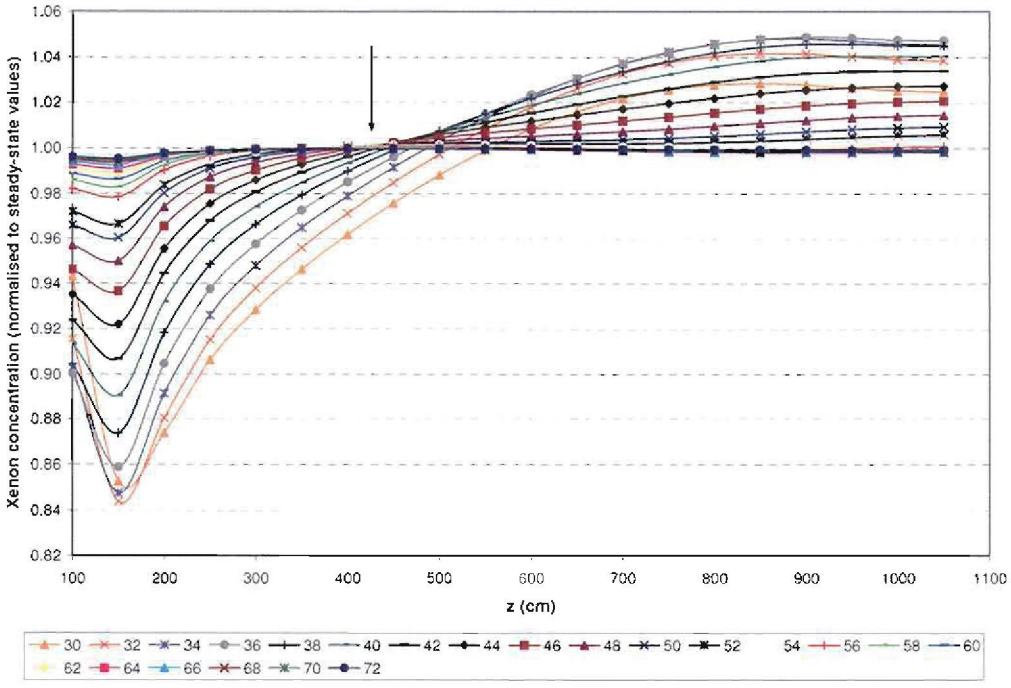

Figure 5-11: Case 5 normalised axial xenon concentration profiles at r = 180 cm, for 22 time points from 30 h - 72 h

In contrast to the clear first axial xenon oscillation mode that case 5 exhibits, case 6 shows very weak oscillatory behaviour in Figure 5-12. Only during the early stages of the transient between 10 h and 18 h, when the shift back to 100% flux levels still influences the xenon distribution, can an oscillatory node be distinguished at z ~ 510 cm. This difference in the nature of the xenon oscillation between the two cases is clear when Figure 5-11 (case 5) and Figure 5-13 (case 6) are compared for the "free" oscillation phase of case 5 (from t = 30 h - 72 h). These observations lead to the important conclusion that the movement of the control rods is the main driving mechanism for the decrease in the axial xenon oscillation stability during a typical load-follow transient. This decrease in damping stability is confirmed in the next section of this chapter, where the quantitative damping properties of case 5 and case 6 are determined.

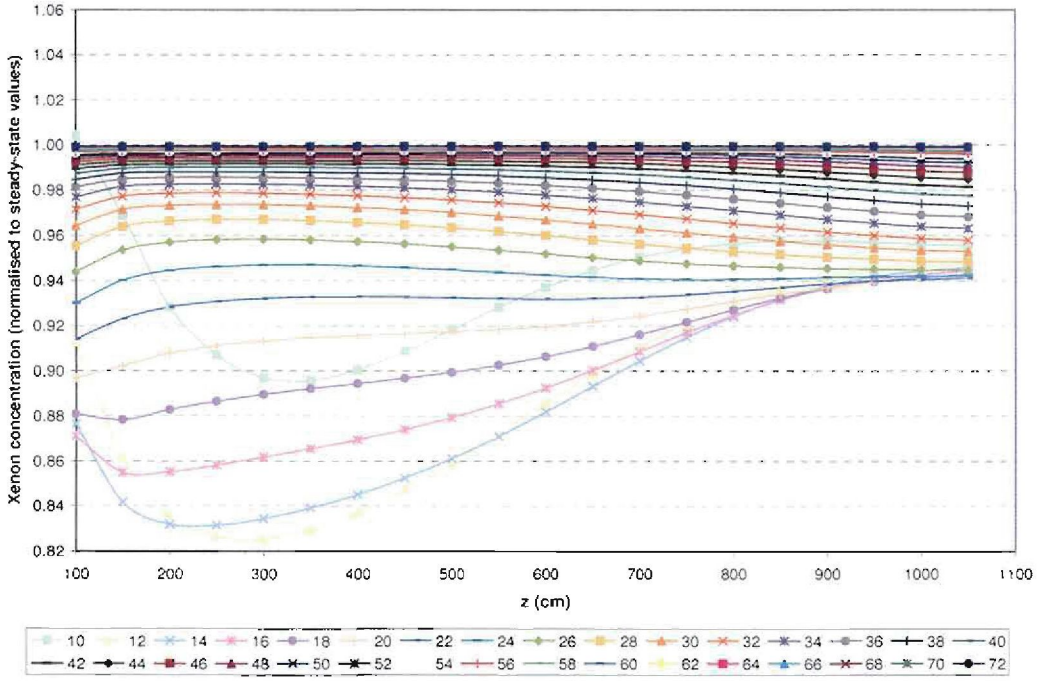

Figure 5-12: Case 6 normalised axial xenon concentration profiles at r = 180 cm, from 10 h -72 h

Figure 5-14 and Figure 5-15 show the radial xenon concentration differences on an axial cut at z = 800 cm for cases 5 and case 6, i.e. the change in the radial xenon concentration shape over time. Only very small variations occur in the radial xenon concentration differences in the earlier stages of case 5 and case 6, which confirms the conclusion made in Section 4.2.3 in regard to the inherent damping cases 1 to 4, where it was found that the axial xenon oscillations occurring during these transients do not excite a radial oscillation component as well.

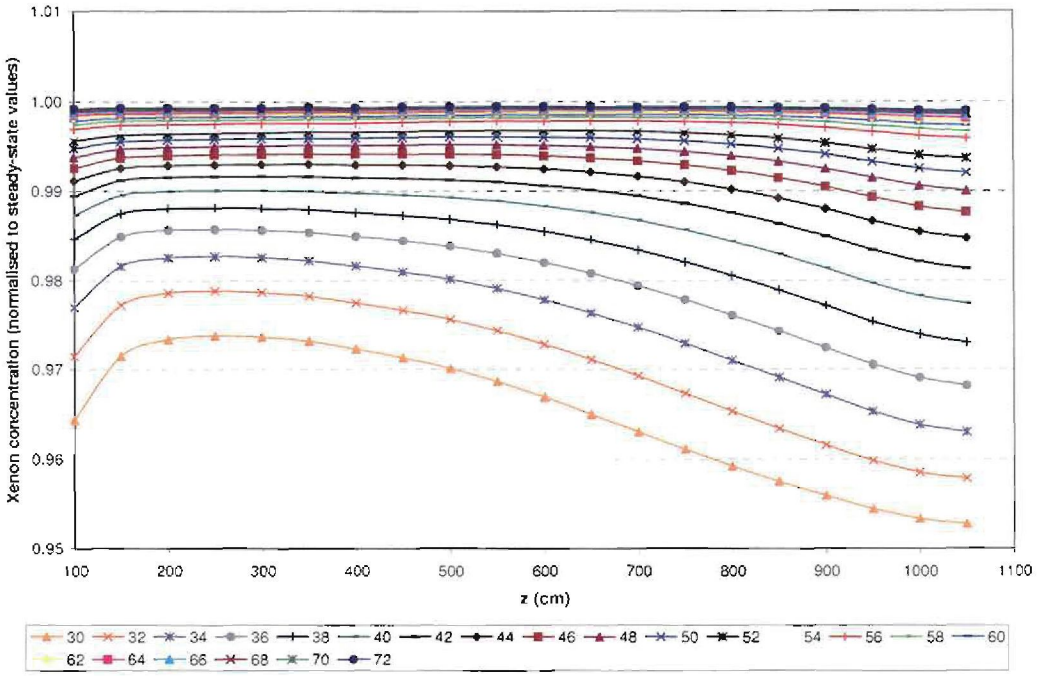

Figure 5-13: Case 6 normalised axial xenon concentration profiles at r = 180 cm, from 30 h - 72 h

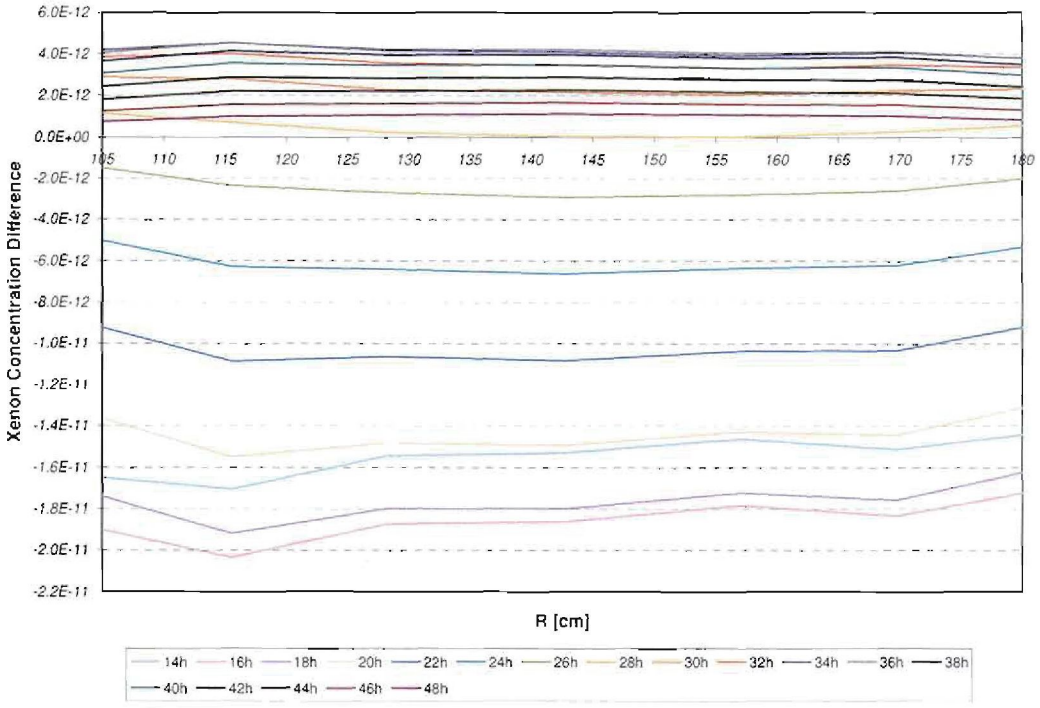

Figure 5-14: Case 5 radial xenon concentration profiles at z = 800 cm, from 14 h - 48 h

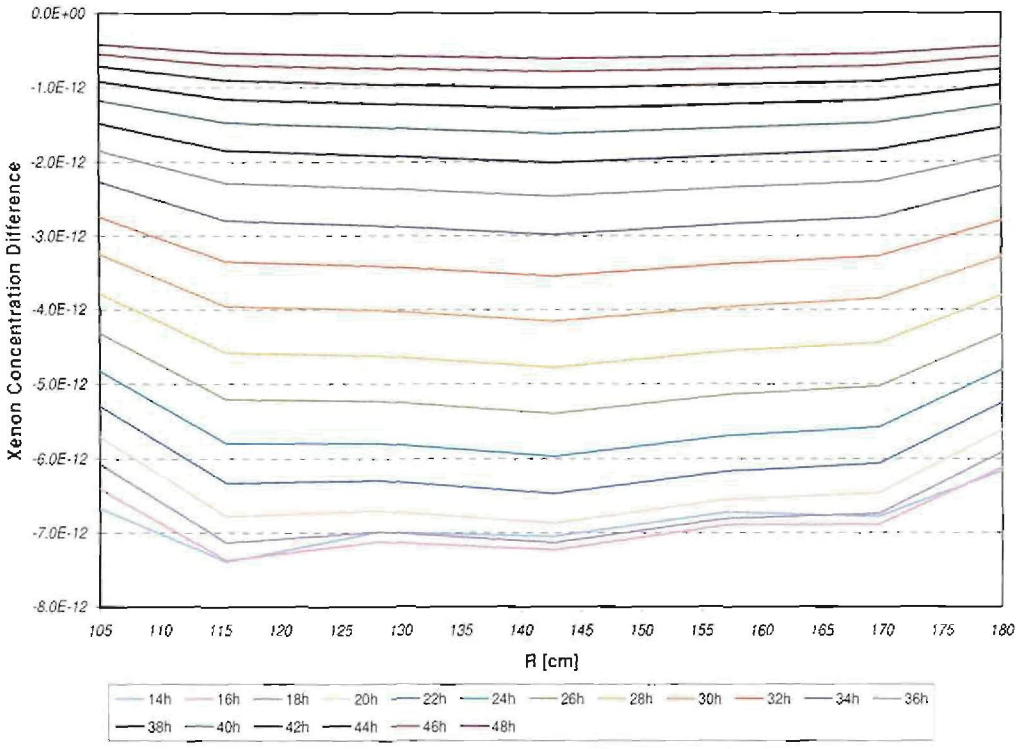

Figure 5-15: Case 6 radial xenon concentration profiles at z = 800 cm, from 14 h - 48 h

5.2.2 Power Density

As already discussed in Section 4.2.4, one of the most important issues in xenon stability is actually not the behaviour of the xenon concentration, but rather the effect of its variations on the spatial power density, via the thermal flux changes. The power density is an important indicator in fuel safety studies, since it directly influences the fuel temperatures, fuel integrity and fission product releases. Currently the PBMR has an operational limit of 4.5 kW per fuel sphere, while the core-averaged power generation per fuel sphere is less than 1 kW/sphere at 400 MW. The maximum spatial power density for the PBMR 400 MW equilibrium core at steady-state is ~ 10.2 W/cm^3, or ~ 1.3 kW/sphere. This means that the PBMR fuel is operated far below the safety margins, and the maximum local power density would have to increase with more than 300% to reach limiting power density values.

The changes in the core power density for case 5 at 9 spatial locations are shown in Figure 5-16. The largest increase (from 3.5 W/cm^3 to 8.9 W/cm^3) in this set occurs at an axial height of 200 cm, due to the movement of the control rod tips at this axial level and the shape of the axial power profiles. It can be seen that the power density values during this load-follow event do not reach any safety limits, and the variations occur over a long enough period not to cause any excessive fuel heat-up rates.

The changes in the core power density for case 6 are shown in Figure 5-17, where the largest differences between the two cases can be see between t = 8 h and 16 h. In this interval, the power densities in the upper part of the core (i.e. at z = 100 to z = 300 cm) decrease for case 5, while the values increase back to their nominal values for case 6.

The amplitude of these variations is also significantly larger for case 5 (e.g. from 7.1 W/cm^3 to 1.3 W/cm^3 at z = 100 cm), compared to the inverse case 6 variations in the same location (from 1.0 W/cm^3 to 2.9 W/cm^3). The decrease in the power levels in the upper part of the core is caused by the deeper insertion of the control rods during this interval (see Figure 5-1), which forces the axial power peak downwards. This perturbation in the local flux by the control rods in the upper part of the core is the root cause of the strong axial oscillations in the xenon and power density variables during a power load-follow.

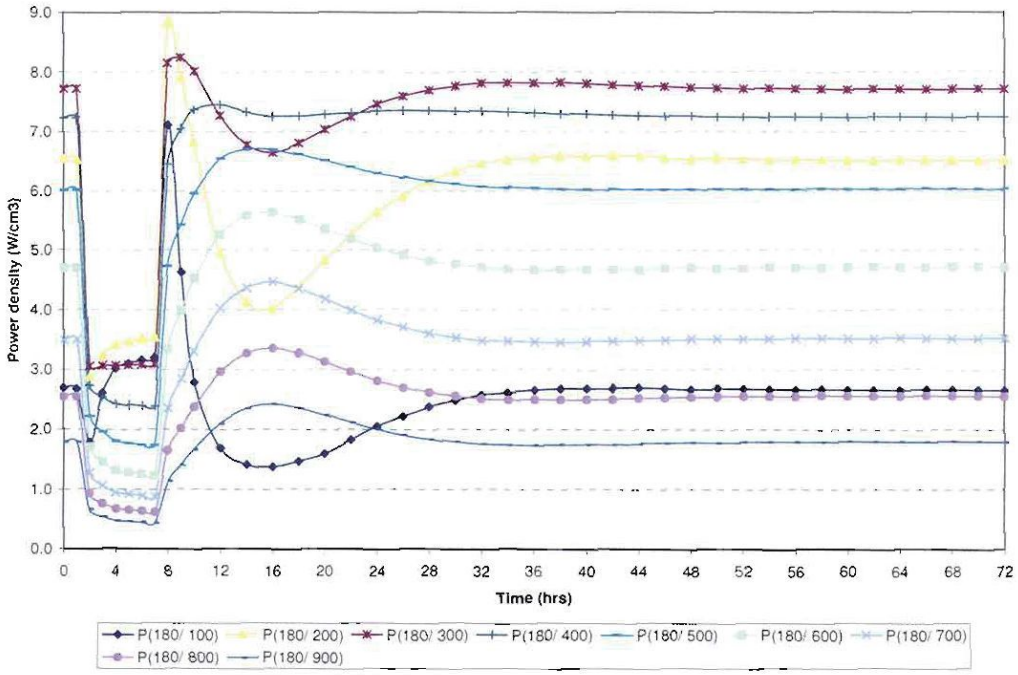

Figure 5-16: Case 5 spatial power density vs. time at 9 axial locations, and r = 180 cm

The normalised power density variations in Figure 5-18 (case 5) and Figure 5-19 (case 6) also clearly show the differences in the spatial power oscillations: the amplitude is much larger for case 5 (from a factor 2.6 to 0.5 at z = 100 cm) compared to the inverse pattern for case 6 (from 0.35 to 1.02 at the same location).

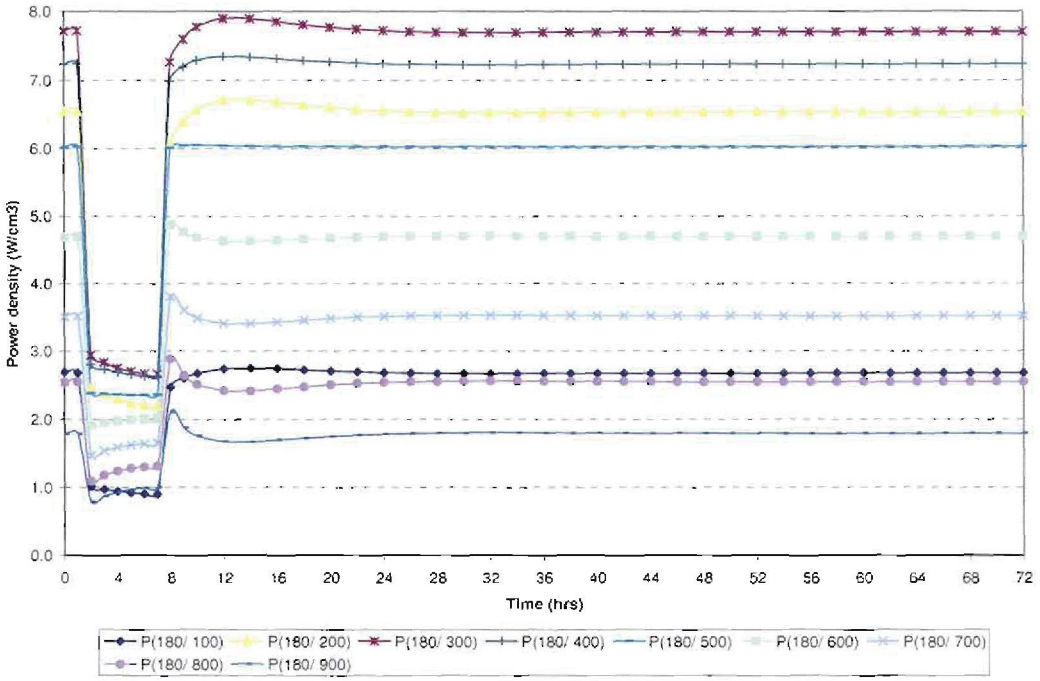

Figure 5-17: Case 6 spatial power density vs. time at 9 axial locations, and r = 180 cm

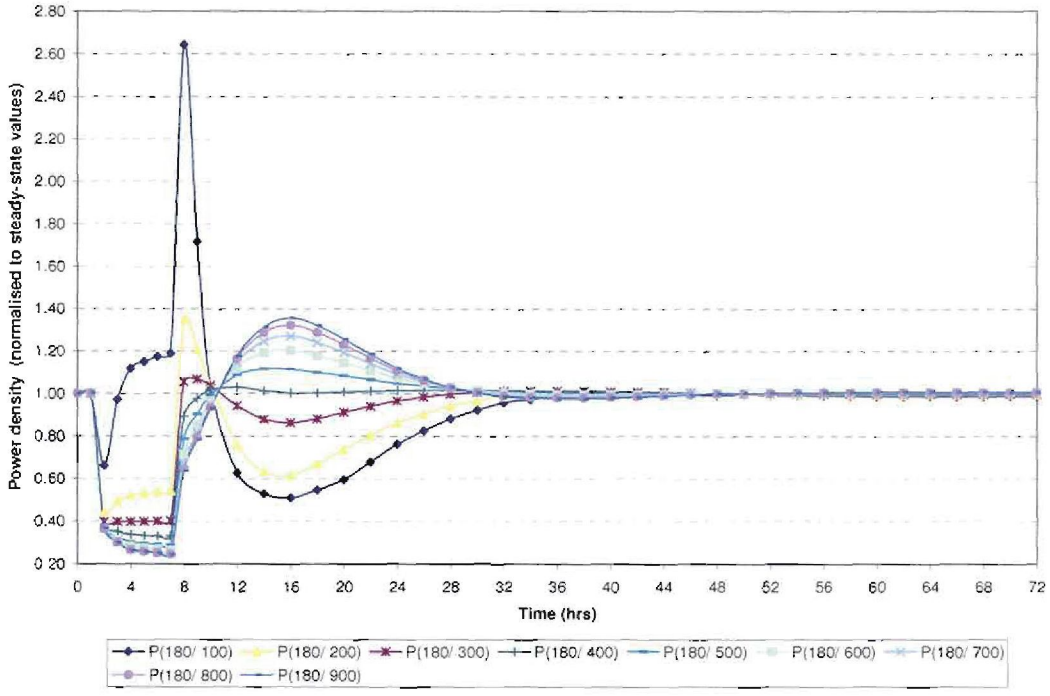

Figure 5-18: Case 5 normalised spatial power density vs. time at 9 axial locations, and r = 180 cm

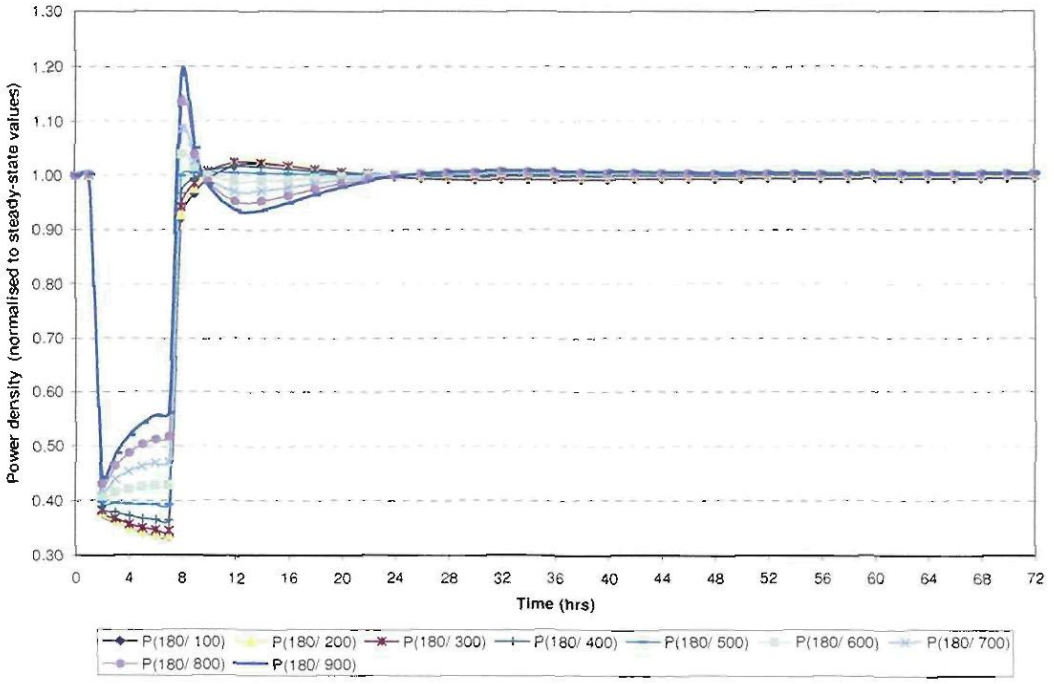

Figure 5-19: Case 6 normalised spatial power density vs. time at 9 axial locations, and r = 180 cm

Axial oscillation nodes can be detected for case 5 (z ~ 400 cm) and case 6 (at z ~ 510 cm) in Figure 5-20 and Figure 5-21. The locations of the nodes differ by almost a meter between the cases due to the movement of the control rods in the upper part of the core. The node location for case 5 is very similar between the xenon (see Figure 5-10) and power density variables – both nodes are located around z ~ 400 cm. It is interesting to note that although only weak axial xenon oscillations were observed for case 6 (Figure 5-12), the power density is also a function of fuel and moderator temperatures, which do vary between the 40% and 100% phases. These local variations are enough to introduce a small oscillation in the axial power density for case 6. To investigate the effect of the moving control rods on the axial power density shape in case 5, the axial shape variations are shown between t = 30 h and 72 h in Figure 5-22, and between t = 54 h and 72 h in Figure 5-23.

The influence of the rods can still be seen in the axial shapes at 30 h, 32 h and 34 h (indicated by arrows in Figure 5-22), but by t = 54 h the rods have stopped moving, and the axial shape variations are similar to the axial variations of case 6's, shown in Figure 5-24. The "skewness" of the curves in Figure 5-23 and Figure 5-24 is caused by the redistribution of the spatial fuel and gas temperature fields when the power and gas ramps are taken back from 40% to 100% (as well as the movements of the control rods for case 5). Note however that these differences deviate less than 1% from the nominal axial power shape (the enlarged scale of the figures might be visually misleading).

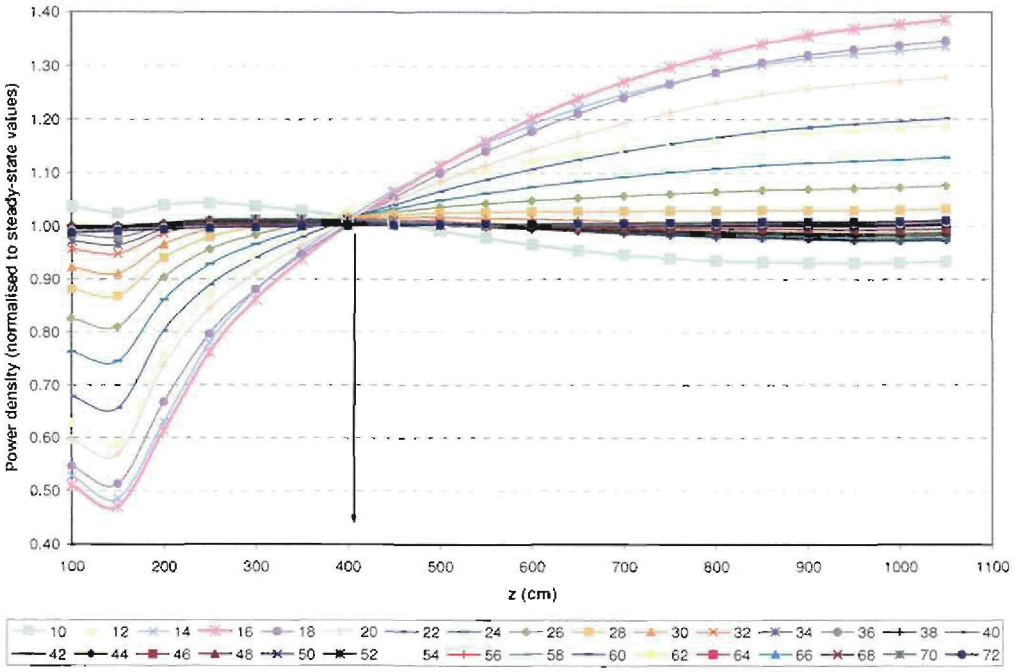

Figure 5-20: Case 5 normalised axial power density profiles at r = 180 cm, from 10 h - 72 h

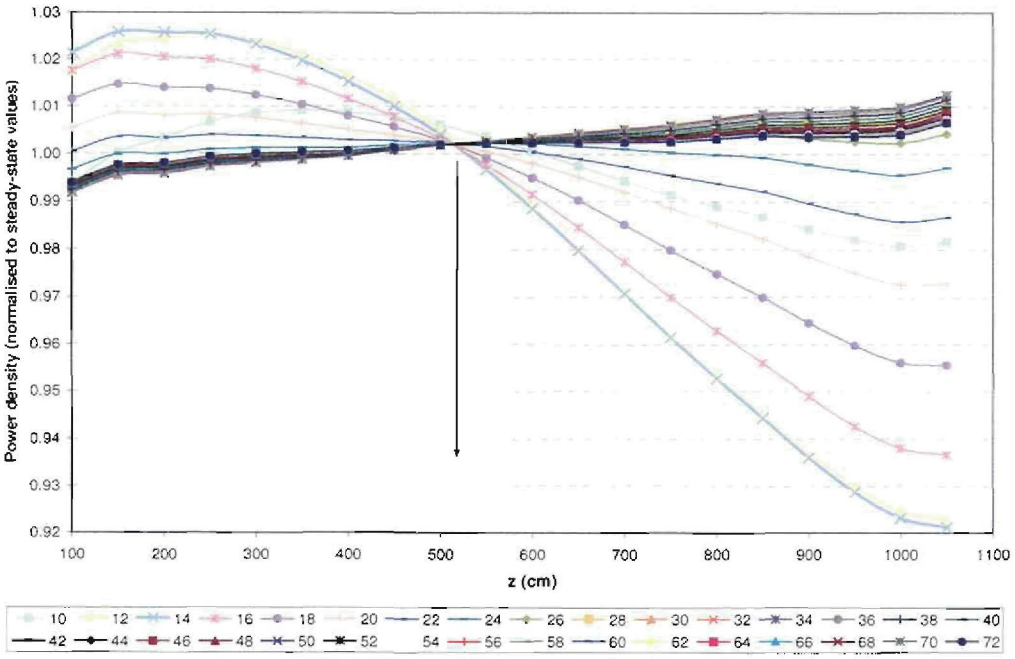

Figure 5-21: Case 6 normalised axial power density profiles at r = 180 cm, from 10 h - 72 h

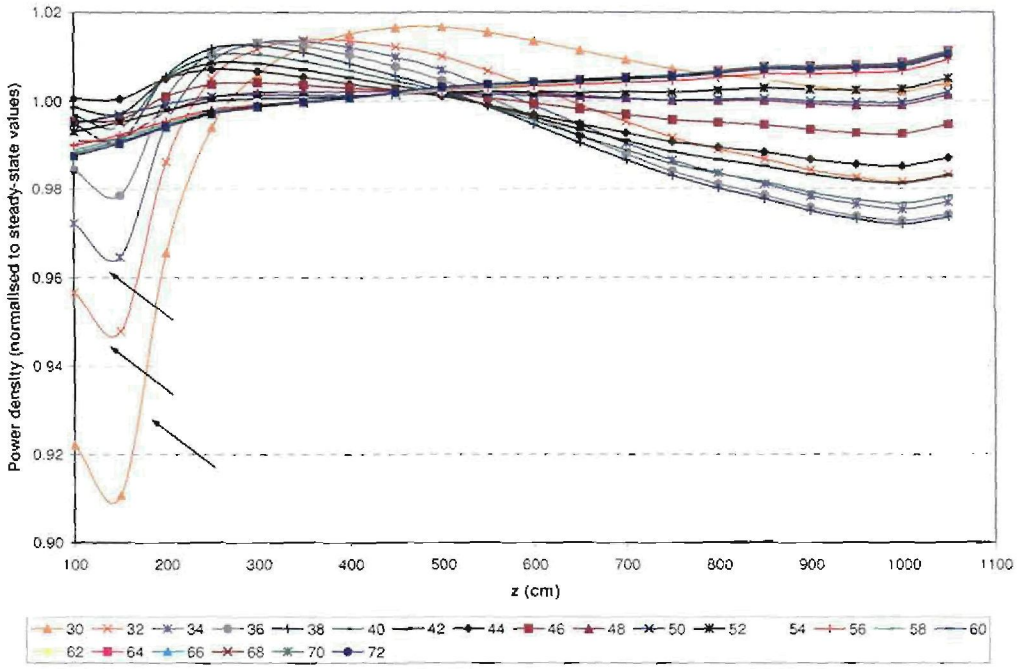

Figure 5-22: Case 5 normalised axial power density profiles at r = 180 cm, from 30 h - 72 h

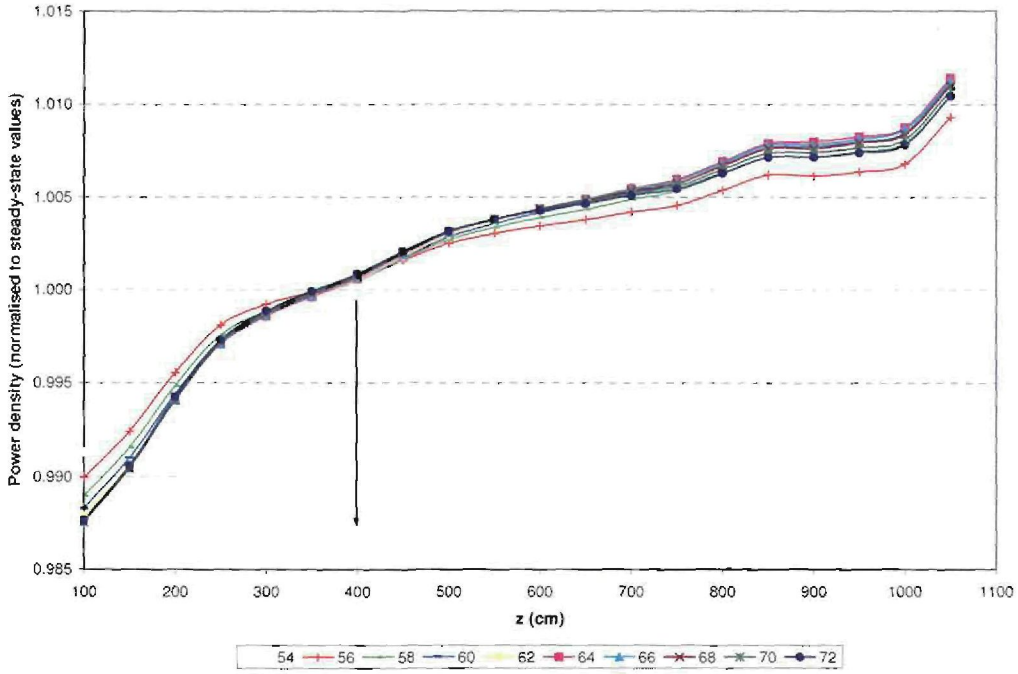

Figure 5-23: Case 5 normalised axial power density profiles at r = 180 cm, from 54 h - 72 h

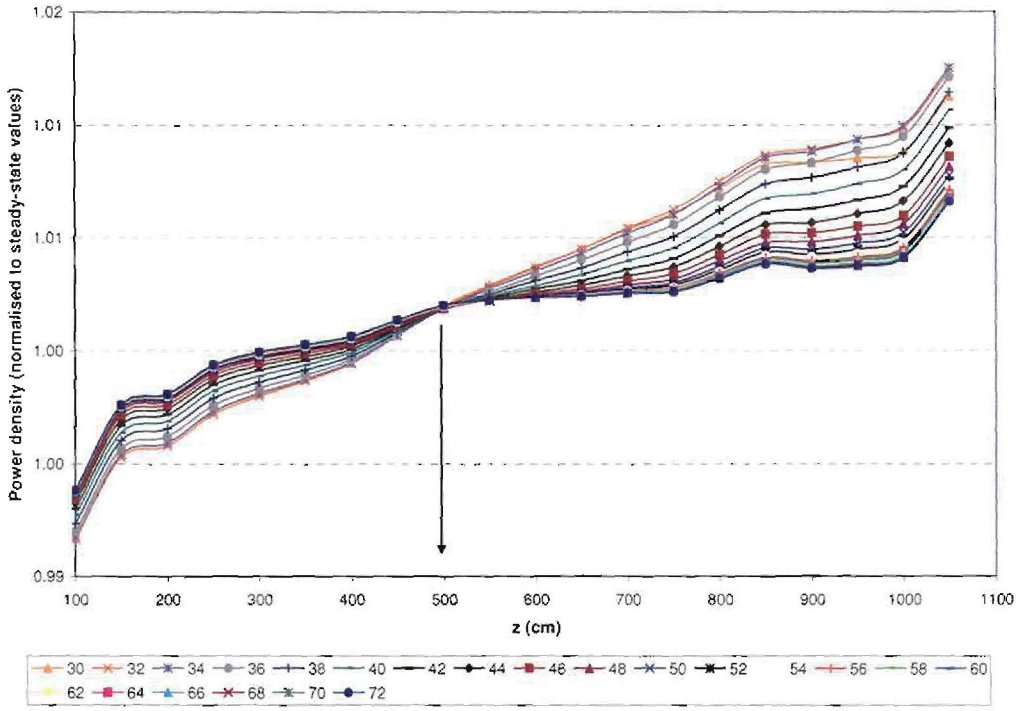

Figure 5-24: Case 6 normalised axial power density profiles at r = 180 cm, from 30 h - 72 h

5.3 QUALITATIVE POWER DENSITY DAMPING STABILITY DATA

Figure 5-25 and Figure 5-26 present the results from the application of the least-squares fitting method to the normalised spatial xenon concentrations of case 5, as introduced in the discussion of Table 4-2. The following restrictions apply to this method as applied to the transients in this chapter:

- The data for cases 5 and 6 are normalised to their steady-state values. Since these two cases use identical steady states as starting conditions, the initial normalisation between the data values for the two cases are also identical, and a direct comparison between normalised values can be performed.
- The full complex spatial oscillation modes that exist in the core are only treated approximately by this method. For example, it was shown in Figure 5-9 that two possible axial modes exist during the early stages of case 5, while a recent study on BWR cores [8] showed that various excitation modes are possible, depending on the initial disturbance size and type. This study also showed that higher order axial and azimuthal harmonics are overlaid on the fundamental or first modes. These factors can be modelled by explicit mathematical approaches developed over the last decade or so, but since the existence of the higher harmonics leads to non-linear spatial effects, such a mathematical treatment is beyond the scope of this study.

- The method cannot incorporate the initial disturbances that caused the spatial oscillations, since the method is formally only valid for free-running linear oscillations. Only the free-running parts of the transients should therefore be included in these fits, e.g. from t = 44 h onwards for case 5, or from t = 8 h for case 6. However, for case 6 the control rods only move about 35 cm from t = 20 h onwards (compared to more than 260 cm between t = 7 h and 16 h), and the least-squares fits have been applied from t = 20 h for case 5. Separate tests showed that the application of the least-squares method at later time points in case 5, e.g. t = 44 h, did not produce significantly different quantitative results.

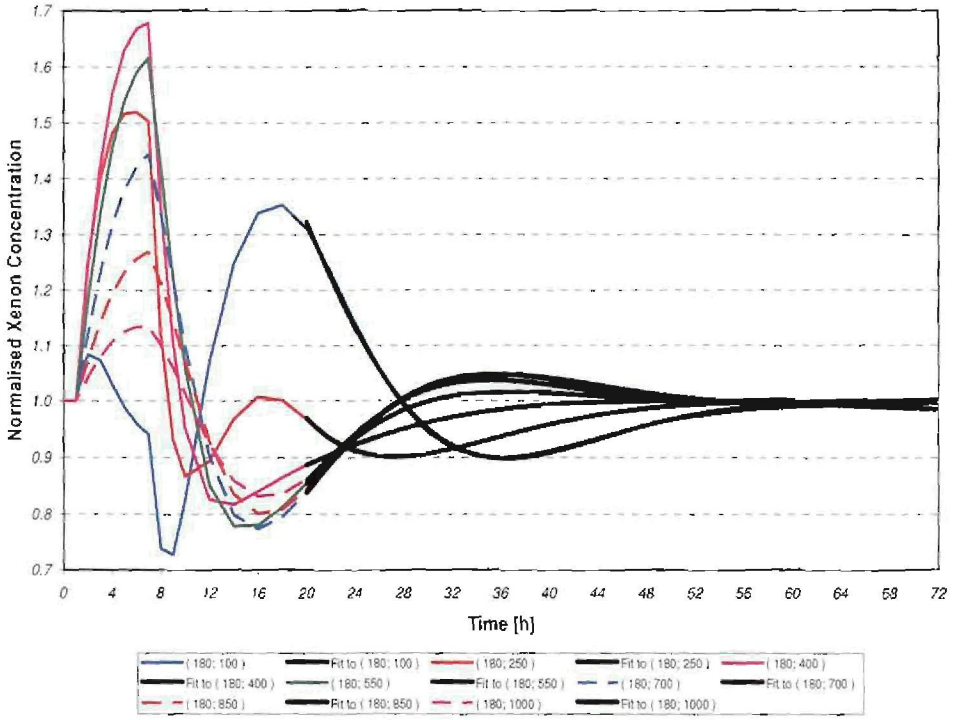

Figure 5-25: Case 5 least square fits to the normalised xenon concentration variations with time, at 7 axial locations and r = 180 cm

A good example of the decrease in the fit quality due to the interference of the moving control rods is shown in Figure 5-25, and with more detail in Figure 5-26. The least-squares fits in these figures have been applied from t = 20 h onwards for case 5, and a visual comparison in Figure 5-26 shows that the fit quality is quite good at all locations, except for the highest point in the core (at z = 100 cm). At this location, the insertion of control rods had a strong effect on the local xenon and thermal flux level, and the "noise" introduced by the rods could not be fitted very well with the least-squares method.

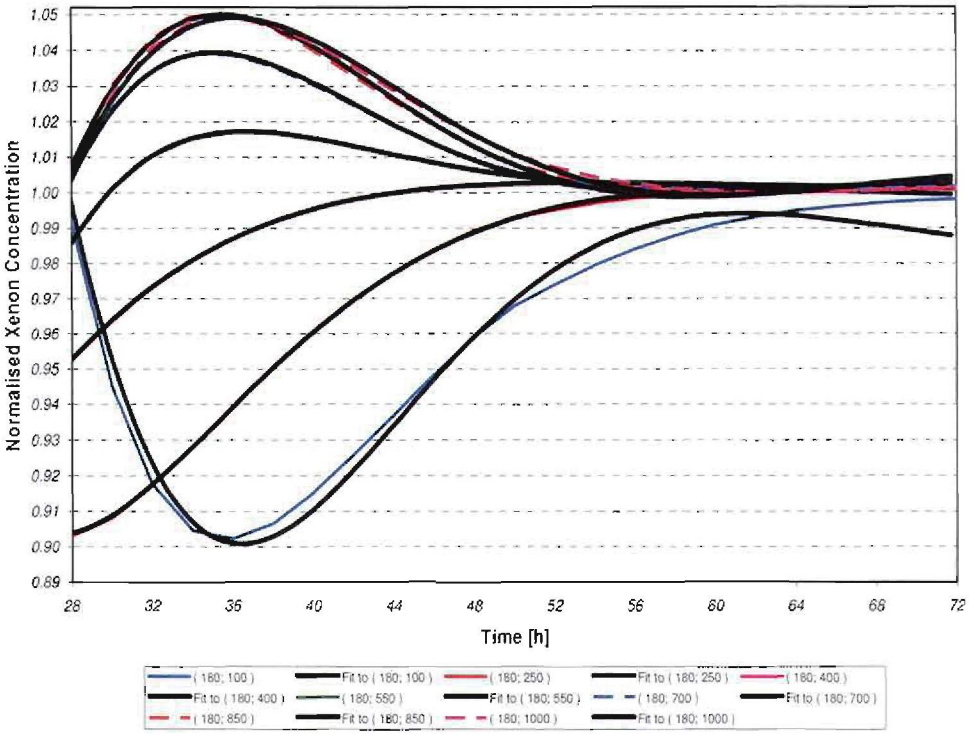

Figure 5-26: Case 5 least square fits to the normalised xenon concentration variations with time, at 7 axial locations and r = 180 cm. Detail between 28 h and 72 h

It therefore implies that the quantitative data obtained for case 5 from the fits at these "high" locations (i.e. axial regions where the control rods have a strong effect) will not be representative of the inherent spatial oscillation damping properties for this case, since the data at these points will be influenced by the strong absorber presence of the control rods. However, the oscillation damping data at these points will still be included in the full dataset for comparison with case 6.

The normalised power density least-squares fits shown in Figure 5-27 and Figure 5-28 are included here as visual examples of the fit quality for cases 5 and case 6.

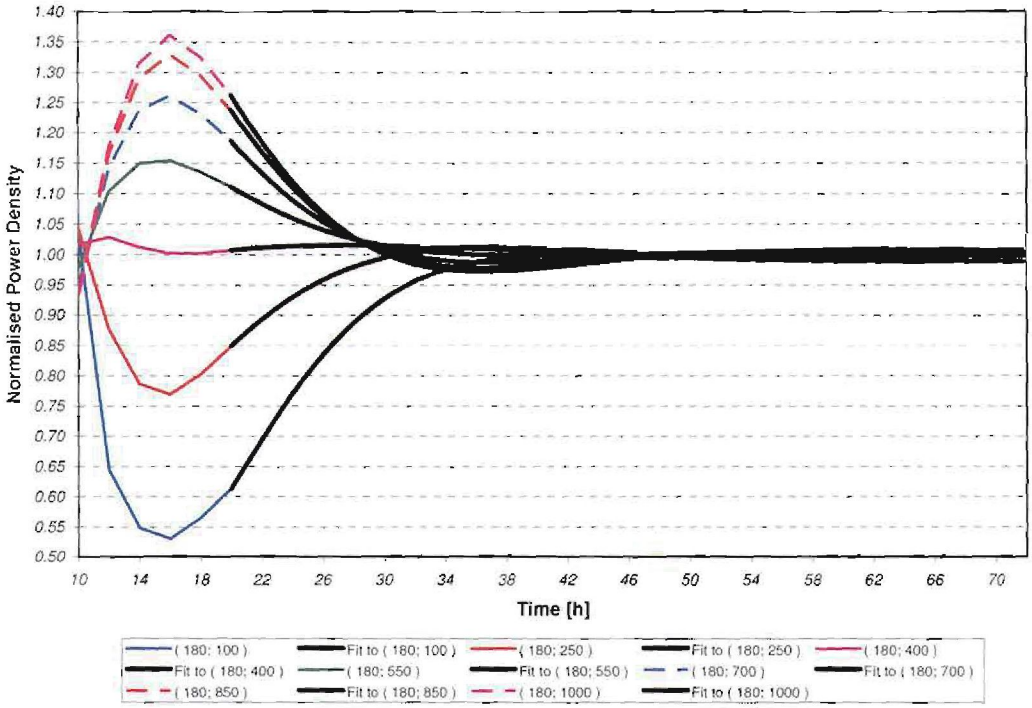

Figure 5-27: Case 5 least square fits to normalised power density variations with time, at 7 axial locations and r = 180 cm. Detail between 10 h and 72 h

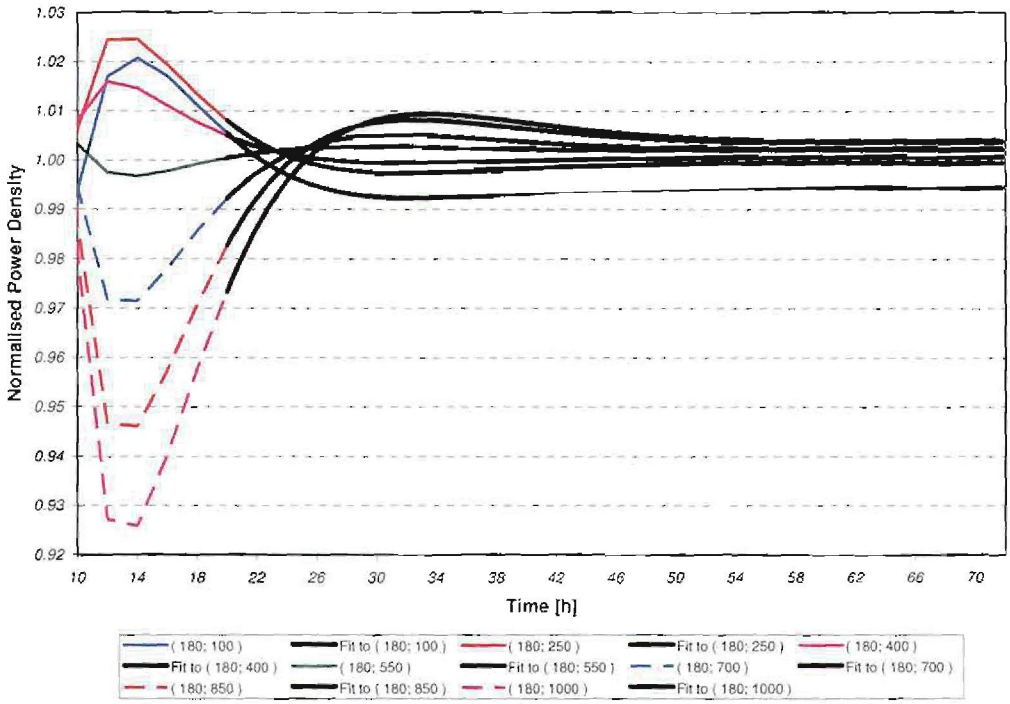

Figure 5-28: Case 6 least square fits to normalised power density variations with time, at 7 axial locations and r = 180 cm. Detail between 10 h and 72 h

Table 5-2 presents the cases 5 and case 6 average power density oscillation damping data for the damping constant b, the damping ratio ξ and the damping period T_D. The table shows that the average power density damping ratio for case 6 (0.56) is higher than the value for case 5 (0.48), i.e. that a reduction in the inherent damping stability is observed for a typical power load-follow transient when the control rods are moved to maintain core criticality.

Table 5-2: Case-averaged power density stability data for case 5 and case 6

Case 5			Case 6		
Damping constant b	Damping ratio ξ	Damped period T_D	Damping constant b	Damping ratio ξ	Damped period T_D
0.12	0.48	51	0.13	0.56	55

This observation is confirmation of the more general work that Stacey performed in the early 1980's [17]. A few secondary remarks could also be made here:

- The least-squares fits have been applied from t = 20 h onwards. This is acceptable for case 6, where no spatial disturbances occur after t = 7 h, but the control rods are still moving up to t = 44 h in case 5. The application of the least-squares fits to the spatial variations from t = 20 h onwards are therefore questionable, since the fits should formally only be applied to "free"-running oscillations. However, it is felt that the comparison of Cases 5 and 6 would be adversely affected if fits at different starting points were used, so the decision was made to wait for the "main" disturbances to die out (i.e. wait until t = 20 h), before the fits were attempted. The average data was calculated in a similar manner to before, i.e. over all spatial points except the central nodal locations.
- The data for case 6 can be directly compared with the case 1 data for an assessment of inherent stability, since both transients exclude any control rod movements during the free oscillation phase, but very different xenon excitation mechanisms. In Section 4.2.4 the current PBMR equilibrium core operating at 400 MW was characterised by a set of inherent xenon stability parameters of b = 0.14, ξ =0.53, and T_D = 49 h. The damping ratio value for case 5 (0.48) is slightly lower than the value for case 1 (0.53), and case 5 also exhibits a slightly longer damped period (51 h vs. 49 h). This minor decrease in inherent stability could be caused by a variety of factors. One of these is the fact that for case 1 a strong control rod insertion was used as the perturbation source, while the power level variations in case 5 caused the xenon/power oscillations. This leads to a strong suppression of the thermal flux levels in the top part of the core for case 1, while the flux levels in case 5 dropped by 60% over the entire volume of the core. However, this small decrease in stability is not of major significance.

5.4 SUMMARY

The axial xenon stability of the PBMR design under 100%-40%-100% load-follow conditions was investigated in Chapter 5. In contrast to Chapter 4, where artificial control rod movements were used to induce axial xenon and power density oscillations, the load-follow transient in this chapter required realistic movement of the control rods to maintain the core criticality.

The 100%-40%-100% load-follow transient was modelled with (case 5) and without (case 6) control rod movements to quantify the effect of the axial rod movements on the xenon stability. It was found that average power density damping ratio for case 6 (0.56) is higher than the value for case 5 (0.48), i.e. that a reduction in the inherent damping stability is observed for a typical power load-follow transient when the control rods are moved to maintain core criticality. This observation therefore confirmed the more general work that Stacey performed in the early 1980's [17]. The axial movement of the rods influences is especially noticeable in the de-stabilisation of the xenon oscillation damping.

The data for case 6 can also be directly compared with the case 1 data for an assessment of inherent stability, since both transients exclude any control rod movements during the free oscillation phase, but very different xenon excitation mechanisms. In Section 4.2.4 the current PBMR equilibrium core operating at 400 MW was characterised by a set of inherent xenon stability parameters of b = 0.14, ξ =0.53, and T_D = 49 h. The damping ratio value for case 5 (0.48) is slightly lower than the value for case 1 (0.53), and case 5 also exhibits a slightly longer damped period (51 h vs. 49 h), but this small decrease in stability is not of major significance.

The findings in this chapter therefore illustrate that the inherent xenon stability of the PBMR core is not dependent on the excitation mechanism, and secondly that although the movement of the control rods de-stabilise the xenon oscillation damping, the core still exhibits well-damped behaviour under realistic load-follow transients.

In Chapter 6, the xenon stability results from two parametric studies on the duration and final power level of the general load-follow transient will be reported, to ensure that the findings of this chapter are confirmed for a large range of possible core power states.

CHAPTER 6

6. AXIAL XENON OSCILLATION STABILITY RESULTS FOR OTHER POWER LOAD-FOLLOW TRANSIENTS

In Chapter 5 it was shown that the control rod movements during a 100%-40%-100% load-follow transient lead to a decrease in the xenon-induced axial power oscillation stability of the PBMR core. In this chapter, the xenon oscillation stability results for several load-follow transients are investigated to determine if the conclusions made in Chapter 5 are valid for these general power variations as well.

The results of a set of 100%-50%-100% transients are included in Section 6.1, where the 50% power phases were specified for various durations from 6 h to 24 h. Since the duration of the low power phase essentially varies the excitation magnitude (see Table 6-2 in Section 6.1), this sensitivity study can be used to determine if any relationship exists between the amplitude of the initial perturbation and the resulting xenon oscillation damping stability. Section 6.2 contains the results of a similar sensitivity study on the relative damping stability of various increased final power levels, where the total power levels are varied from 400 MW to 800 MW. (Note that the power levels selected for these transients are intended as examples only- there is no intention to operate the current PBMR design at 500 MW to 800 MW power levels).

The two studies should conclude that there is no dependency on the amplitude of the initial perturbation, but that an increase in power level would lead to a decrease in stability. (These conclusions can be expected from the basic driving mechanisms of xenon oscillation stability, as discussed in the components of Eq (2.5), Section 2.2).

Since a large quantity of data can be presented for these cases (if a detailed analysis comparable to case 5 is reported here), this section will only contain the data for the comparison between the cases for the following parameters:

- the movement of the control rods for Cases 7 to 10, with specific focus on the maximum and minimum values reached, and the magnitude of the core-averaged xenon levels;
- the variance in the damping ratio ξ for the various cases, with the focus again on the power density variances. The detailed data on the spatial variances in the power density, fast and thermal fluxes, and the iodine and xenon concentration levels are included in the more detailed PBMR report [25].

6.1 CASES 7 TO 10: SENSITIVITY STUDY ON THE DURATION OF THE LOW POWER PHASE

This sensitivity study investigates the effect of the duration of a low power phase on the stability of the load-follow event. Since the results of case 5 indicated that the control rods are completely withdrawn from the core to overcome the build-up of xenon during a 100%-40%-100% transient, Cases 7-10 are all defined as 100%-50%-100% load-follow events, to ensure that the control rods do not reach the fully withdrawn location.

The control rod "dead time" (i.e. the period when the rods are fully withdrawn) introduces unnecessary complicating spatial flux effects, while a 50% power level would allow full control rod control for the entire load-follow duration.

Data from 8 sub-cases are presented here: Cases 7a to 10a include the movement of the control rods to keep the core critical (and therefore form the realistic set for the operating PBMR core), while Cases 7b to 10b exclude all control rod movement, and use the TINTE external reactivity controller to keep the core critical. The cases all follow the same sequence of events:

- The main inlet gas flow rate is decreased from 100% (192.7 kg/s) to 50% (96.35 kg/s) over 6 minutes, starting at t = 1 h.
- The reactor outlet pressure is decreased from 87.9 to 43.95 bar over 6 minutes, also starting at t = 1 h. (The CBCS mass flow and pressure are also reduced by the same ratios).
- A reactor total power ramp from 100% to 50% is also applied in the same period to match the total reactor power with the fluidic power decrease during the transient. The TINTE auto-reactivity controller is instructed to move the control rods to keep the reactor critical during the event (Cases 7a to 10a), or to utilise the global external reactivity parameter (Cases 7b to 10b).
- The duration of the 50% power phases are 6 h (case 7), 12 h (case 8), 18 h (case 9) and 24 h (case 10). The ramps back to 100% power therefore occur at the following times in the transients respectively: t = 7, 13, 19 and 25 h.
- The transients are calculated for a total of 72 h, without any further boundary condition changes.

It is important to note that since this section focuses on the damping stability of these variations on the 100%-50%-100% load-follow, the interference from the movement of the control rods could play a significant role in the distortion of the inherent xenon stability. Figure 6-1 shows the change in the control rod location for Cases 7a to 10a, while Table 6-1 presents a summary of the minimum and maximum control rod depths reached during the phase when the power is returned to 400 MW. Of interest in these data is the distance that the control rods were inserted to counter the decay of xenon, since this distance is related to the magnitude of the xenon perturbation.

The data show that case 7a reaches a fully withdrawn control rod location for a short period (5 minutes) due to the ramp back to 100% power, from where the rods are inserted to 255 cm over the next 4 h. This is in contrast to case 10a, where the rods were only inserted a distance of 95 cm (from 241 cm to 336 cm).

Table 6-1: Summary of control rod minimum and maximum locations and xenon maximum absorption levels for Cases 7a to 10a

Case	50% Phase duration (hr)	Control rod depth at end of 50% power phase (cm)	Maximum control rod depth (cm)	Net distance inserted due to ramp back to 400 MW (cm)
7a	6	0	255	255
8a	12	96	296	200
9a	18	192	327	135
10a	24	241	336	95

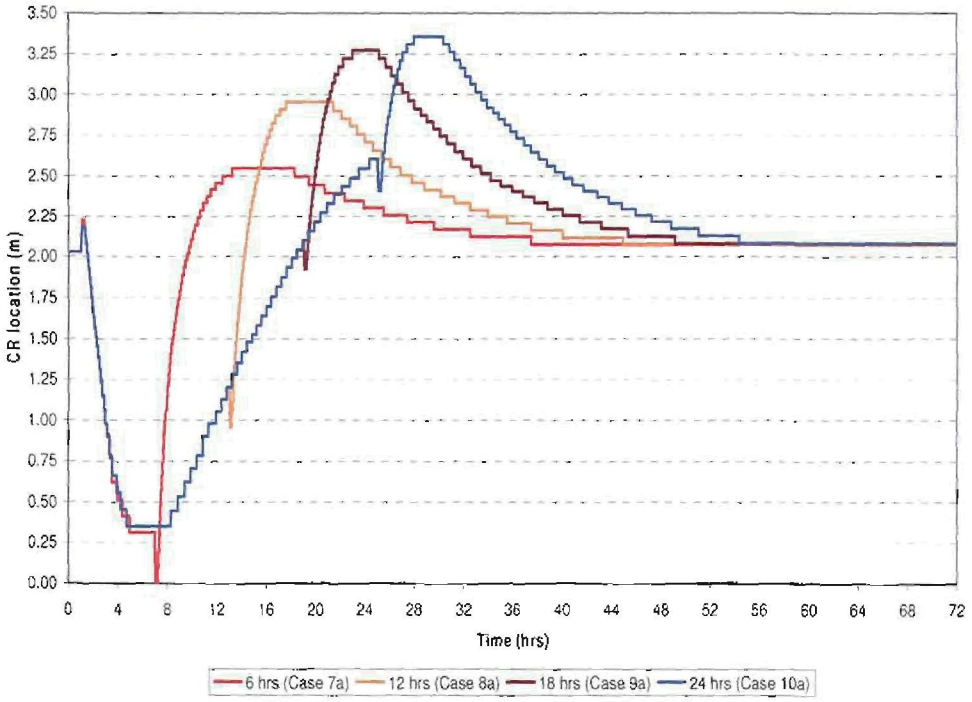

Figure 6-1: Control rod movements for Cases 7a to 10a.

If the behaviour of the control rods is viewed in isolation, the conclusion can be made that case 7a (50% power for 6 h) displays the largest perturbation in the axial xenon/flux fields of these four cases. However, it is interesting to note that the difference in the core-averaged xenon absorption levels of case 7a and case 8a are in fact very similar (Table 6-2 and Figure 6-2), and that the two cases therefore introduce almost identical changes in the core-averaged xenon absorption levels. (The differences were calculated by subtracting the minimum Xenon absorption level for each case from the case-respective xenon absorption levels at the end of the 50% power phase, i.e. when the ramp back to 400 MW was done. This is indicated in Figure 6-2 by arrows for each case).

This perceived difference between case 7a and case 8a can be explained by the lower differential worth of the control rods in the upper part of the core (i.e. between 0 cm and 100 cm), compared to the higher differential worth in the range 100 cm to 200 cm. (The control rod differential worth is defined as the control rod bank reactivity effect per cm of movement, with a unit of pcm/cm). For case 8a, the rods were inserted 200 cm when returning to full power to overcome a decrease in the core-averaged xenon absorption of 0.85%; in case 7a the rods needed 55 cm more to overcome the same decrease in the core-averaged xenon absorption (0.84%) when the return to 400 MW power was made.

Table 6-2: Summary of core-averaged xenon absorption levels for Cases 7a to 10a

Case	50% Phase duration (hr)	Core-averaged xenon Absorption when returning to 400 MW power (%)	Minimum core-averaged xenon absorption (%)	Difference in core-averaged xenon absorption (%)
7a	6	2.77	1.93	0.84
8a	12	2.57	1.72	0.85
9a	18	2.29	1.57	0.72
10a	24	2.06	1.5	0.56

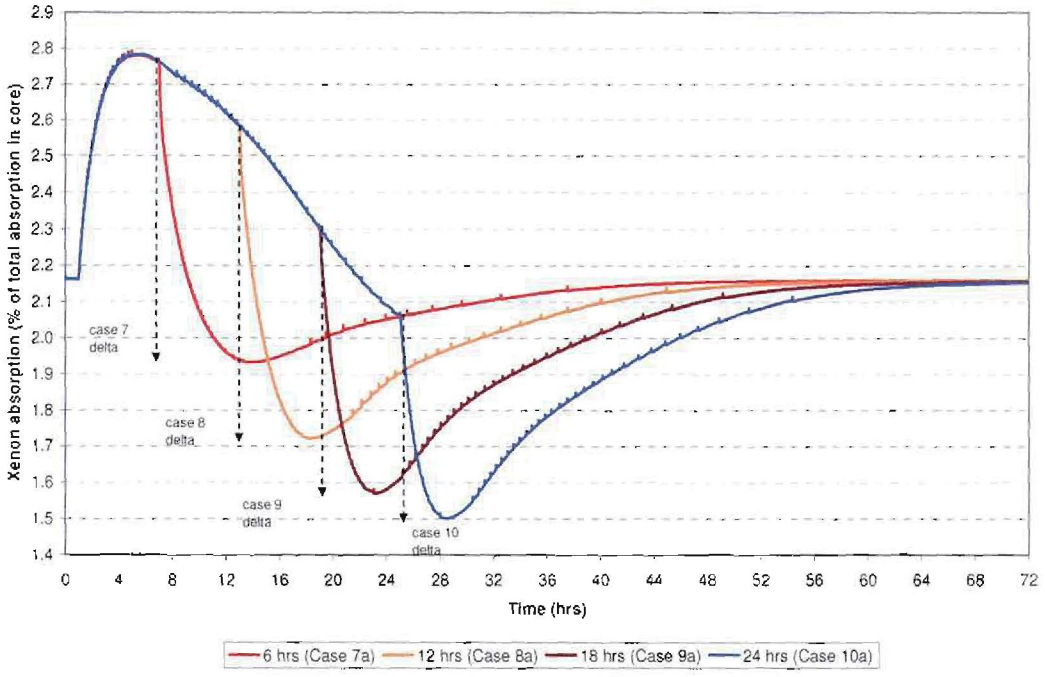

Figure 6-2: Core-averaged xenon absorption (%) for Cases 7a to 10a.

The power density oscillation damping ratios for cases 7a to 10a are presented for 10 spatial locations in the core in Table 6-3, while Table 6-4 presents the same data for cases 7b to 10b, i.e. without any control rod movements. Note that the damping ratio values at location z = 550 cm are not included in the tables, or in the determination of the average values, due to the distorted data close to the axial oscillation nodal point (see Section 4.2.5 for more detail).

Table 6-3: Power density damping ratio ξ for cases 7a to 10a (transients include control rod movements)

Variable	Spatial Location	case 7a	case 8a	case 9a	case 10a
Power density	(105; 100)	0.44	0.37	0.37	0.47
	(105; 250)	0.40	0.42	0.46	0.48
	(105; 700)	0.40	0.39	0.42	0.46
	(105; 850)	0.37	0.38	0.41	0.43
	(105; 1000)	0.36	0.37	0.40	0.42
	(180; 100)	0.49	0.39	0.37	0.52
	(180; 250)	0.41	0.47	0.53	0.54
	(180; 700)	0.40	0.39	0.42	0.46
	(180; 850)	0.37	0.38	0.41	0.43
	(180; 1000)	0.36	0.37	0.40	0.42
Average		**0.40**	**0.39**	**0.42**	**0.46**

Table 6-4: Power density damping ratio ξ for cases 7b to 10b (transients exclude control rod movements)

Variable	Spatial Location	case 7b	case 8b	case 9b	case 10b
Power density	(105; 100)	0.52	0.55	0.54	0.54
	(105; 250)	0.59	0.63	0.61	0.61
	(105; 700)	0.57	0.61	0.60	0.60
	(105; 850)	0.59	0.63	0.62	0.62
	(105; 1000)	0.60	0.64	0.62	0.62
	(180; 100)	0.52	0.54	0.53	0.53
	(180; 250)	0.58	0.62	0.61	0.61
	(180; 700)	0.57	0.61	0.60	0.61
	(180; 850)	0.59	0.63	0.62	0.62
	(180; 1000)	0.60	0.65	0.62	0.62
Average		**0.57**	**0.61**	**0.60**	**0.60**

Two main observations can be made from this data:

- As was previously noted in the discussion of case 5 and case 6, the continuous movement of the control rods over an extended period of time during the transients leads to a decrease in the *inherent* damping stability. This pattern is consistently observed for all variables and all four cases in this section. The power density damping ratio averages decrease from 0.57 (case 7b), 0.61 (case 8b), 0.60 (case 9b) and 0.60 (case 10b) to 0.40, 0.39, 0.42 and 0.46, when the control rod movements are included in the transients.

- A slight variation (0.42 ± 0.04, or 10%) exists in the damping stability from case 7a to case 10a, but if the inherent behaviour of these cases is studied (Table 6-4), no significant variation exists between the cases (0.59 ± 0.02, or 3%). It must also be kept in mind that the oscillation fitting method implemented in this study should actually only be applied to free oscillations, and that the variation from case 7a to case 10a is within the uncertainty bandwidth introduced by the application of the fitting technique to transients where the control rods are still moving.

In summary, it can therefore be stated that the duration of the low power phase does not play a significant role in the power density damping stability of the PBMR design.

6.2 CASES 11-14: SENSITIVITY STUDY ON THE FINAL POWER LEVEL OF A POWER LOAD-FOLLOW

A second sensitivity study was performed on a variation in the final power level of five hypothetical open-ended load-follow transients. The cases all started at 400 MW total power, and after one hour the power levels were varied to 300 MW (case 11), 500 MW (case 12), 600 MW (case 13) and 700 MW (case 14), respectively, for the remainder of the 72 hour transient calculation. The inherent oscillation damping stability results of this set of load-follow transients will be compared with the power level variation results obtained in Section 4.2.4.

It is important to note the differences between the two "power level" studies: In Chapter 4 the total power was kept constant during the transient, and the control rods were inserted and withdrawn to excite xenon-induced power oscillations for four different power cases. In this section, the total power levels are varied during the transients, and the control rods are not moved from their nominal locations at 202 cm. The four cases in this section were only calculated without movement of the control rods, since adequate examples on the destabilising effects of the control rods on the inherent oscillation damping properties have already been shown in the preceding sections.

The normalised power density variations and the least-square fits at 7 axial locations in the core for cases 11 to 14 are presented in Figure 6-3 to Figure 6-6. Since the four cases end up at different power levels, it should be noted that the power oscillations stabilise at different normalised y-axis values after 72 h. It is also noticeable that the nature of the spatial oscillations is similar for case 13 to case 15 (500 MW-700 MW), but that the decrease to 300 MW power in case 11 resulted in a more damped oscillation. This observation is quantitatively confirmed by the power density damping ratio data shown in Table 6-5.

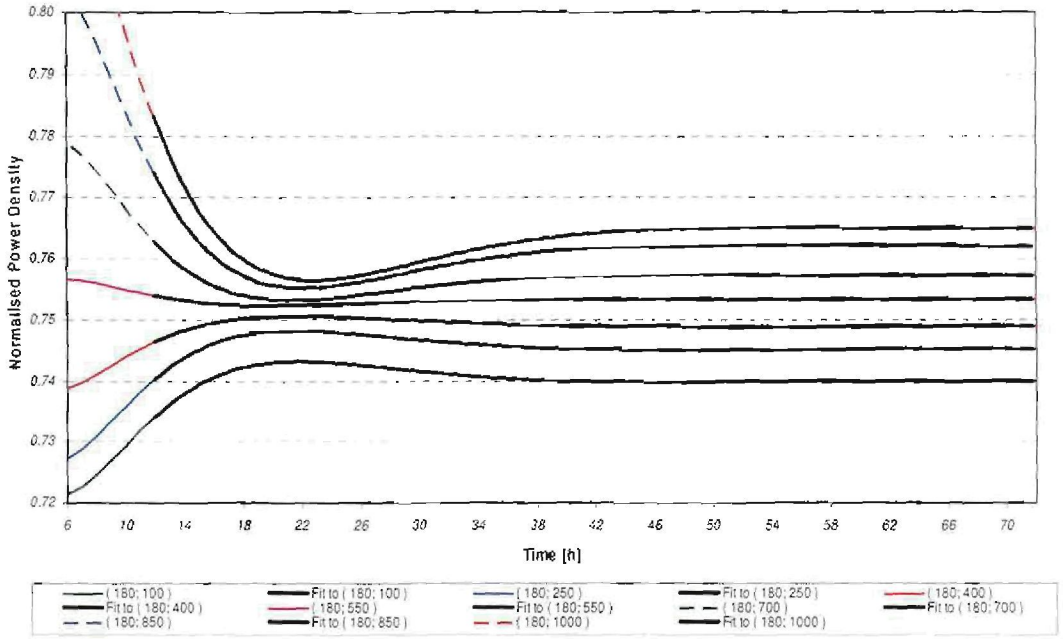

Figure 6-3: Case 11 (400 MW to 300 MW) Least-squares fits to normalised power density variations with time, at 7 axial locations and r = 180 cm

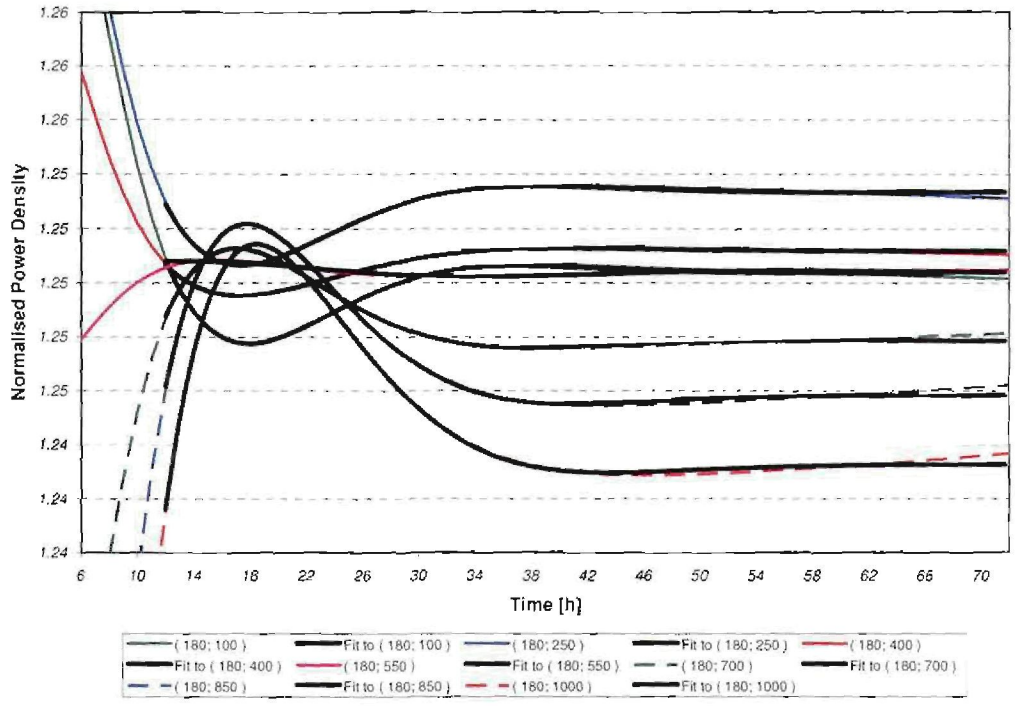

Figure 6-4: Case 12 (400 MW to 500 MW) Least-squares fits to normalised power density variations with time, at 7 axial locations and r = 180 cm

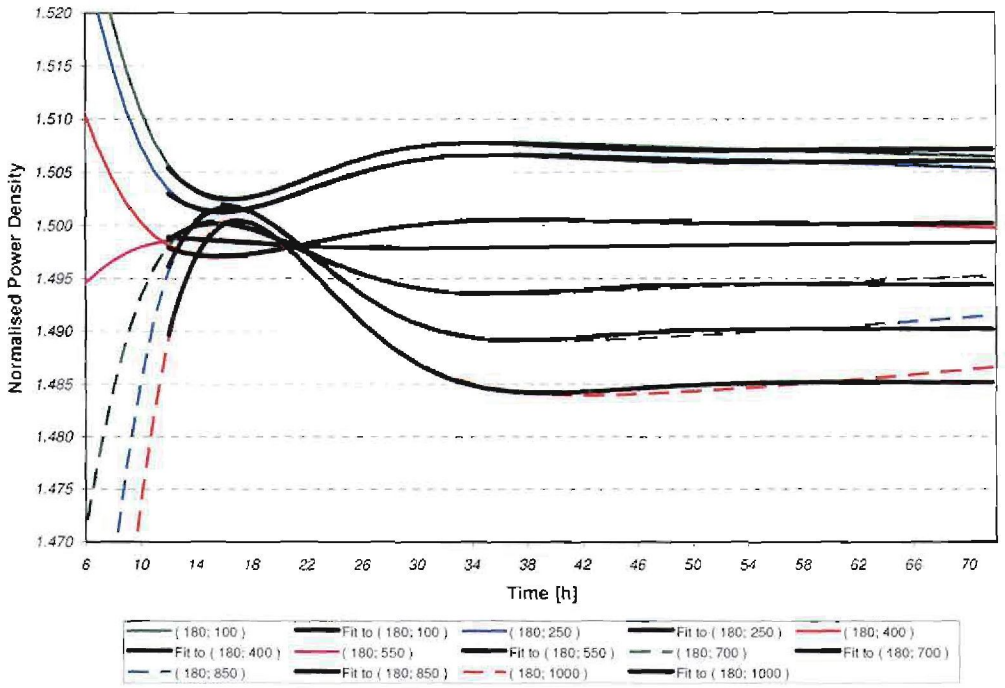

Figure 6-5: Case 13 (400 MW to 600 MW) least-squares fits to normalised power density variations with time, at 7 axial locations and r = 180 cm

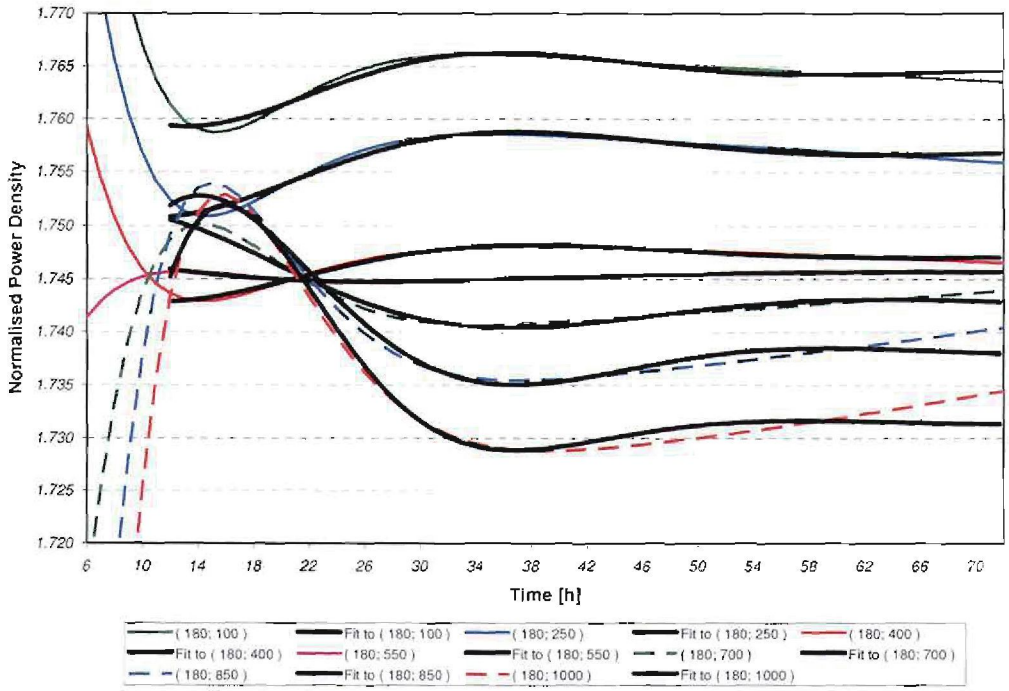

Figure 6-6: Case 14 (400 MW to 700 MW) least-squares fits to normalised power density variations with time, at 7 axial locations and r = 180 cm

The power damping ratios for the four load-follow cases investigated in this section are presented for 7 spatial locations in the core in Table 6-5. The case-average power density damping ratios have again been determined by neglecting the contributions from the two locations close to the axial oscillation node at z = 400 cm and 550 cm.

Table 6-5: Power density damping ratio ξ for cases 11to 14.

Location	Case 11 (400 MW to 300MW)	Case 12 (400 MW to 500MW)	Case 13 (400 MW to 600MW)	Case 14 (400 MW to 700MW)
(180; 100)	0.47	0.37	0.29	0.13
(180; 250)	0.52	0.42	0.29	0.15
(180; 400)	0.58	0.45	0.32	0.19
(180; 550)	0.37	0.08	0.12	0.28
(180; 700)	0.53	0.41	0.28	0.16
(180; 850)	0.57	0.48	0.38	0.21
(180; 1000)	0.60	0.54	0.44	0.31
Average	**0.54**	**0.44**	**0.34**	**0.19**

The decrease in the average power density damping ratios from case 11 (0.54) to case 14 (0.19) confirms the expected outcome of this sensitivity study, i.e. that an increase in the reactor power level leads to a decrease in xenon-induced axial power density oscillation damping stability. This conclusion is in agreement with the general xenon stability theory as discussed in Section 2.2, as well as the findings of Section 5.3, where a similar relationship between the inherent power density damping stability and the reactor power level was observed.

The variation of the power density damping ratio ξ with the final load-follow power level is presented in Figure 6-7. A dotted third-order polynomial fit line is also shown in relation to the source data. The dependency of the damping ratio ξ on the load-follow final power level P is given by the fit expression

$$\xi = -(9.0\text{x}10^{-11})\,P^3 - (1.81\text{x}10^{-06})\,P^2 + (0.001)\,P + 0.4067 \qquad (6.1)$$

with an R^2 value of 0.9995.

The derivative of the damping ratio with the power level can be determined from Eq (6.1) as

$$d\xi / dP = -(2.70\text{x}10^{-10})\,P^2 - (3.62\text{x}10^{-06})\,P + 0.001 \qquad (6.2)$$

If this derivative is evaluated at the nominal power level of 400 MW, a value of -4.91x10^{-04} MW^{-1} is obtained. This value is significantly (57%) smaller than the coefficient obtained for variations in the steady-state power in Section 4.2.4 (-3.12 x10^{-04} MW^{-1}). However, this difference can be expected if the different excitation mechanisms between the two sets of cases are kept in mind (i.e. very strong artificial control rod insertions at constant power for cases 1 to 4 vs. large global power level variations with no control rod movements for cases 11 to 14).

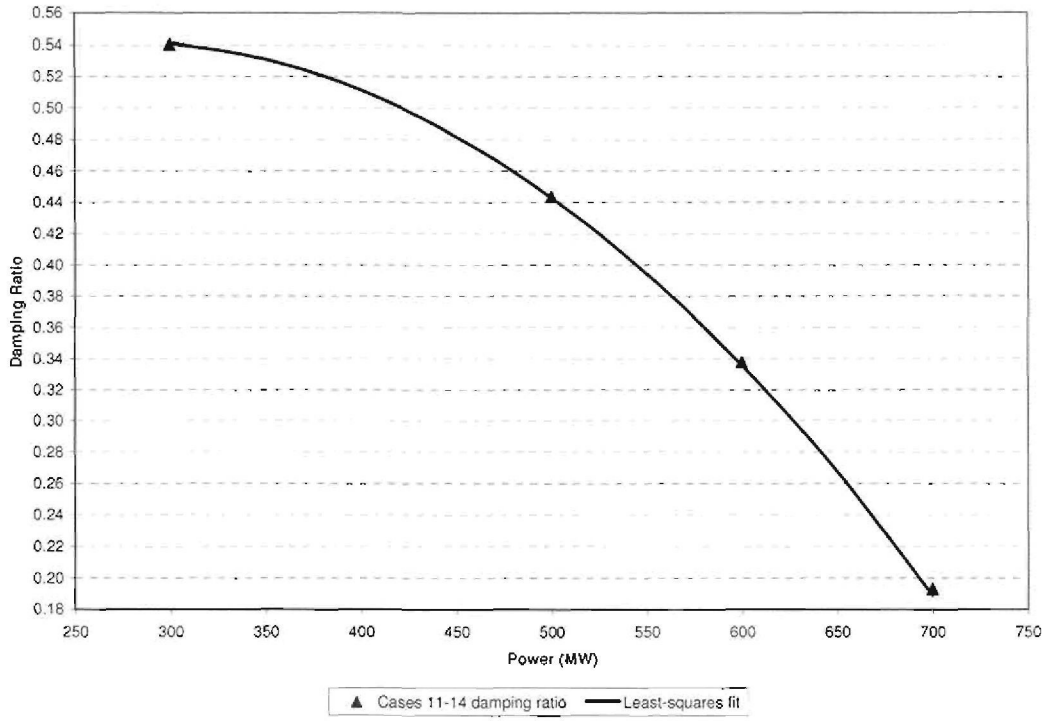

Figure 6-7: Variation in the inherent power density damping ratio ξ with the final load-follow power level.

A quantitative comparison between the two power density damping ratio fits in the range 300 MW to 500 MW is shown in Table 6-6 and Figure 6-8.

Table 6-6: Third-order polynomial fitted power density damping ratio vs. reactor power level for cases 11 to 14 and cases 1 to 4

Power level	Fitted ξ for cases 10-14	Fitted ξ for cases 1-4
300	0.54	0.56
350	0.53	0.54
400	0.51	0.53
450	0.48	0.51
500	0.44	0.48

The data in Figure 6-8 show that the spread between the calculated ξ values for the two inherent oscillation damping transient sets between 300 MW and 500 MW is less than 10%; quantitatively confirming that the inherent power oscillation damping stability is not dependent on/independent of the nature of the perturbation used to study this parameter.

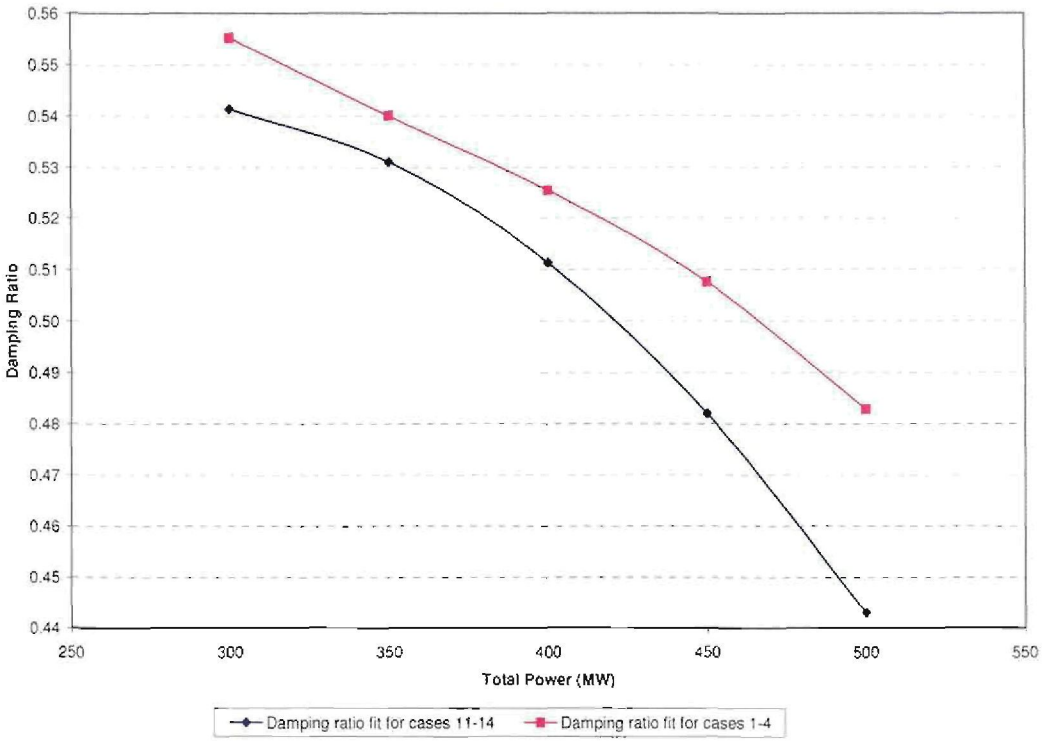

Figure 6-8: Comparison of the variation in the inherent power density damping ratio ξ between cases 1 to 4 and 11 to 14, based on third-order polynomial fit data.

6.3 SUMMARY

The variation in the PBMR xenon-induced power density oscillation stability for several power load-follow transients was investigated in Chapter 6. The aim of this chapter was to establish if the degree of xenon stability quantified in Chapter 5 for the 100%-40%-100% load-follow would also be applicable for other loaf-follow events, and to what extent this load-follow stability is influenced by variations in the duration and amplitude of the power levels. Two sensitivity studies were performed:

1. The duration of the low-power phase of a 100%-50%-100% power load-follow transient was varied between 6 hours and 24 hours in cases 6 to 10. The 4 transients were repeated with and without any control rod movements, to quantify the effects of the moving rods on the xenon stability. It was found that the duration of the low-power phase of a load-follow transient does not influence the xenon-induced power oscillation damping stability of the current 400 MW PBMR core to any significant degree.

This result was expected from the basic xenon stability theory, since the xenon stability properties of the PBMR core is not influenced by the amplitude of the initial xenon/flux perturbation, but rather by operational and design factors such as the operating power level, the core height and the temperature feedback coefficient of reactivity (see Section 2.2 for more detail).

2. For the second sensitivity study, the final power level of four open-ended load-follows was varied between 300 MW and 700 MW. The transients in Section 6.2 were all calculated with stationary control rods, to enable comparison of the inherent xenon stability for various power levels between cases 1 to 4 (Chapter 4) and cases 11 to 14. It was found that an increase in the final power level of a load-follow transient results in a decrease in the damping stability of xenon-induced power oscillations. This observation was also made in Section 4.2.4, and the two relationships determined in these sections between the inherent xenon damping ratio and the power level were compared. Although the value of the damping ratio derivative with power, as calculated in Section 6.2 at 400 MW, differs significantly (57%) from the value calculated in Section 4.2.4, the differences were expected due to the different nature of the two transient sets. When the actual damping ratio vs. power behaviour was analysed for the two types of xenon perturbation transients used in Chapters 4 and 6, by using the derived least-squares fit expressions in Sections 4.2.4 and 6.2, less than 10% difference existed between the two data sets. This finding confirmed that the inherent xenon stability of the core is largely independent of the nature of the xenon/flux perturbation.

The determination of the 400 MW PBMR xenon-induced power oscillation stability was performed in Chapters 4-6. In Chapter 7, a sensitivity study is presented on variances in four of the main contributors to the PBMR xenon stability. The purpose of Chapter 7 is to determine the main reason, or reasons, for the PBMR's high degree of axial xenon stability.

CHAPTER 7

7. SENSITIVITY STUDY ON FOUR PARAMETERS INFLUENCING PBMR AXIAL XENON STABILITY

7.1 INTRODUCTION

It has been shown in Chapters 4 to 6 that the current PBMR core design exhibits well-damped xenon-induced axial power oscillations. In this chapter four important contributors to this high level of axial xenon oscillation stability are investigated in more detail. Some of these variations result in non-physical PBMR cores (e.g. Cases 22 to 24, where the default core isotopics have been artificially permutated to obtain a flatter axial power profile), but some useful observations can still be made from these "theoretical" cases. As discussed in Section 2.2, Stacey [1] concluded that for various reactor types the xenon-induced power oscillation damping stability decreases with:

1. An increase in core size.
2. An increase in the thermal neutron flux levels (i.e. power).
3. An increase in the "flatness" of the thermal flux distribution (i.e. a reduction in the dimensional power peaking factors).
4. A decrease in the magnitude of the total temperature reactivity coefficient.

It was also stated that although the PBMR core is quite tall; the core-averaged power density at 400 MW thermal power is quite low, the axial power profile is peaked towards the top of the core, and that the current design exhibits a negative total temperature reactivity coefficient. In this section the main reasons for this overall stable oscillation behaviour are identified by selectively adjusting the four parameters indicated above; either as individual variations on the default 400 MW PBMR design, or in combination with other parameters.

In order to compare the stability results for cases 15 to 24 with the inherent damping stability data for case 1 in Chapter 4, the same modelling approach as utilised in Section 4.2 is followed here. A relative control rod insertion depth to half of the active core height was specified for a period of four hours to excite strong spatial disturbances in the neutron flux and xenon concentration fields in the top part of the core. The control rods are returned to their nominal location after this period. No other control rod movements are performed for the remainder of the transients. Due to limitations on available space, only the power density oscillation stability results for these nine transient cases will be compared with the case 1 results, and very limited tabular or graphical data will be shown in this section. The detailed data set is discussed in the PBMR report on this topic [25].

7.2 CORE AXIAL HEIGHT INCREASED TO 20 M, 30 M AND 40 M

It was discussed in Section 2.2 that an increase in the reactor dimensions would lead to smaller values of $\mu_n^2 M^2$ (see Eq. 2.3), which implies a nearly quadratic reduction of the damping stability with an increase in the core size. Therefore, in principle it should be possible to find a PBMR core height that produces diverging axial xenon oscillations, regardless of the stabilising effects of the other contributing parameters. For Cases 15 to 17, the core axial height is increased from the nominal ~ 11 m to 20 m, 30 m and 40 m, respectively. In order to keep the average power density similar to the nominal value of ~ 5 MW/m^3, the total core power generation in these three cases is increased to 800 MW, 1200 MW and 1600 MW, and the control rods are adjusted to the same relative height, in order to isolate the effect of the increased core height. Table 7-1 indicates the changes in control rod locations for these three cases.

Table 7-1: Control rod movements for cases 15 to 17

Case #	Power level (MW) and core height (m)	Control rod location (m) at t = 0 h, and from 5-72 h	Control rod location (m) from 1-5 h
15	800 MW / 20 m	4	10
16	1200 MW / 30 m	6	15
17	1600 MW / 40 m	8	20

The normalised power density oscillations for cases 15 to 17 are presented in Figure 7-1 to Figure 7-3. Note that least-square fit data were only determined for case 15 and case 16 (the reason for this is explained in the next paragraph). Since the power normalisation is performed to different steady-state power levels for the three cases (800 MW, 1200 MW and 1600 MW), the amplitudes of the oscillations cannot be directly compared with each other. However, it is apparent that the magnitudes and degree of damping of the three cases differ significantly, with a clear trend of less damped power oscillations with an increase in core height. This observation is confirmed by the quantitative data for case 15 and case 16, as shown in Table 7-2, where the oscillation stability parameters of these two cases are compared with the data for case 1 (i.e. the nominal 400 MW 11 m high core).

Case 17 (the 40 m high PBMR core variant) exhibits power density oscillations that are very close to diverging, or possibly slightly un-damped. This implies that the damping constant b is close to zero or negative, and the amplitude peak-to-peak ratio close to one, or possibly larger than one. This can be seen in Figure 7-3 if the amplitudes of the power density oscillation at the location z = 250 cm is compared at the time points t = 22 h and t = 62 h. The oscillation magnitude difference between the top and bottom of the core is also very noticeable in this figure: the power density peak at z = 850 cm and t = 46 h is 5.5 times higher than its steady-state value, while the peak at z = 250 cm and t = 62 h is "only" twice as high as its steady-state value.

Since the power oscillations in case 17 are not of a pure exponential-sinusoidal nature (note the distorted power density variations between t = 36 h and t = 56 h), the fitting routine based on Eq. (2.7)

$$N_{x_i}(t) = N_{x_i}(t_0)e^{ht}\sin(Ct + D) + E \qquad (2.7)$$

cannot be applied to the data for case 17 with an acceptable level of accuracy. Quantitative data on the nature of the case 17 axial power oscillations were therefore not determined, but it are included in this section as an example of a highly unstable core with respect to xenon-induced power oscillations.

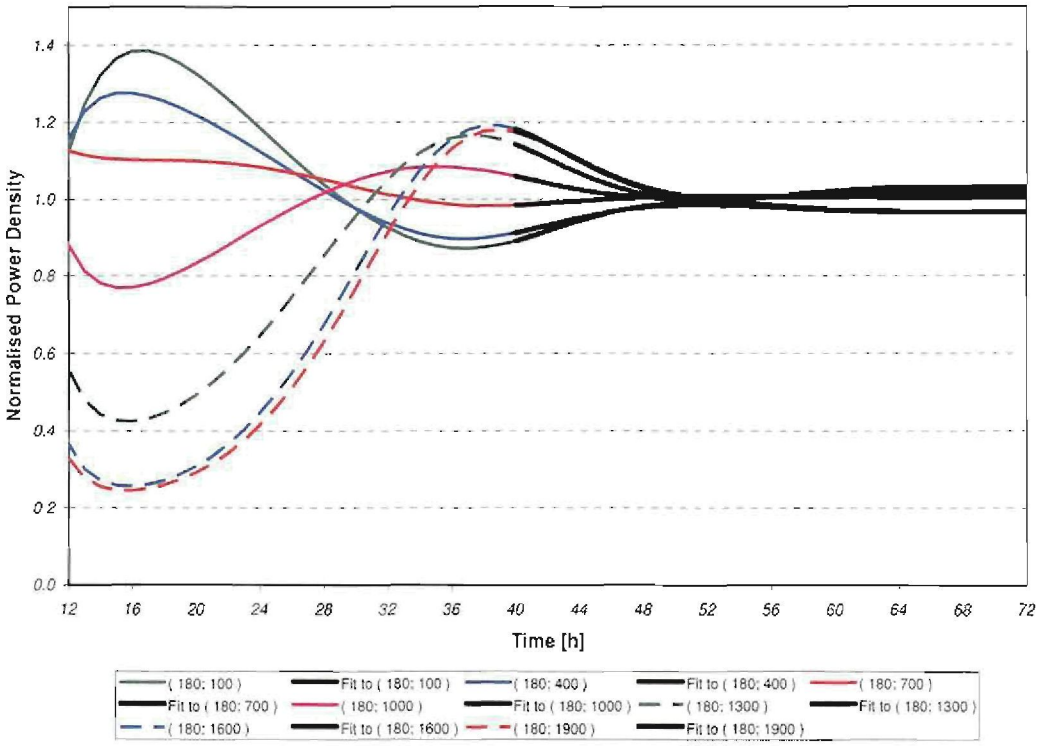

Figure 7-1: Case 15 (20 m core) normalised axial power density at 7 axial locations along r = 180 cm

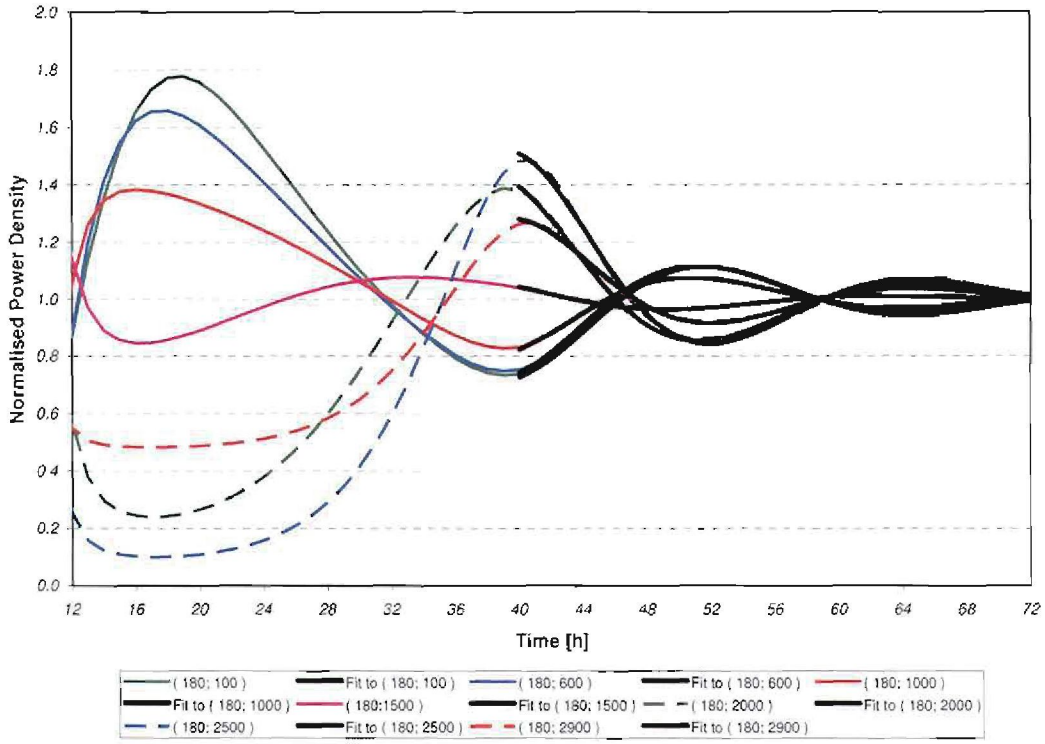

Figure 7-2: Case 16 (30 m core) normalised axial power density at 7 axial locations along r = 180 cm

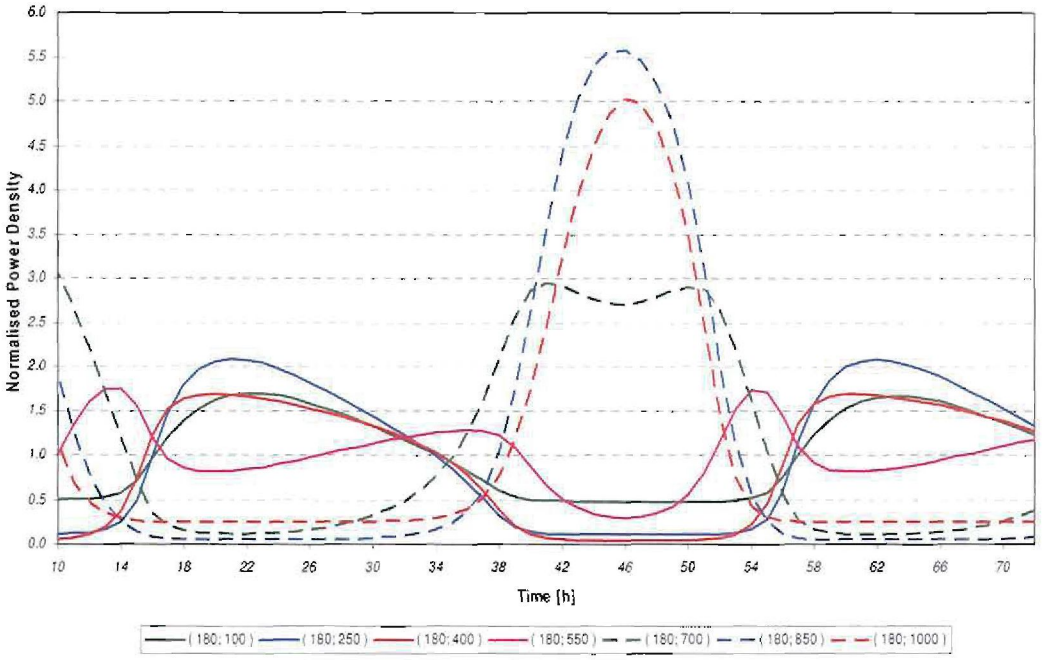

Figure 7-3: Case 17 (40 m core) normalised axial power density at 6 axial locations along r = 180 cm

Table 7-2: Cases 1 and 15-17 power density oscillation damping data

Case	Damping constant *b*	Damping ratio ξ	Damped period T_D (h)	Quality	Notes
Case 1: 10 m core	0.14	0.53	49	-	Nodes at 400 cm and 550 cm excluded.
Case 15: 20 m core	0.12	0.24	30	0.003	Node at 1000 cm excluded.
Case 16: 30 m core	0.08	0.09	26	0.34	Node at 1500 cm excluded.

The variation of the power density oscillation damping ratio with the core axial height is presented in Figure 7-4, together with a second order polynomial fit line. The dependency of the damping ratio ξ on the core height H within the range 10 m - 30 m is given by the fit expression

$$\xi = 0.00103\,H^2 - 0.0632\,H + 1.075 \qquad (7.1)$$

with a R^2 value of 0.99999. This implies that an increase of 5 m in the core height from 10 m to 15 m would result in a 34% decrease of the power density oscillation damping stability from, 0.53 to 0.35. In principle, Eq. (7.1) can be solved to find the predicted core height $H_{critical}$ that corresponds to the transition point between converging and diverging oscillations by setting $\xi = 0$ in the expression. However, it is found that Eq. (7.1) reaches a minimum value of ~ 0.11 around 30 m, and thereafter increases again. Therefore it has no real $H_{critical}$ values that correspond to zero ξ values.

If it is kept in mind that the determination of the oscillation exponential-sinusoidal parameters is based on linear perturbation theory, the approach followed in this study will not be able to determine quantitative data for the highly unstable non-linear cores, of which case 17 is an example. If "cleaner" (i.e. linear, pure exponential-sinusoidal and with small initial amplitudes) power oscillations could have been obtained, the fitting routine would have be able to calculate negative values for the damping constant *b*, but unfortunately the 40 m high PBMR core does not exhibit low amplitude linear behaviour. The use of the Eq. (7.1) is therefore restricted to core height values between 10 m and 30 m.

The derivative of the damping ratio with the power level can be determined from Eq (7.1) as

$$d\xi / dH = 0.00206\,H - 0.0632 \qquad (7.2)$$

This leads to a $d\xi / dH$ value of -0.043 m^{-1} for the current PBMR equilibrium core design at the nominal core height of 10 m. This ratio essentially represents the gradient of the damping ratio vs. core height fit at this core height, and it can be used to assess the magnitude of a change in the xenon stability with a variation in the core height around this point.

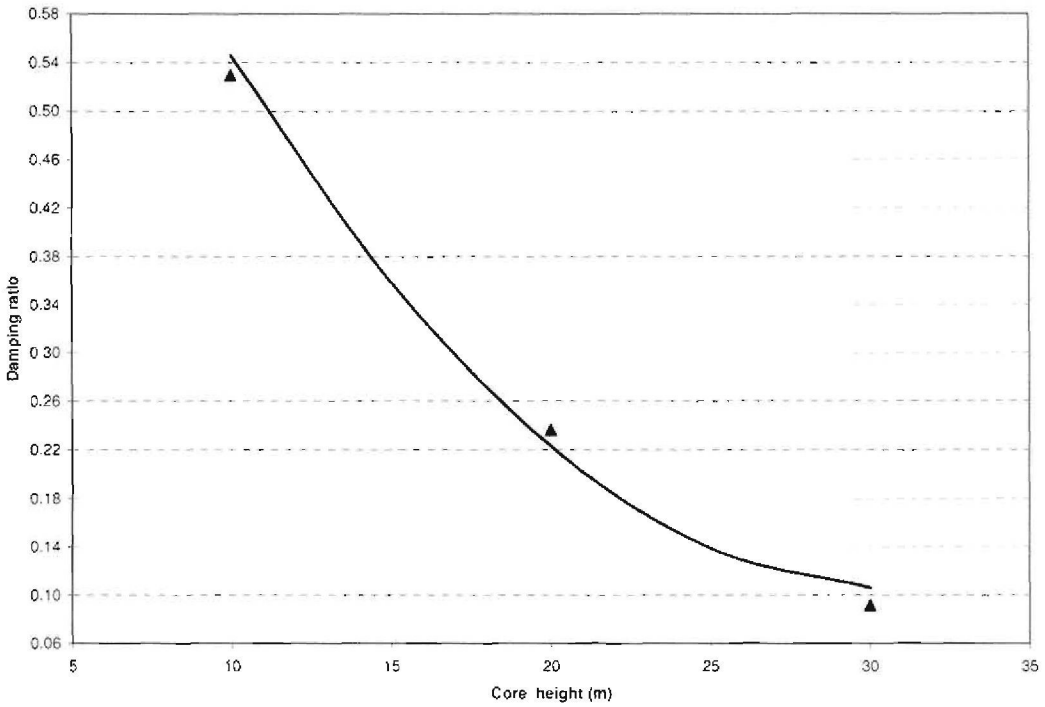

Figure 7-4: Variation of power damping ratio with core axial height (m): calculated data points and fitted polynomial trend line

In conclusion, the following remarks can be made on the work performed in this section:

1. An increase in the active core height leads to a significant decrease in the xenon-induced power oscillation damping stability.
2. Although the exact transition core height $H_{critical}$ could not be determined mathematically due to the non-linearity of the power oscillations in the 40 m high PBMR core, the TINTE power oscillation data clearly show the transition from damped to undamped behaviour between the 30 m (Cases 16) and 40 m (case 17) high PBMR cores. The inherent xenon stability margin in the current PBMR core in respect to the active core height is therefore substantial, since stable xenon and power oscillatory behaviour can be expected for this type of core design up to an active core height of 30 m operating at a total power output of 1200 MW, if all other core and fuel design parameters remain constant.

7.3 TOTAL POWER VARIATIONS FROM 200 MW - 800 MW

In Section 4.2.4 and Section 6.2 it was determined that the power density oscillation damping stability depends non-linearly on the steady-state power levels and the final power level after a load-follow manoeuvre, respectively. It was quantitatively confirmed that a decrease in stability occurs with an increase in the power levels. This section provides final confirmation of this general trend. The four transient cases consist of repeating the basic case 1 control rod insertion scenario at four fixed steady-state power levels: 200 MW, 400 MW, 600 MW and 800 MW.

Since this scope is essentially similar to the work reported in Chapter 4, an additional element is added in this section by minimising the effect on the damping stability data of the increase in fuel and moderator temperatures as the power levels increase. This is obtained by reducing the absolute fuel and moderator temperatures to values where the overall reactivity coefficient of temperature is smaller. Cases 18 to 21 therefore utilise very high mass flow rates through the core to obtain lower fuel and moderator temperatures over the entire core, and reactor outlet temperatures (ROTs) of only 600°C, i.e. gas temperature increases of only 100°C. The total reactor power is increased from 200 MW (case 18) to 400 MW (case 19), 600 MW (case 20) and 800 MW (case 21), and a comparison is then made between the power damping stability of these cases and the 400 MW and 200 MW PBMR cores operating at ROTs of 900°C (Cases 1 and 3). The control rods are maintained at the nominal 400 MW insertion depth of 202 cm for all four cases.

This comparison essentially quantifies the role of the fuel and moderator temperature feedback in the power oscillation damping stability at 200 MW and 400 MW power. A general xenon oscillation stability criterion was discussed in Section 2.2:

$$\mu_n^2 M^2 - \beta_T \bar{\phi}_0 + \rho_X^{\infty} \cdot \left\{ \sigma\bar{\phi}_0 \cdot \left[\frac{1}{1 + \frac{\lambda_x}{\sigma\bar{\phi}_0}} - \gamma_X \right] / (\lambda_x + \lambda_i + \sigma\bar{\phi}) \right\} > 0 \qquad (2.5)$$

(Here, β_T is the total reactivity coefficient and $\bar{\phi}_0$ the average steady-state flux). The second term in Eq. (2.5) describes the stabilising effect of the fuel and moderator temperature feedback on spatial flux, and it can be seen that a larger negative total reactivity coefficient β results in more strongly damped xenon oscillations. In practice, β is a dynamic parameter that changes continuously with variations in the fuel, moderator and reflector temperatures. Figure 7-5 shows that the total temperature reactivity coefficient becomes more negative at higher temperatures, which will therefore tend to increase the stability of xenon-induced power oscillations. By changing the magnitude of this coefficient, its effect on axial xenon stability could be investigated. Note that the total temperature reactivity coefficient consists of complex contributions from the decreasing negative fuel coefficient and the increasing negative moderator coefficient, for an increase in the respective temperatures.

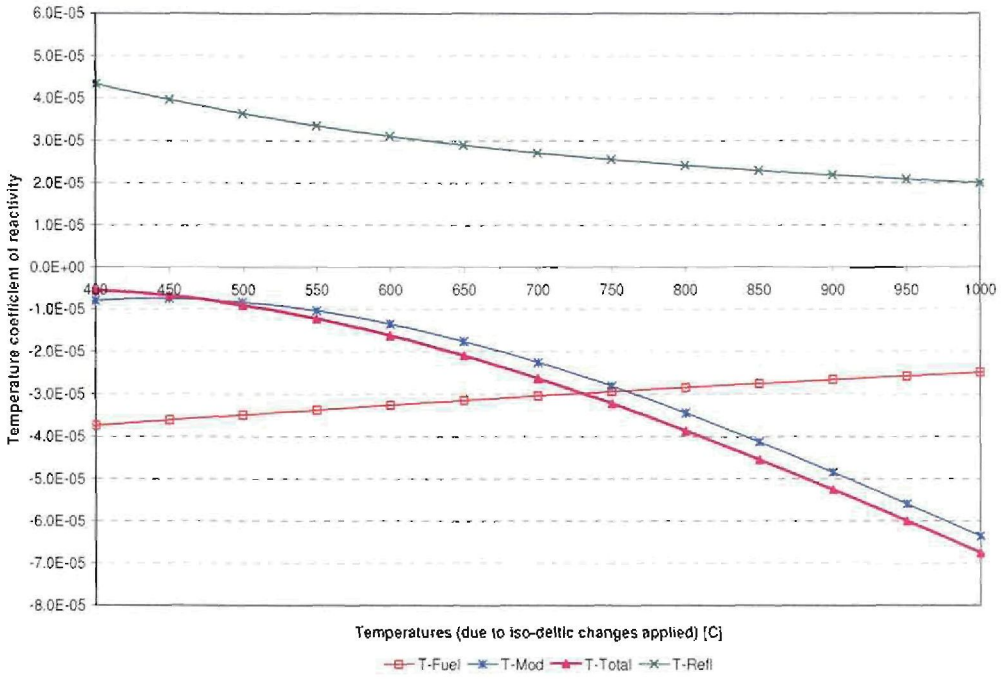

Figure 7-5: Variations in the PBMR fuel, moderator, reflector and total temperature coefficients of reactivity with isodeltic changes in temperatures

The quantitative power density damping ratio data for these four cases is summarised in Table 7-3, where the decrease in power density oscillation damping stability with an increase in the power levels, can be clearly observed.

The variation of the power density-damping ratio ξ with the steady-state power level is presented in Figure 7-6. A third-order polynomial fit line is also shown in relation to the source data points. The dependency of the damping ratio ξ on the power level P is given by the fit expression

$$\xi = -(8.0\text{x}10^{-10})P^3 + (1.72\text{x}10^{-06})P^2 - (0.0013)P + 0.6762 \qquad (7.3)$$

with a R^2 value of 0.9999.

The derivative of the damping ratio with the power level can be determined from Eq (7.3) as

$$\frac{d\xi}{dP} = -(2.40\text{x}10^{-09})P^2 + (3.44\text{x}10^{-06})P + 0.0013 \qquad (7.4)$$

Table 7-3: Power density damping ratio ξ for cases 18 to 21

Coordinate	Case and power level (MW)			
	18 (200 MW)	19 (400 MW)	20 (600 MW)	21 (800 MW)
(140; 100)	0.48	0.38	0.34	0.33
(140; 250)	0.48	0.39	0.35	0.33
(140; 400)	*0.49*	*0.39*	*0.35*	*0.32*
(140; 550)	*0.38*	*0.26*	*0.25*	*0.25*
(140; 700)	0.48	0.38	0.35	0.33
(140; 850)	0.48	0.38	0.34	0.32
(140; 1000)	0.49	0.39	0.34	0.32
(105; 100)	0.48	0.38	0.34	0.33
(105; 250)	0.48	0.38	0.35	0.33
(105; 400)	*0.49*	*0.39*	*0.35*	*0.32*
(105; 550)	*0.38*	*0.27*	*0.25*	*0.26*
(105; 700)	0.48	0.38	0.35	0.33
(105; 850)	0.48	0.38	0.34	0.32
(105; 1000)	0.49	0.39	0.34	0.32
(180; 100)	0.48	0.38	0.34	0.33
(180; 250)	0.48	0.39	0.35	0.33
(180; 400)	*0.49*	*0.39*	*0.35*	*0.32*
(180; 550)	*0.39*	*0.27*	*0.25*	*0.26*
(180; 700)	0.48	0.38	0.35	0.33
(180; 850)	0.48	0.38	0.34	0.32
(180; 1000)	0.49	0.39	0.34	0.32
average	**0.48**	**0.38**	**0.34**	**0.32**

If the derivative in Eq. (7.4) is compared with the derivative determined for variations in the low power variations at the nominal power level of 400 MW (Cases 1-4, Eq. (4.4) in Section 4.2.4), a value of -3.08×10^{-04} is obtained vs. -3.12×10^{-04} for Eq (4.4). The independence of this derivative on the temperature differences that exists between the Cases 1-4 data (based on a ROT of 900°C) and the Cases 18-21 data (ROT 600°C) should be noted, even if the damping ratio data itself differs significantly between the two sets (see Table 7-4).

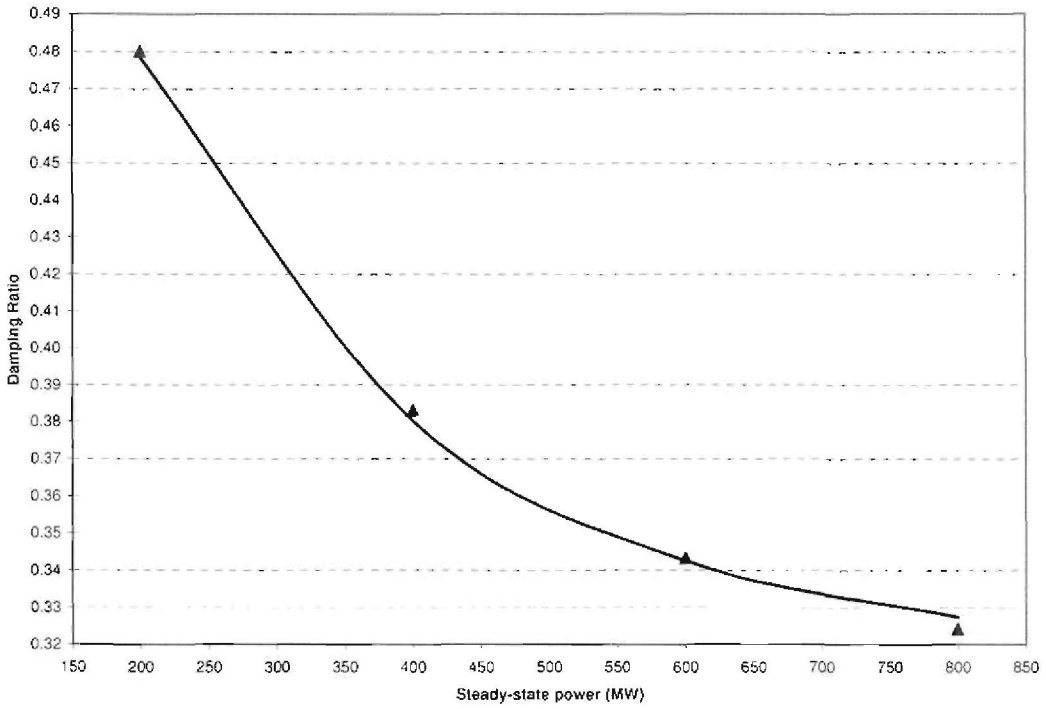

Figure 7-6: Variation of the power damping ratio with the steady-state power level for cases 18 to 21: calculated data points and fitted polynomial trend line

It is shown in Table 7-4 that the lower ROT cases (case 18 and case 19) exhibit weaker damped power oscillations compared to the 900°C ROT case 1 and case 3, which confirms the stabilising effect of a more negative temperature feedback coefficient at increased fuel and moderator temperatures.

Table 7-4: Comparison of the average power density-damping ratio ξ for cases 1, 3, 18 and 19

Case 18 (200 MW, ROT 600C)	Case 3 (200 MW, ROT 900C))	Case 19 (400 MW, ROT 600C)	Case 1 (400 MW, ROT 900C)
0.48	0.60	0.38	0.53

An important conclusion can be drawn from the findings in this section: although an increase in total power levels would lead to a decrease in stability on its own, this power increase is usually accompanied in operating cores by increases in the fuel and moderator temperatures as well. These two effects work against each other in terms of xenon-damping stability, and the increase of the total temperature coefficient of reactivity (more negative) with increased temperatures in Figure 7-5, could be one of the main reasons for the gradual decrease in the gradient of the power-damping ratio (Figure 7-6).

In fact, Stacey [17] notes that an increase in the power levels could actually lead to an increase in stability for certain core designs, depending partly on the magnitude of the total temperature reactivity coefficient.

The findings of this section can be summarised as follows:

1. An increase in the steady-state power level leads to a decrease in the xenon-induced power oscillation damping stability.
2. The current PBMR core can be operated at total power levels up to 800 MW and still exhibit well-damped power oscillations. This is partly due to the increase in fuel and moderator temperatures that occur during operation at these higher power levels, which lead to an increase in the (negative) magnitude of the total temperature reactivity coefficient. This enhanced reactivity feedback partly offsets the destabilising xenon-damping effect of the increased power levels, and it forms one of the main inherent stabilising mechanisms in the PBMR core design. (It should be stressed that this conclusion is not "overcome", but "offset"; i.e. a net reduction in the damping stability still occurs with a rise in power levels, but at a reduced rate, due to the countering effect of the increase in the moderator and fuel temperature feedback coefficient).

7.4 CASES 22 TO 24: FLATTER AXIAL POWER SHAPES FOR THE 400 MW, 800 MW AND 15 METER CORES

In this section three transient cases are defined to investigate the effect of flattening the axial power profiles of the nominal core on the power damping stability. Section 2.2 indicated a general observation from the work of Lauer [16] that the eigenvalues μ^2 become smaller as the steady-state flux profile $\bar{\phi}_0$ becomes flatter, indicating that reactor designs with a flattened flux profile would tend to be less stable. The "flatter" axial power profiles are obtained by manipulating the spatial nuclear material regions in the TINTE model in a unphysical manner.

The detailed composition of the nominal and permutated core isotopic material meshes is shown in Table 7-5. Each isotopic material number refers to a set of isotopic number densities, obtained from the VSOP99 code. The nominal material mesh pattern is directly related to the PBMR fuel loading scheme, flux and temperature and burn-up profiles, while the permutated core simply uses these material meshes in a arbitrary pattern designed to obtain as flat as possible axial power profile. The permutated core does not represent any possible physical or operational configuration of the current PBMR core design. The changes to the nominal isotopic pattern can be summarised as follows:

- Only the top third of the core material regions (#1-9 in the first column) is used.
- The top third of the core remains identical to the nominal isotopic material pattern, but the bottom third "packed" in an inverse loading pattern to obtain fresher fuel at the bottom of the core.

- The centre of the core consists of only the 9th material region, repeated for 400 cm (8 rows of 50 cm each).

Table 7-5: Nominal and permutated "flatter axial profile" PBMR 400 MW core isotopic material compositions

1	25	49	73	97	121
2	26	50	74	98	122
3	27	51	75	99	123
4	28	52	76	100	124
5	29	53	77	101	125
6	30	54	78	102	126
7	31	55	79	103	127
8	32	56	80	104	128
9	33	57	81	105	129
10	34	58	82	106	130
11	35	59	83	107	131
12	36	60	84	108	132
13	37	61	85	109	133
14	38	62	86	110	134
15	39	63	87	111	135
16	40	64	88	112	136
17	41	65	89	113	137
18	42	66	90	114	138
19	43	67	91	115	139
20	44	68	92	116	140
21	45	69	93	117	141
22	46	70	94	118	142
23	47	71	95	119	143
24	48	72	96	120	144

1	25	49	73	97	121
2	26	50	74	98	122
3	27	51	75	99	123
4	28	52	76	100	124
5	29	53	77	101	125
6	30	54	78	102	126
7	31	55	79	103	127
8	32	56	80	104	128
9	33	57	81	105	129
9	33	57	81	105	129
9	33	57	81	105	129
9	33	57	81	105	129
9	33	57	81	105	129
9	33	57	81	105	129
9	33	57	81	105	129
9	33	57	81	105	129
9	33	57	81	105	129
8	32	56	80	104	128
7	31	55	79	103	127
6	30	54	78	102	126
5	29	53	77	101	125
4	28	52	76	100	124
3	27	51	75	99	123
2	26	50	74	98	122
1	25	49	73	97	121

The three cases are:

- Case 22: A PBMR core operating at 400 MW and with all other parameters at nominal values, except for the flatter axial power profile.
- Case 23: A flatter axial power profile version of case 21, i.e. a PBMR core operating at 800 MW and 600°C ROT.
- Case 24: A flatter axial power profile PBMR core operating at 600 MW and with a core height of 15 m. (The reason for selecting a core height of 15 m instead of 20 m will be explained shortly).

A comparison between the axial power profiles of the two 400 MW cores (case 1 and case 22) is presented in Figure 7-7.

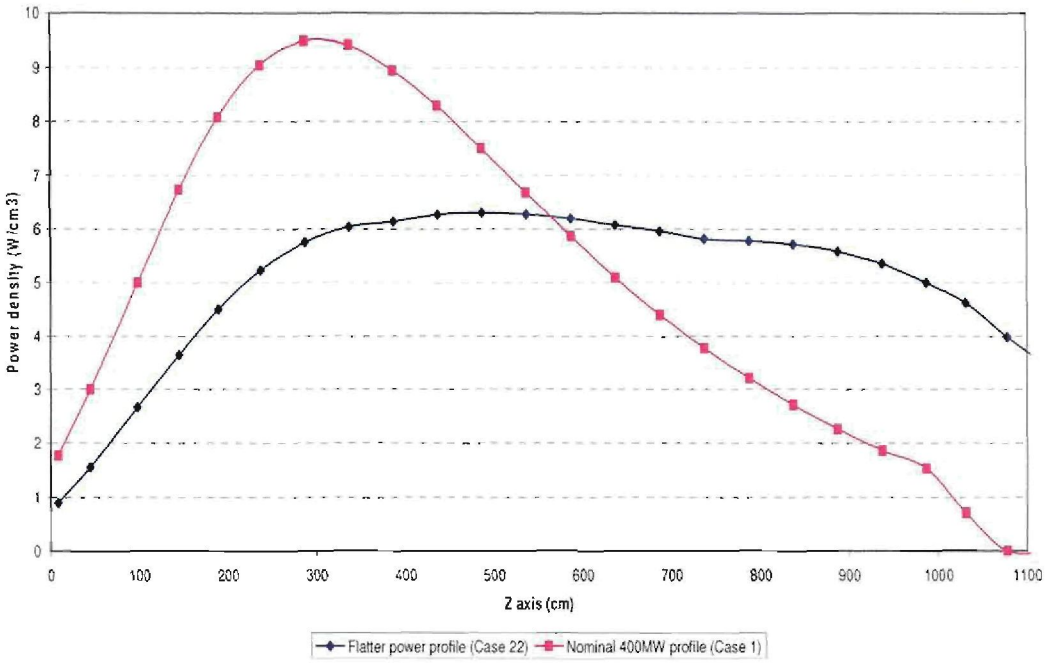

Figure 7-7: Case 1 and case 22 axial power density profiles at r = 105 cm

Due to the core heat-up profile from the top to the bottom, as well as the axial fuel burnup profile, the lower power production in the top part of the core could not be increased significantly, but it is evident that case 22 exhibits a much flatter axial power profile over the rest of the core volume when compared with the nominal 400 MW core (case 1). Similar results were obtained for the 800 MW 600°C ROT cores (cases 21 and case 23).

The normalised power density variations and the least-square fits for Cases 22-24 are presented in Figure 7-8 to Figure 7-10. The time at which the least-square fits were initialised was adjusted between the three cases, since the large initial oscillation amplitudes reached in this section resulted in lower quality fits if the starting points were selected too early in the transients. The starting time points for the cases 22 to 24 were chosen as 12 h, 32 h and 40 h, respectively (it should be noted that several fit iterations starting at various time points were attempted, with no significant variance in the damping ratio results, but with large increases in the fit quality).

The initial intention was to compare case 24 with case 15 (i.e. two 20 m high cores), but it has been found that the 20 m "flat profile" core is very unstable against spatial flux and xenon perturbations. The diverging power density oscillations for the 20 m flat power profile core are shown in Figure 7-11, and since the time-dependent variations of the power density are non-linear and non-sinusoidal due to distortions caused by the interference from higher oscillations modes, no attempt was made to determine least-square fitting data for this case.

The core height was then decreased to 15 m (Figure 7-10), which led to a more unstable core than the 20 m high nominal core. However, the stability of the 15 m flat profile core still remained within the damped oscillation domain. Figure 7-11 can be visually compared with Figure 7-10 to see the difference in the degree of damping.

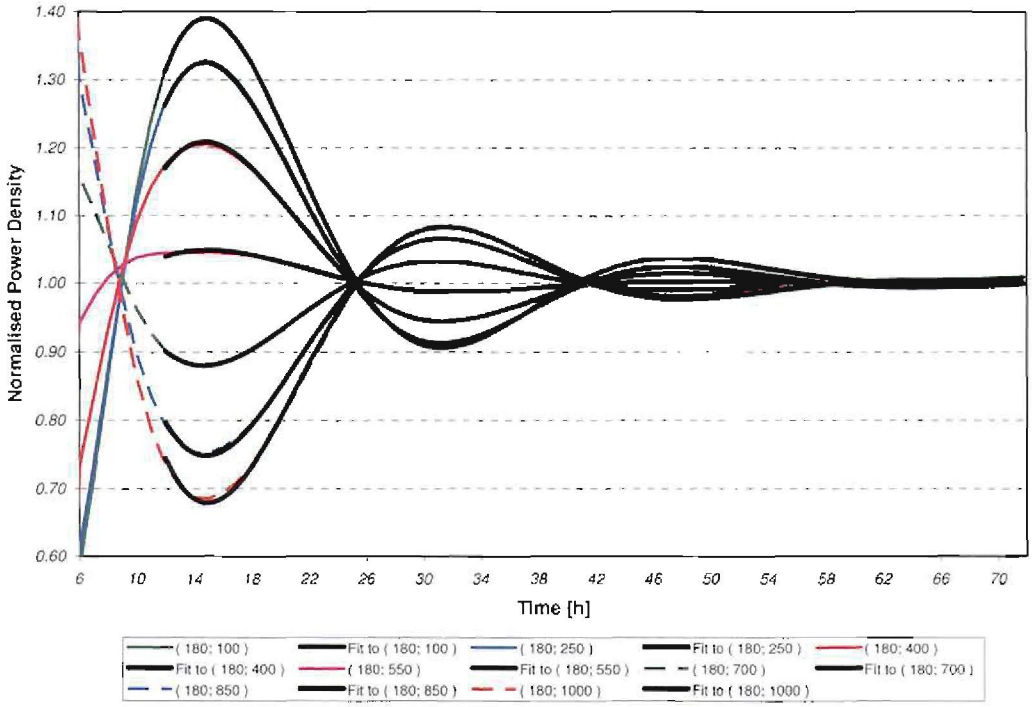

Figure 7-8: Case 22 (400 MW "flat power" core) normalised axial power density at 7 axial locations along r = 180 cm

A visual comparison of Figure 4-4 with Figure 7-8 (case 1 vs. case 22) clearly shows that the power density oscillations for case 22 are less damped than its nominal core counterpart. The relatively peaked PBMR axial power profile therefore is therefore one of the main stabilising mechanisms in respect of xenon-induced power oscillations.

Unlike the quantification of the relationships between the damping stability and increases in height and power (Section 7.2 and Section 7.3), it unfortunately is very difficult to quantify the destabilising effect of an increasing "flatness" of the axial power profile. It might be possible to mathematically relate the axial power peaking factor to the power damping ratio, but since the axial power shape may be peaked at the bottom or the top of the core and still exhibit the same absolute peaking factor, a unique damping ratio for a specific axial power peaking factor may not be easily determined.

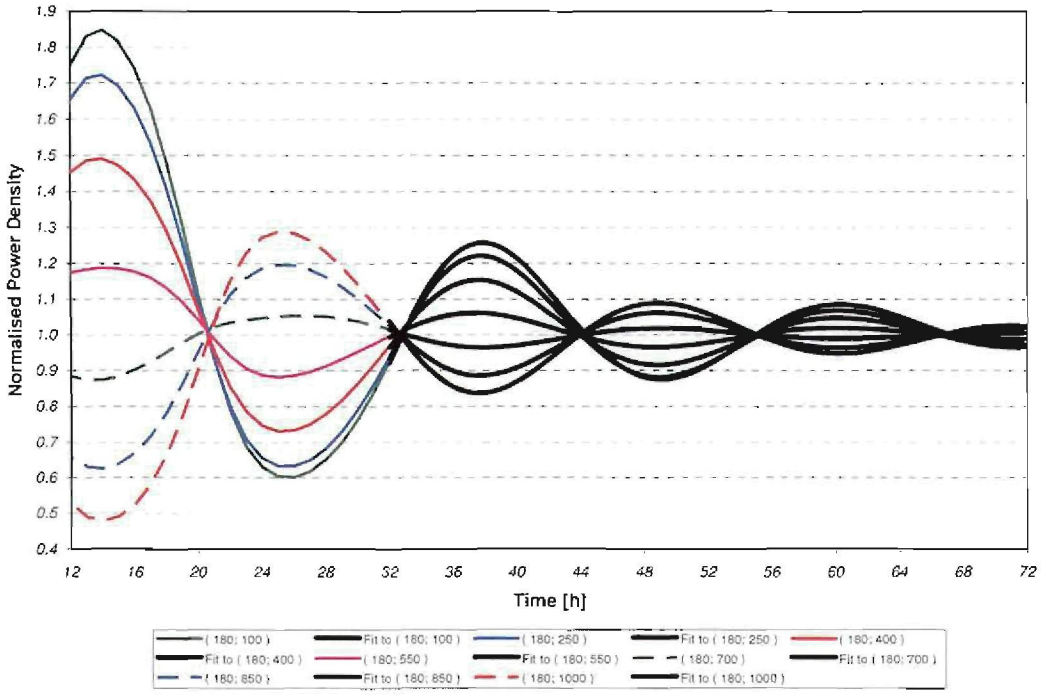

Figure 7-9: Case 23 (800 MW 600°C ROT "flat power" core) normalised axial power density at 7 axial locations along r = 180 cm

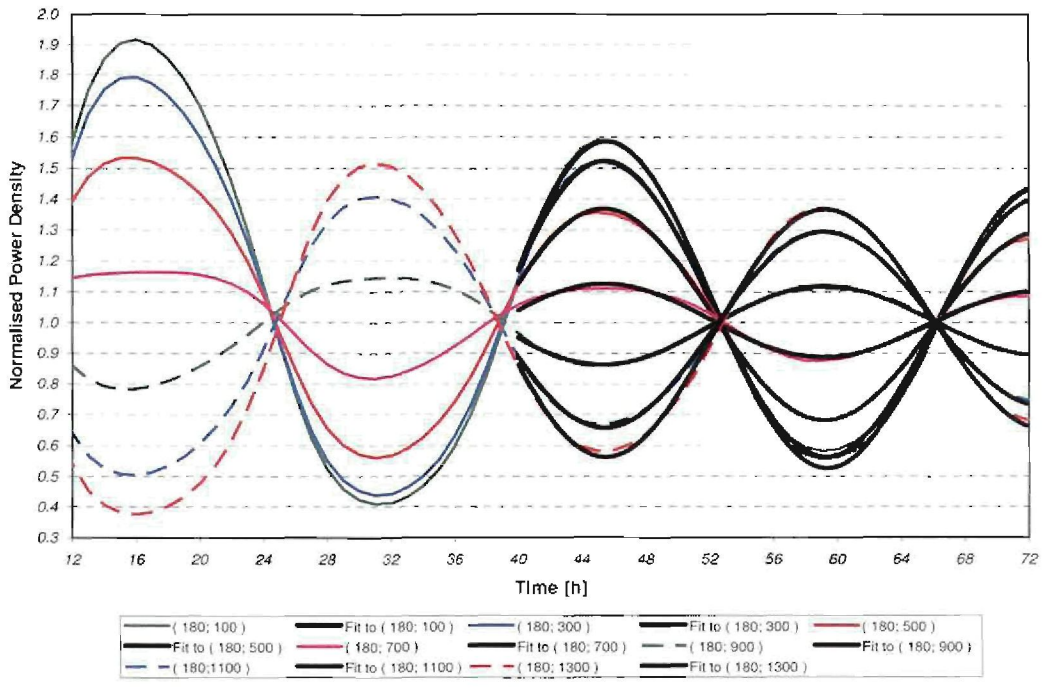

Figure 7-10: Case 24 (15 m high "flat power" core) normalised axial power density at 7 axial locations along r = 180 cm

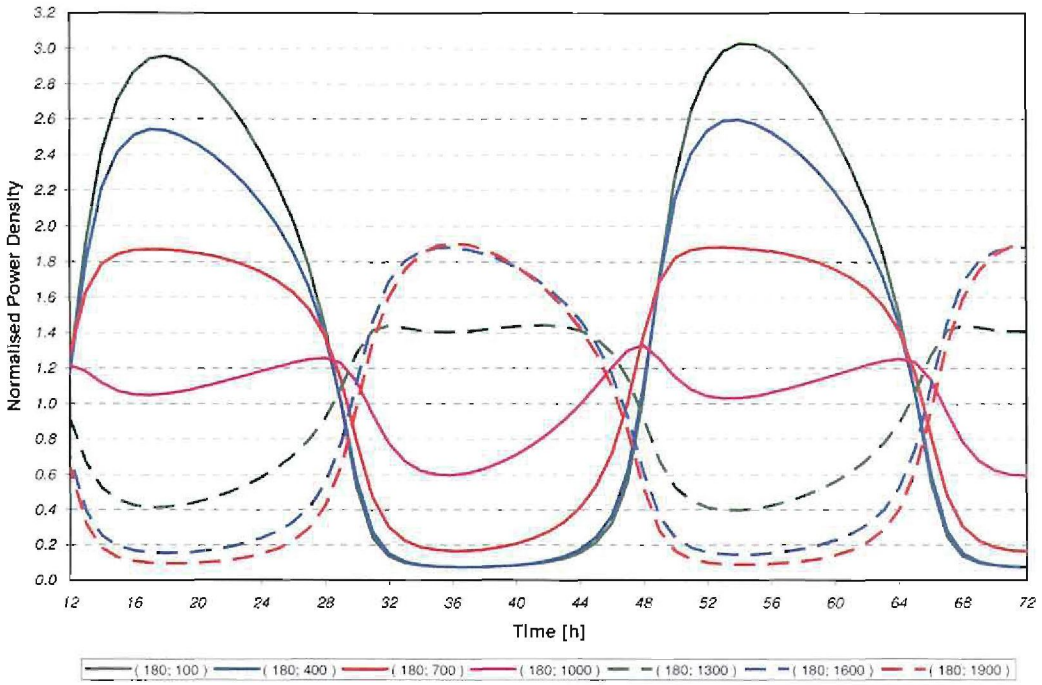

Figure 7-11: 20 m high "flat power" core: normalised axial power density at 7 axial locations along r = 180 cm

The quantitative power damping ratio comparisons between cases 1 and cases 21 to 23 are presented in Table 7-6.

Table 7-6: Comparison of the power density damping ratio ξ between case 1 and cases 21 to 23

Coordinate	Damping ratio ξ			
	Case 1 (400 MW nominal)	Case 22 (400 MW flat)	Case 21 (800 MW 600C ROT nominal)	Case 23 (800 MW 600C ROT flat)
(105; 100)	0.53	0.15	0.33	0.03
(105; 250)	0.53	0.15	0.33	0.03
(105; 400)	*0.52*	*0.15*	*0.32*	*0.03*
(105; 550)	*0.50*	*0.17*	*0.26*	*0.03*
(105; 700)	0.52	0.15	0.33	0.04
(105; 850)	0.52	0.15	0.32	0.03
(105; 1000)	0.53	0.15	0.32	0.03
(180; 100)	0.53	0.15	0.33	0.03
(180; 250)	0.54	0.15	0.33	0.03
(180; 400)	*0.52*	*0.15*	*0.32*	*0.03*
(180; 550)	*0.50*	*0.17*	*0.26*	*0.03*
(180; 700)	0.52	0.15	0.33	0.04
(180; 850)	0.52	0.15	0.32	0.03
(180; 1000)	0.53	0.15	0.32	0.03
average	**0.53**	**0.15**	**0.32**	**0.03**

A reduction in the average power damping ratio from 0.53 to 0.15 is obtained for the two 400 MW cases 1 and 22, while a very low average power damping ratio of 0.03 is calculated for case 23 (800 MW 600°C ROT).

The average power density damping ratios for the "flat power" 15 m high core and the nominal 20 m high core are shown in Table 7-7. The average power damping ratio for the "flat power" 15 m high core is almost 100 times more unstable than the nominal 20 m high core, but even this very low damping ratio still represents a core with damped power oscillations.

Table 7-7: Comparison of the power density damping ratio ξ between case 15 and case 24

Case 15 (20 m height nominal)		Case 24 (15 m height flat)	
Coordinate	**Damping ratio ξ**	**Coordinate**	**Damping ratio ξ**
(105; 100)	0.20	(105; 100)	0.0021
(105; 400)	0.20	(105; 300)	0.0023
(105; 700)	0.27	(105; 500)	0.0028
(105; 1000)	*0.19*	*(105; 700)*	*0.0043*
(105; 1300)	0.23	(105; 900)	0.0020
(105; 1600)	0.25	(105; 1100)	0.0028
(105; 1900)	0.26	(105; 1300)	0.0028
(180; 100)	0.20	(180; 100)	0.0020
(180; 400)	0.20	(180; 300)	0.0023
(180; 700)	0.27	(180; 500)	0.0028
(180; 1000)	*0.19*	*(180; 700)*	*0.0043*
(180; 1300)	0.23	(180; 900)	0.0020
(180; 1600)	0.25	(180; 1100)	0.0028
(180; 1900)	0.26	(180; 1300)	0.0028
average	**0.23**	**average**	**0.0025**

The findings of this section can be summarised as follows:

- An increase in the axial power peaking factor stabilises the PBMR core against xenon-induced axial power oscillations. A quantitative relationship between the axial power peaking factor and the xenon stability was not established, but a flatter axial power profile led to significantly more unstable xenon-induced axial power oscillations.
- This observation was confirmed for the nominal 400 MW core, as well as a 15 m high core operating at 600 MW, and an 800 MW core operating at a reactor outlet temperature of 600°C.

7.5 SUMMARY

The results from the studies performed in this chapter can be summarised as follows:

1. The effect of variances in four reactor design parameters on the PBMR xenon-induced power density oscillation stability was presented. Increases in the magnitudes of the temperature reactivity coefficient and the axial power peaking factor increased the inherent stability of the PBMR core, while increases in the core axial height and the operating power level decreased the inherent stability.
2. A comparison between the effect of increases in the core height and the power level showed that if the core height is doubled from 10 m to 20 m the resulting decrease in stability from ξ = 0.53 to ξ = 0.23 is more severe than a doubling in power from 400 MW to 800 MW, which resulted in a ξ decrease from 0.38 to 0.32. An increase in the core height is therefore much more destabilising than an increase in the operating power level. This conclusion confirms the general statement in Section 2.3, that a nearly quadratic reduction of the damping stability could be expected with an increase of the core size, but only a linear stability reduction could be expected when the power is increased.
3. Quantitative relationships between the xenon-induced power density oscillation stability and the axial power peaking factor, as well as the magnitude of the temperature reactivity coefficient, were not derived. However, it was shown that a decrease in the axial power peaking factor (i.e. a flatter axial power profile) severely decreased the existing PBMR inherent stability, and that the increase in the magnitude of the temperature reactivity coefficient with temperature acts as a countering stabilising mechanism when operating power levels are increased. These two factors were identified as two of the major contributors to the xenon stability of the current 400 MW PBMR core design.

Chapter 7 presented the final quantitative results of the PBMR axial xenon stability study. In Chapter 8, practical considerations on xenon stability measurements in operational reactors are discussed, as well as selected observations on the application of the findings in Chapters 4-6 with respect to the PBMR flux mapping system.

CHAPTER 8

8. PRACTICAL XENON STABILITY IMPLICATIONS AND RECOMMENDATIONS FOR THE PBMR DESIGN

The discussion in this chapter focuses on the need for implementing the findings of this xenon stability study in the current PBMR core design process. It is by no means the main purpose of this study, nor is it an attempt to prescribe design criteria for a flux-mapping and spatial power control system. The only aim here is to integrate the implications of the xenon stability results obtained in Chapters 4 to 6 into a practical context. The comments made here is based on the literature studied and the positioning and response of detectors in the PBMR were not studied in any way. Such a study would be required to make definite recommendations and determine requirements for the PBMR detector layout.

It is important to note that even if a constant total power is maintained, spatial power oscillations can occur without detection, if adequate flux measurement systems are not in place. It is important therefore to use radial, axial and azimuthal flux measurements to detect changes in the thermal flux profiles. Most of the large, high-powered PWR and BWR designs currently operating in the world follow some level of flux mapping and corrective control rod programmes [9], [28], [29]. Several investigations have also been performed in the past on using ex-core detectors to determine power and flux mapping for HTR cores during power changes, control rod insertions and xenon oscillations [32], [33] and [34].

Even though the current PBMR design exhibits well-damped xenon-induced axial power oscillations, it would be beneficial to have an effective spatial flux mapping system as part of its core instrumentation design. Such a system should be capable of monitoring spatial flux levels with an adequate level of resolution to determine gross, large-scale deviations from the steady-state flux profiles. From literature the following ideal properties can be considered in such a design:

- For axial flux mapping, 5 sets of detectors should be positioned along the axial active height of the core, to detect oscillations between the top and bottom of the core.
- For radial thermal flux mapping, at least 3 sets of detectors should be positioned in the central reflector, along the axial active height of the core. However, this might not be practical, due to the high temperatures in this region. Generally speaking, of the 3 oscillation modes, the radial mode is also the most stable, and should only occur in a highly damped form, if at all, in the PBMR core. The measurement of radial oscillation is therefore of secondary importance.

The investigation of azimuthal xenon oscillations is beyond the scope of this study, and therefore no practical suggestions can be made on this aspect.

It is assumed that the detectors indicated above will be positioned in the side reflector, i.e. ex-core detectors. Several historic studies have investigated the use of fast flux measurements outside the core region to determine power oscillations in HTRs, and this aspect should not pose significant practical complications [32] - [34].

A variable commonly used for tracking first mode changes in the spatial power distribution is the flux or power offset value, which is basically defined as the ratio of the power generated in the top of the core over the total core power generation. This parameter effectively indicates the "shape" of the axial thermal flux profile, for example, which could be peaked towards the top. The question can now be asked, "If a deviation in the thermal flux shape is detected during a load-follow, what should the appropriate reactor control response entail?"

The answer falls within the domain of reactor control and measurement, which is a specialized field in nuclear engineering. The general principle behind power offset control is quite simple: the average measured steady-state power shapes (axial, radial and azimuthal) are used as the reference "shapes" for subsequent transient tracking, and if the deviations from this reference shape are larger than some pre-determined bandwidth, the reactor coolant flow is adjusted, or power is decreased, or the control rods are moved in a specific sequence.

Most power utilities use dedicated software to assist the operator/auto-reactivity control systems with the decision-making process of when to initiate a specific countermeasure that would flatten the shape change, and inhibit the oscillation from continuing [28], [29], [30]. From a control point of view, the PBMR is definitely less susceptible to axial xenon oscillations than other reactor types (e.g. most large CANDU and BWR reactors need *active* intervention control most of the time), and the PBMR fuel is also more robust against temperature changes (catastrophic fuel "cladding" failure caused by xenon-induced power oscillations cannot occur in the PBMR).

A final remark on the conclusions of the sensitivity study presented in Chapter 7 is that typically core designs evolve over time, and the current PBMR design will be no exception. However, the effect of changes in some core design parameters on xenon stability should be kept in mind when later versions of the current PBMR are planned. Chapter 7 has shown that the core height is of no concern with respect to xenon-induced power oscillations, since a very tall core of up to 30m can still be sufficiently damped. In any case, from a practical point of view such a tall core would not be optimal, but still, a large theoretical design margin exists for this parameter.

Of specific importance for the xenon stability of the PBMR core is the axial power peaking factor, or flatness of the axial power profile. Due to the addition of fresh fuel at the top of the core, and the heat-up profile of the core for the helium coolant that enters from the top of the core, the PBMR design will always exhibit a peaked power profile towards the top of the core. However, the addition of burnable poisons or a different control rod design could possibly flatten the current axial power profile, which would lead to a decrease in the current design's xenon stability. Since the effect of a flattening in the axial power profile is therefore so significant in terms of xenon stability, design decisions that could influence this factor in future should be carefully considered.

CHAPTER 9

9. CONCLUSIONS AND RECOMMENDATIONS

9.1 CONCLUSIONS

This study evaluated the stability of the 400 MW_{th} Pebble Bed Modular Reactor (PBMR) core design with respect to axial xenon-induced power oscillations. Since the two-dimensional capabilities of the TINTE code excludes the possibility of modelling azimuthal xenon transients, the study was limited to the axial xenon behaviour of the PBMR equilibrium core, with some minor notes on radial xenon stability. The primary aim of this work was to provide the first quantitative investigation into the degree of inherent axial damping in the PBMR annular core design, as well as the xenon oscillation stability under power load-follow operational conditions.

It was shown that the TINTE code in its current form could be used with sufficient accuracy to model the axial variations that occur in the power density, iodine and xenon concentration levels, as well as the time-dependent feedback that exists between these parameters during load-follow and other operational transient events. The detailed TINTE spatial power density and xenon concentration data were used to quantify the amplitude, period and linear damping properties of xenon-induced axial power oscillations.

The 400 MW_{th} PBMR design includes three major characteristics that enhance its stability with regard to xenon-induced spatial power oscillations:

- The core radial dimensions limit xenon oscillations in the radial direction, since the core annulus radius of 85 cm is only slightly larger than the mean neutron diffusion length in graphite (59 cm). Therefore, the core is tightly coupled spatially in the radial dimension.
- The current design has a large negative temperature coefficient of reactivity, compared to typical values for BWR and PWR core designs [35]. This does not only stabilise the total power against excursions, but also decreases the oscillation propagation in local power density variations.
- The axial power profile is peaked towards the top of the core. It was found in Chapter 7 that a modified PBMR core with a flatter axial power profile produced significantly less-damped axial xenon-induced power oscillations.

Several TINTE transient cases were defined and used to determine the stability of the PBMR design against xenon-induced spatial power oscillations. These calculations lead to the conclusion that the current PBMR 400 MW demonstration unit design is inherently very stable against xenon-induced spatial power oscillations in the axial dimension, and that the design shows an adequate margin to the transition point of instability in this respect. This conclusion fulfils the main objective of this study.

No active xenon oscillation control system is therefore recommended for the PBMR, since the axial oscillations analysed in this study showed an acceptable degree of inherent damping. These conclusions are supported by a more detailed discussion of the main findings for each chapter in the section that follows.

9.1.1 Chapters 4 and 5: Cases 1 to 6

Case 1 and case 5 represented the reference cases for the two types of transients that were investigated. The first of these transient types was a short-time artificial insertion of the control rods at a constant total power to obtain a strong initial axial perturbation in the flux and xenon levels, which were used to analyse inherent stability. The second transient type specified generic power load-follow events, of which the most limiting possibility in the current operational planning is the 100%-40%-100% case. The damping ratio ξ (see Section 2.2, Eq. (2.12)) is used as the defining variable for this PBMR xenon oscillation study, as it indicates the degree of damping for a specific transient, and enables direct comparison between the various cases. Most of the reported results in this study focussed on the damping ratio data for the power density, since this is the variable that most directly influences fuel temperatures, but the damping ratio data were also calculated for the xenon and iodine concentrations, and the fast and thermal flux levels.

It was shown in Section 4.2.4 that the overall power density average damping ratios for cases 1 to 4 (control rod insertions at constant total power levels of 100%, 80%, 50% and 20%, respectively) are 0.53, 0.55, 0.60 and 0.73. There is a clear trend towards an increased inherent damping ratio as the power levels are decreased, with the 20% power case (case 4) showing the strongest damping characteristics. This trend is a qualitative confirmation of the observations made in the literature, as summarised in Section 2.2. The current PBMR equilibrium core operating at the nominal power level of 400 MW can therefore be characterised by a single set of inherent power density stability parameters:

- Damping ratio ξ =0.53
- Damping constant b = 0.14
- Damped period T_D = 49 h

The damping ratio of 0.53 implies that this core state of the current PBMR design exhibits well-damped axial power oscillations.

The main conclusion of this Chapter 5 was based on the observation that the average power density damping ratio for case 6 (0.56) is higher than the value for case 5 (0.48), i.e. that a reduction in the inherent damping stability occurs for a typical power load-follow transient when the control rods are moved to maintain core criticality. Case 5 represents the realistic operational load-follow transient, since a global poison option is not available in the current PBMR design. The data for case 6 were also directly compared with the case 1 data for an assessment of inherent stability, since both transients excluded any control rod movements during the free oscillation phase, but very different xenon excitation mechanisms. The damping ratio value for case 5 (0.48) is slightly lower than the value for case 1 (0.53), and case 5 also exhibits a slightly longer damped period (51 h vs. 49 h). This minor decrease in inherent stability could be caused by a variety of factors. One of these is the fact that for case 1 a strong control rod insertion was used as the perturbation source, while the power level variations in case 5 caused the xenon/power oscillations.

9.1.2 Chapter 6: Cases 7-14

Section 6.1 and 6.2 presented the xenon stability results of eight transients that were utilised in two sensitivity studies on the duration and final power level of selected load-follow cases. The first sensitivity study investigated the effect of the duration of the central phase of a three-phase load-follow, i.e. low power durations of 6 h, 12 h, 18 h and 24 h were specified for cases 7 to10.

The main observation regarding cases 7 to 14 was that the continuous movement of the control rods over an extended period of time during the transients lead to a decrease in the inherent damping stability, i.e. similar to the finding made in Chapter 5. A slight variation (0.42±0.04, or 10%) was observed for case 7a to case 10a, but if the inherent behaviour of these cases is studied, no significant variation existed between the cases (0.59±0.02, or 3%). It was therefore concluded that the duration of the low power phase does not play a significant role in the power density damping stability of the PBMR design.

The average power-damping ratios for the second sensitivity study, which involved four load-follow transients that varied the power level of the final phase of a two-stage load-follow from 300 MW to 700 MW, varied from 0.54 (case 11) to 0.19 (case 14). This decrease confirmed the expected outcome of this sensitivity study, i.e. that an increase in the reactor power level would lead to a decrease in xenon-induced axial power density oscillation damping stability. This conclusion is in agreement with the findings of Section 5.3.

9.1.3 Chapter 7: Cases 15 to 24

In this section four important contributors to the PBMR axial xenon oscillation stability were investigated in more detail. It was quantitatively confirmed that the xenon-induced power oscillation damping stability *decreases* with:

- An increase in core size (cases 15 to 17).
- An increase in the total power levels (cases 18 to 21). These cases were also used to confirm that a decrease in the magnitude of the total temperature reactivity coefficient has a destabilising effect on xenon stability.
- An increase in the "flatness" of the thermal flux distribution (cases 22 to 24).

It was found in Section 7.2 that a significant decrease in damping stability occurred with an increase in the axial core height, and that a 40 m high core produced very unstable axial power oscillations. It was concluded that the current PBMR core design is sufficiently far removed from the xenon oscillation instability transition point regarding its axial core height, which could occur for a PBMR type core with an axial core height larger than 30 m operating at 1200 MW or higher.

In Section 7.3 four transient cases were defined. These cases consisted of repeating the basic case 1 control-rod insertion scenario at four fixed steady-state power levels: 200 MW, 400 MW, 600 MW and 800 MW. These transients used very high mass flow rates through the core to obtain reactor outlet temperatures (ROTs) of only 600°C,

to enable comparison of the effect of a variance in the magnitude of the total temperature reactivity coefficient on xenon stability. The quantitative power density damping ratio data for these four cases were summarised in Table 7-2, where the decrease in power damping stability with an increase in the power levels was clearly observed.

Table 7-3 showed that the damping ratio data itself differed significantly between the two transient sets, and that the lower ROT cases (cases 18 and case 19) exhibited weaker damped power oscillations compared to the 900°C ROT cases 1 and case 3. This confirmed the stabilising effect of a more negative temperature feedback coefficient at increased fuel and moderator temperatures. It was also noted that the increase in power and the simultaneous increase in the total temperature coefficient of reactivity work against each other in terms of xenon-damping stability (the former destabilising, the latter stabilising).

The conclusion from this section therefore was that from a xenon stability point of view the current PBMR design can be operated at total power levels up to 800 MW, since the increase in fuel and moderator temperatures would offset the destabilising xenon-damping effect of these increased power levels sufficiently to remain within the well-damped power oscillation regime.

The relatively peaked PBMR axial power profile was identified in Section 7.4 to be one of the main stabilising mechanisms in respect of xenon-induced power oscillations. The three transient cases included in this section all used an artificially "flattened" axial power profile, and it was shown that the power density oscillations for cases 22 to 24 are less damped than their respective nominal core counterparts. This decrease in stability for a 20 m high "flatter axial power profile" core was so severe that it represents the only transient in this study that actually produced un-damped axial power oscillations. It was therefore concluded in Chapter 8 that since the effect of flattening the axial power profile is so significant on xenon stability, careful consideration should be given to design decisions that could influence this factor.

9.2 RECOMMENDATIONS FOR FUTURE WORK

As indicated in Chapter 1, several assumptions and limitations limited the scope of this work. A more complete assessment of the full spatial xenon oscillation stability of the PBMR core design should include the following aspects:

- Several core states, and modes of operation within these states, need to be analysed to obtain the full picture of xenon stability under all possible operational conditions. These include detailed analysis on the start-up and run-in core phases, as well as low power operation (e.g. below 100 MW), where different values of the temperature feedback reactivity coefficients will occur. However, it is expected that the limiting (i.e. bounding) cases for axial xenon oscillations in the PBMR have been included in this study.

- An implicit assumption in the use of the current TINTE version for this study is that the two energy groups-approach is sufficient to quantify the xenon-induced power oscillation phenomena. A previous FZJ study [31] has investigated the energy group effects on xenon oscillations in HTR cores, and since a multi-group version of TINTE (MGT) will be available in 2008, it could be beneficial to confirm that the conclusions of this two-group study are still valid in the PBMR's case, for four or more energy groups.
- The two-group cross-section data in the current TINTE are reconstructed from pre-calculated polynomial representations of the cross sections dependencies. The validity of this cross-section representation method, with its neglect of the cross terms between the dependent variables, should be assessed when MGT becomes available. The MGT code is capable of performing dynamic in-line spectrum calculations that would form the reference solutions of the coupled neutronics and thermal hydraulic PBMR model.
- The azimuthal xenon oscillation stability of the PBMR core was not assessed in this study, due to the two-dimensional capabilities of TINTE. Studies are currently being performed at PBMR with the 3D version of the VSOP99 code [17] using the quasi-static approximation to assess this aspect of xenon stability, and independent verification of this work could also be performed by other codes (e.g. NEM-THERMIX [26]).

BIBLIOGRAPHY

[1] Stacey, W M (1970). Xenon-induced Spatial Power Oscillations. *Reactor Technology*, vol 13, No 3, pp. 252-279.

[2] Morales-Sandoval J, Hernandez-Solis A (2005). Global Physical and Numerical Stability of a Nuclear Reactor Core. *Annals of Nuclear Energy*, vol 32, pp. 1666-1678.

[3] Reitsma, F (2004). The Pebble Bed Modular Reactor Layout and Neutronics Design of the Equilibrium Cycle. (*In* PHYSOR 2004, Chicago, Illinois, April 25-29, 2004, on CD-ROM, American Nuclear Society, Lagrange Park, IL).

[4] Matzner, D (2004). PBMR Project status and the Way Ahead. (*In* HTR2004, Beijing, September 22-24, 2004, Paper A04).

[5] Scherer, W., Gerwin, H (1987). The TINTE Modular Code System for Computational Simulation of Transient Processes in the Primary Circuit of a Pebble-Bed High-Temperature Gas-Cooled Reactor. *Nuclear Science and Engineering*, vol 103, pp. 302-312.

[6] Mogale, N W (2007). PBMR Safety Analysis Report, SAR Revision 2, Chapter 4, 001929, Revision 2A, p.8.

[7] Lauer, A. (2000). Analysis of Power Density Fluctuations in the PBMR Due to Xenon Dynamics and Control Rod Movement during Load-Follow Transients. FZJ-ISR-RC-5020-2000 (PBMR472 e-iv).

[8] Ikeda H, Ama T, Hashimoto K., Takeda T (2001). Nonlinear Behaviour under Regional Neutron Flux Oscillations in BWR Cores. *Journal of Nuclear Science and Technology*, vol. 38, No. 5, pp. 312-323.

[9] Na M G, Upadhyaya B R, Choi J I (1998). Adaptive Control for Axial Power Distribution in Nuclear Reactors. *Nuclear Science and Engineering*, vol 129, pp. 283-293.

[10] Duderstadt J J, Hamilton L J (1976). Nuclear Reactor Analysis. John Wiley & Sons, pp. 569-570.

[11] Duderstadt J J, Hamilton L J (1976). Nuclear Reactor Analysis. John Wiley & Sons, p. 25.

[12] Duderstadt J J, Hamilton L J (1976). Nuclear Reactor Analysis. John Wiley & Sons, p. 161.

[13] Duderstadt J J, Hamilton L J (1976). Nuclear Reactor Analysis. John Wiley & Sons, p. 579.

[14] Froehling W, Lauer A, Schwiegk H J (1976). Annals of Nuclear Energy, vol 3, pp. 215-220.

[15] Sen, S. (2007). Xenon Induced Oscillations in the Azimuthal Direction. PBMR Internal Publication T000914.

[16] Lauer, A. (1972). Räumliche Xenon-Schwingungen in Hochtemperaturreaktoren. (Spatial Xenon Variations in High Temperature reactors). FZJ Study Jul -850-RG, PBMR Study PBMR/7814.

[17] Stacey, W M (2001). Nuclear Reactor Physics. Wiley-Interscience; p. 649.

[18] Levenberg, K A (1944). Method for the Solution of Certain Problems in Least Squares. *Quarterly Applied Mathematics*, No 2, pp. 164-168.

[19] Marquardt, D (1963). An Algorithm for Least-Squares Estimation of Nonlinear Parameters. *SIAM Journal of Applied Mathematics*, No 11, pp. 431-441.

[20] Gill P R; Murray W and Wright M H (1981). The Levenberg-Marquardt Method: Practical Optimization. London Academic Press, pp. 136-137.

[21] Lourakis M, Levmar v2.1.2. Institute of Computer Science, Foundation for Research and Technology – Hellas, Heraklion, Crete, Greece. http://www.ics.forth.gr/ ~ lourakis/levmar/.

[22] Chopra, A K (1995). Dynamics of Structures: Theory and Applications to Earthquake Engineering. Prentice Hall, pp. 44-48.

[23] Gerwin, H (1989). Das Zweidimensionale Reaktordynamikprogramm TINTE. Teil 2: Anwendungsbeispiele. (The Two-dimensional Reactor Dynamics Code TINTE. Part 2: Sample Cases).). FZJ Report Jül-2266.

[24] Cifford, I (2007). TINTE Nuclear Calculation Theory Description Study. PBMR document 052322, Revision B.

[25] Strydom, G (2007). TINTE Xenon Stability of the PBMR 400 MW Design. PBMR report T000110, Revision C.

[26] Bandini, B A (1990). Three-dimensional Transient Neutronics Routine for the TRAC-PF1 Reactor Thermal Hydraulics Reactor Code. PhD Dissertation, Pennsylvania State University.

[27] Jeong C; Choi H (1999). Instability Analysis on Xenon Spatial Oscillations in a CANDU-6 reactor with DUPIC Fuel. *Annals of Nuclear Energy*, Vol 27, Issue 10, pp. 887-899.

[28] The Westinghouse BEACON ™ PWR On-line Monitoring, Surveillance and Predictive Software. http://www.westinghousenuclear.com/Products_&_Services/docs/flysheets/NF-FE-0008.pdf

[29] Wang Y, LI F, Luo Z, Han S (2003). On-line Monitoring the In-core Power Distribution by Using Ex-core Ion-chambers. *Nuclear Engineering and Design* 225, pp. 315-326.

[30] Li F, Luo Z, Hu Y (1997). Harmonics Synthesis Method for Core Flux Distribution Reconstruction. *Progress in Nuclear Energy*, Vol. 31, No. 4, pp. 369-372.

[31] Erven U, Lauer A. (1977). Vergleich Verschiedener Energiediskretisierungs-modelle bei der Digitalen Berechnung Radialer und Azimutaler Xenon-transienten am Beispiel von HTR-Cores. (Comparison of Various Energy Discretisation Models for the Calculation of Radial and Azimuthal Xenon Transients in HTR cores). FZJ report Jül-1387.

[32] Knob, PJ (1982). Entwicklung Eines Dreidimensionalen Rechenprogramms zur Entfaltung von Leistungsverteilungen Mittels Seitenreflektorinstrumentierung sowie Bestimmung der Leistungsfähigkeit und Grenzen dieses Verfahrens. (Development of a Three-dimensional Computer Code for the Construction Of Power Distributions by Means of Side Reflector Instrumentation and Determination of the Limitations of this Method). FZJ Report Jül-1793.

[33] Knob PJ, Lauer A, Neef RD (1980). Numerische Untersuchungen zur Detektion von Flußstörungen im Hochtemperaturreaktor mit einer Ausseninstrumentierung. (Numerical Investigations for the Detection of Flux Disturbances in High-Temperature Reactors Using Out-of-core Instrumentation). *Atomenergie Kerntechnik*, vol. 35. pp. 259-263.

[34] Koch, R (1978). Modelluntersuchungen zum Problem der Detektion von Flußirregularitäten (Xe-Schwingungen) in großen Reactoren. (Model Investigations on the Problem of the Detection of Flux-Instabilities (Xenon Oscillations) in Large Reactors). FZJ Report Jül-1488.

[35] DUDERSTADT, J. J., HAMILTON, L. J. 1976. Nuclear reactor analysis. John Wiley & Sons, p. 563.

APPENDIX A: TINTE 100%-40%-100% Load-Follow Dynamic Control Rod Worth

The data presented in this Appendix deviate slightly from the focus of determining the xenon-induced oscillation stability of the 400 MW PBMR design, and as such do not fit in the main body of this work. It is however of sufficient importance to include as part of the overall xenon-related work, since the mitigation of the effects shown here might feed back into the PBMR operational procedures.

A detailed version of Figure 5-1 in Section 5.1 (which presented the control rod and xenon behaviour vs. time for a 100%-40%-100% load-follow) is shown here as Figure A-1, where it can be seen that the control rods reach their fully withdrawn position (0 cm) at t = 3.8 h, i.e. 2.4 h before the maximum xenon peak occurs. A "poisoned-out" period of almost 4 h exists for case 5 (100%-40%-100% load-follow), where no active reactivity increasing control of the reactor is possible. This has some practical implications, in the sense that no reactor operator would be allowed to operate the core with its control rods completely withdrawn, since some operational control rod worth margin is required by the nuclear regulator. The current TINTE dynamic control rod worth therefore does not meet the 100%-40%-100% load-follow design requirements for the PBMR core.

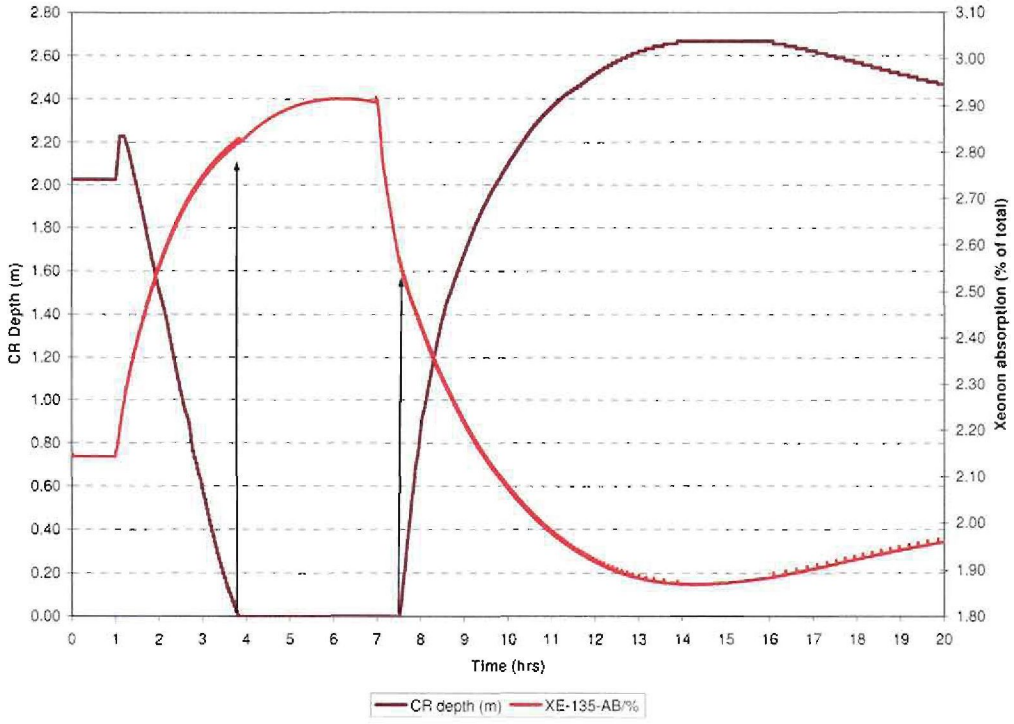

Figure A-1: Case 5 (100%-40%-100% load-follow) detail of core-averaged xenon absorption and control rod locations vs. time

The second point of interest is that the control rods need to be inserted to 267 cm to counteract the decay of xenon at t = 14 h. This location is 65 cm deeper than the nominal control rod location at 202 cm. Note also the small spike in the control rod location curve at t = 1 h, where the control rods were inserted by 20 cm to facilitate the drop in power from 400 MW to 160 MW.

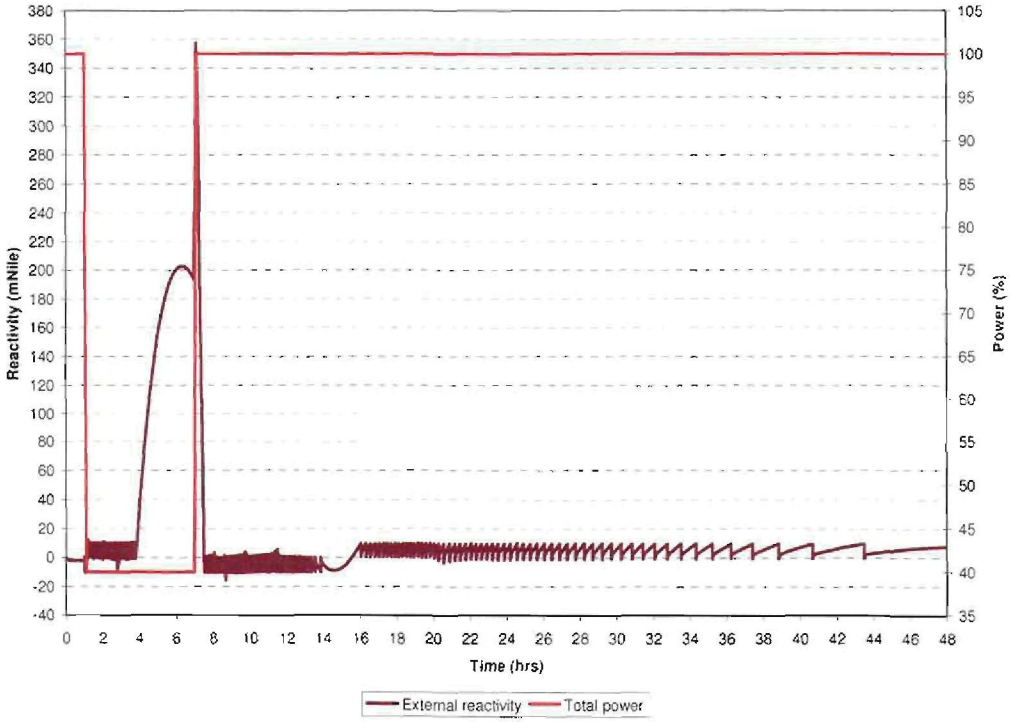

Figure A-2: Case 5 (100%-40%-100% load-follow) total power and external reactivity vs. time

Figure A-2 shows the total reactor power and the external reactivity needed to keep the reactor critical for case 5, in addition to the movement of the control rods already shown in Figure A-1. The plot is noteworthy for three reasons:

1. The control rod auto-controller controls the reactivity bandwidth at ± 10 mNile, i.e. whenever k-eff is greater than 1.0001, or smaller than 0.9999, the control rod is moved at 1cm/s in the correct direction to return k-eff to 1.0000. This behaviour can be seen in Figure A-2 as a series of sharp-edged oscillations, within a 20 mNile reactivity band.
2. Since the control rod worth is not adequate for the 100%-40%-100% load-follow in the present design, and to enable TINTE to continue the transient, the control rod auto-controller is paused as soon as the control rods reach their fully withdrawn location. An indication is then given of the amount of reactivity that would be needed to return the core to a critical situation. (The calculation can still continue, since TINTE is instructed to keep a re-normalised k-eff = 1.0000, and the residual reactivity needed to obtain k-eff = 1.0000 is shown as the field "external reactivity").

The external reactivity field shows that 202 mNile (or 0.2%) positive reactivity needs to be added to keep k-eff = 1.000 at the time when the xenon peak occurs. Therefore, according to the current TINTE results, the control rods need to be worth at least 202 mNile more than their current dynamic value to overcome the xenon build-up. At t = 0 h, the control rod inserted at 202 cm has a static worth of approximately ~ 1300 mNile, or 1.30%, when they are fully withdrawn. (A side note on control rod worth: the static worth, as indicated above, and the dynamic worth as calculated during a transient with changing fuel and moderator temperatures, cannot simply be added together).

3. In addition to the ability to overcome the xenon build-up during this load-follow, the PBMR design is also required to be able to start ramping back to higher power levels at any time during the 40% power phase. At t = 7 h a sharp peak of 354 mNile in the external reactivity field indicates that even more positive reactivity needs to be available than just the reactivity to overcome the xenon peak absorption levels. This is caused by the increase in fuel temperature, and the resultant total temperature feedback effect on reactivity. The higher fuel temperatures therefore cause a decrease in the total core reactivity, which needs to be counteracted by withdrawing the control rods.

The total dynamic control rod worth requirement therefore needs to take into account two factors: it must be able to overcome the xenon maximum absorption levels for any 100%-40%-100% event, and it must be able to accommodate ramp-up to higher power levels at any stage during these types of load-follows. TINTE analysis of case 5 seems to suggest that the control rod system needs at least ~ 200-400 mNile more dynamic worth than it currently has. This confirms observations made in previous studies performed by FZJ on the PBMR design [7].

Further investigations are needed to translate this requirement into a steady-state control rod worth, since VSOP99 supplies TINTE with the spatial isotopic and burn-up data, as well as the equivalent boron concentrations in the control rod region, which effectively determines the control rod worth in TINTE. However, it should be kept in mind that the TINTE dynamic control rod worth is a function of the spatial treatment of the rods, since static control rod (e.g. S-curves) and 3D VSOP analysis will more than likely give different control-rod worth results. Another contributing factor that could be investigated when a multi-group version of TINTE becomes available, is the current two energy group-approach followed in TINTE, in contrast to the 4-group structure of VSOP99.

Even if the current two-group TINTE model suggests that the dynamic control rod worth is not adequate for the 100%-40%-100% xenon override, it must be noted that several operational mitigation strategies can be considered. Four examples have been investigated as part of this study:

1. Figure A-3 presents a variation on case 5 where the 40% phase has only been specified for one hour. The control rods are withdrawn up to 1 meter inserted, which proves that a fast change to 40% power is possible, but for periods shorter than ~ 2 h.

2. Another interesting possibility is shown in Figure A-4, where the 100%-40%-100% pattern has been repeated for 3 cycles in 24 h. Due to the increase in xenon burn-out caused by the repeated ramps to full power, the build-up of xenon in the subsequent 40% phases are less, so that a fast 40% load-follow actually becomes possible after the first drop in power. This transient shows the importance of the power history on the xenon levels in the core: if the first reduced power level can be reached (possibly 60%, as is shown in the next point), the subsequent 40% phases become possible.

3. Instead of going straight for the 40% power phase, an intermediate achievable lower power phase can be used to increase the xenon burn-out. This is due to the period spent at higher (than 40%) power, where the higher thermal flux levels lower the total xenon build-up. Figure A-5 indicates that a 40% power phase can be achieved (with the control rods at ~ 20 cm), if it is preceded by a 60% power phase. Note however that the control rods still need to be fully withdrawn when the 100% phase is reached, so there must also be operational limitations on the low-to-high power transitions.

4. If the power reduction rate is decreased, the higher thermal flux levels over a longer period lead to increased xenon burn-out, which lowers the total xenon build-up. This is shown in Figure A-6, where the drop in power to 40% has been performed over 4 h, i.e. at 1 MW per minute. This "slow" load-follow also causes the rods to fully withdraw, but the control rod "dead-time" at 0 cm is now only 55 minutes, compared to almost 4 h in the case of a 6 minute power reduction rate.

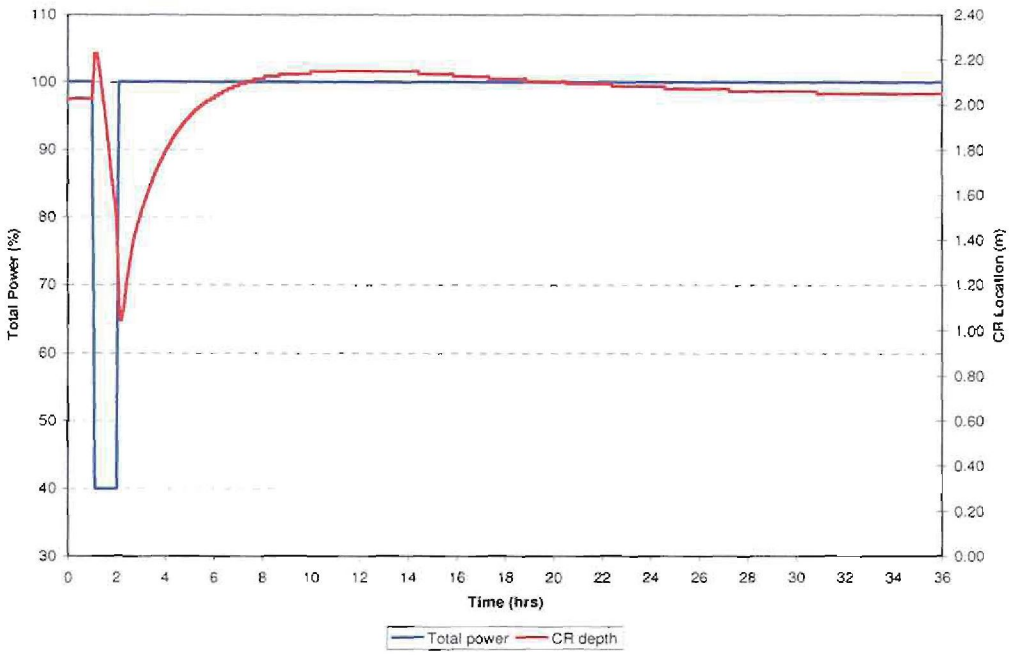

Figure A-3: Total power and control rod depth vs. time – 100%-40%-100%, with 40% power phase for 1 hour

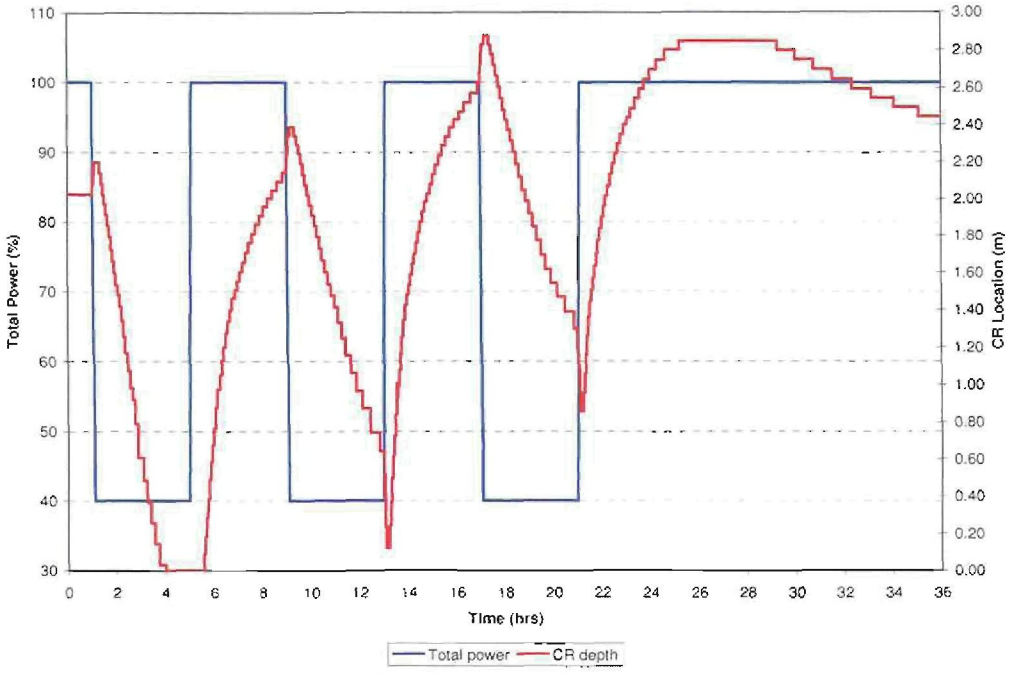

Figure A-4: Total power and control rod depth vs. time – repeated 100%-40%-100% cycle

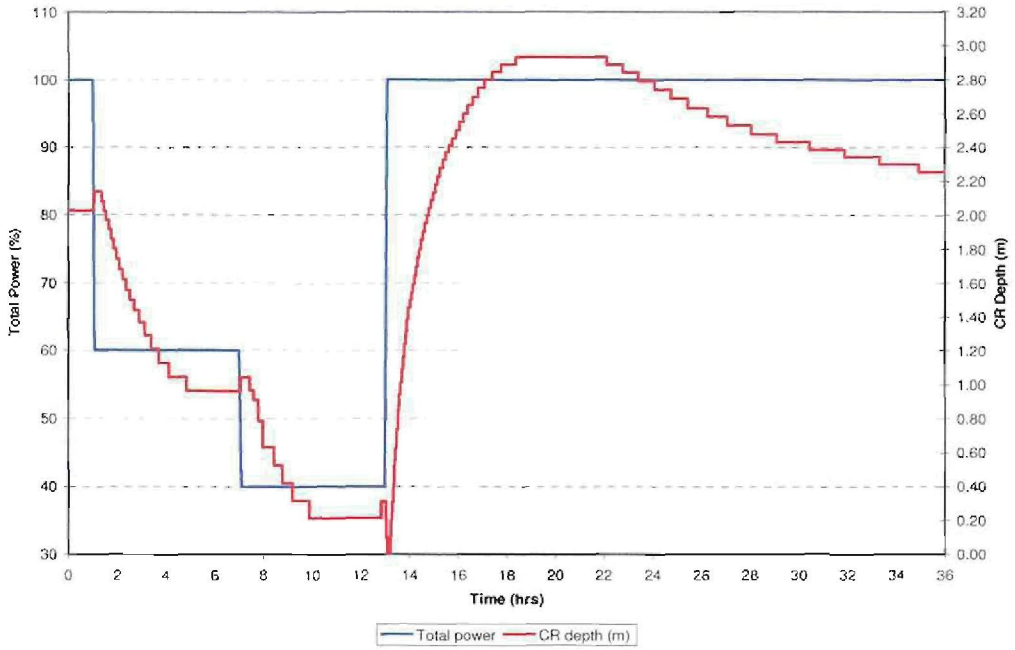

Figure A-5: Total power and control rod depth vs. time – 100%-60%-40%-100% load-follow

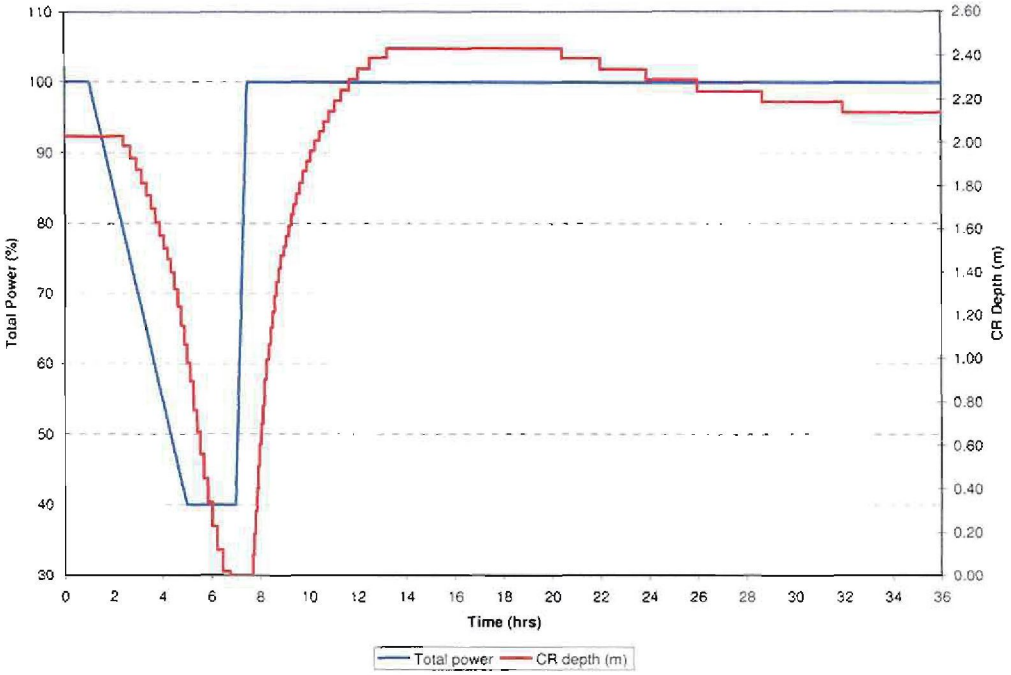

Figure A-6: Total power and control rod depth vs time – 100%-40%-100% load-follow with reduced power reduction rate